Sundstrand Aviation - Denver
Denver, Colorado
CDRD 64-7033

Final Report

# Effect of Back Pressure
# on Re-Entry Turbine Performance

Prepared Under Navy, Office of Naval Research
Contract Nonr-2292(00)

13 March 1964

Prepared by

Robert G. Adams, Manager Turbomachinery Group
James E. Mullaney, Project Engineer

# TABLE OF CONTENTS

# TABLE OF CONTENTS (Cont'd)

# 1.0    OBJECT OF PROGRAM

The intent as stated in Reference 1 was to investigate experimentally the influence of back pressure (Reynolds Number effect) on the stage performance and overall performance of a two-stage re-entry type turbine, to analyze and correlate these data, where possible, with existing theories and to attempt a loss analysis which will separate the viscous losses from the non-viscous losses. For these tests, existing turbine hardware was to be used with only minor changes. The investigations were intended to be of exploratory nature registering the gross effects and main trends of the back pressure influence at supersonic as well as sonic approach velocities to the rotor.

## 2.0 CONCLUSIONS OF PROGRAM

Valid data have been obtained on the influence of the Reynolds number on a supersonic impulse turbine operated at a pressure ratio of 17 to 1 and a design specific speed of about 38. The expected Reynolds Number influence is observed namely a decreasing efficiency with decreasing Reynolds numbers in the medium Reynolds number regime. These data are in fair agreement with pre-calculated data reported in Reference 13 with the exception of the low Reynolds number regime where a somewhat larger Reynolds number effect has been calculated than actually observed during these tests, Figure 39.

The two turbine designs tested at transonic rotor approach velocitie show a considerably smaller Reynolds number influence than precalculated and a considerably smaller efficiency level than conventionally expected. Detailed measurements and analysis were performed on these designs. These revealed that the first design experienced large wake losses between nozzle and rotor and that the second transonic design was operating at extremely high degrees of reaction in the optimum efficiency regime due to rotor choking effects. These effects are described in detail in section 6.2.1.1. This caused an excessive angle of attack at the rotor, i.e., hig incidence losses due to the selection of a symmetrical (impulse type) rotor blade design. Thus the efficiencies and Reynolds Number influence shown in Figures 17, 19 and 40 must be considered typical for the particular geometr tested but are not necessarily typical for the efficiency values obtainable with a more favorable rotor and stator geometry.

The detailed analysis of the flow phenomena of the transonic rotor designs indicated that the rotor choking effects and the associated high degree of reaction are typical for impulse turbines designed for a pressure ratio of 5 to 1 and that the design of efficient impulse turbines for this pressure ratio is one of the more difficult aerodynamic design problems, since by using conventional cascade geometries even a small boundary layer build up in the rotor tends to force a comparatively high degree of reaction in order to satisfy the continuity relation through rotor and stator. Hence for these designs it is essential that either a diverging rotor channel be used in order to enable impulse operation or that a blunt rotor leading edge be provided, in order to minimize the incidence effects occurring in cases where a constant area rotor channel is used.

The test data obtained on the two stage reentry design show the expected trends, namely a comparatively mild Reynolds number influence since only the last stage (which contributes only 20 to 30% of the energy at maximum efficiency operation) is effected by the low back pressure. The pertinent data are presented in Figures 28 and 44. Only insignificant Reynolds number effects on interstage leakage were observed.

## 3.0    RECOMMENDATIONS

Since the test data regarding the back pressure effect on turbines designed for a transonic rotor approach velocity are inconclusive due to rotor choking effects it is recommended that these tests be repeated with a modified rotor design. This will necessitate the fabrication of a new turbine rotor which has either a diverging channel geometry or a blunt leading edge.

Only the "medium" Reynolds number regime has been explored experimentally, due to the limited power range of the dynamometer. Extension of the experimental investigations into the higher Reynolds number regime will be essential for a better understanding of the flow phenomena and back pressure effects in this operating regime.

Additional theoretical and experimental investigations are required in order to extrapolate the data to different geometries and obtain knowledge on the optimum geometry for turbines operating at low back pressures.

# 4.0 DESCRIPTION OF PROGRAM

Three different nozzle configurations were investigated with an impulse type rotor at varying back pressures but at constant overall pressure ratio in the form of 75 percent admission turbines. The same rotor was tested again in a two-stage reentry design at varying back pressures and at constant overall pressure ratio. The nozzle configurations for the single stage investigations were (a) supersonic nozzles designed for a pressure ratio of about 17 to 1 yielding a nominal rotor approach Mach number at design point of about 1 8, (b) supersonic nozzles designed for a pressure ratio of about 5 to 1 yielding a nominal transonic approach velocity to the rotor (c) supersonic nozzles designed for a pressure ratio of about 5 to 1 with a reduced trailing edge thickness providing again a nominal transonic rotor approach velocity. The two-stage reentry turbine had a nozzle configuration where each stage was designed for a pressure ratio of about 17 to 1 with supersonic converging diverging nozzles providing a nominal rotor approach Mach number of 1.8 for each stage.

The overall test procedure followed was to test each turbine configuration at its design pressure ratio at various back pressures, and to run the turbine at various back pressures at speeds ranging from zero to approximately 10 percent over the maximum efficiency speed.

The single stage turbine having a relative rotor approach Mach number of 1.8 and the two-stage re-entry turbine were run according to the test plans given in the following tables:

### Single Stage Turbine, Relative Mach Number = 1.8

Turbine Pressure Ratio = 17

| Turbine Exit Pressure psia | | | Speed rpm | | | |
|---|---|---|---|---|---|---|
| .05** | 0 | 10,000 | 20,000 | 30,000 | 40,000 | |
| .07 | 0 | 10,000 | 20,000 | 30,000 | 40,000 | |
| .09 | 0 | 10,000 | 20,000 | 25,000 | 30,000 | 35,000 |
| .17** | 0 | 10,000 | 20,000 | 30,000 | 40,000 | |
| .25 | 0 | 10,000 | 20,000 | 25,000 | 30,000 | 35,000 |
| .30 | 0 | 10,000 | 20,000 | 30,000 | 40,000 | |
| .70 | 0 | | 25,000 | 30,000 | 35,000 | |

** These tests were repeated.

## Two-Stage Re-Entry Turbine

### Turbine Pressure Ratio - 300

| Back Pressure psia | | | | Speeds rpm | | | |
|---|---|---|---|---|---|---|---|
| .05 | 0 | 10,000 | 20,000 | 25,000 | 30,000 | 35,000 | 40,000 |
| .10 | 0 | 10,000 | 20,000 | 25,000 | 30,000 | 35,000 | 40,000 |
| .15 | 0 | 10,000 | 20,000 | 25,000 | 30,000 | 35,000 | 40,000 |
| .30 | 0 | 10,000 | 20,000 | 25,000 | 30,000 | 35,000 | 40,000 |
| 150 | 0 | 10,000 | 20,000 | 25,000 | 30,000 | 35,000 | 40,000 |

The nominal pressure ratio, exhaust pressures and speeds for the tests of the transonic turbine configurations are given in the following table. It should be noted that these are the conditions that were stipulated in the test instructions. The conditions actually obtained differ slightly from these values.

## Single Stage Turbine, Transonic Rotor Approach Velocity

(Both nozzle designs)

### Turbine Pressure Ratio 4.9

| Turbine Exit Pressure psia | | | Speed rpm | | |
|---|---|---|---|---|---|
| .10 | 10,000 | * | | | |
| .25 | 10,000 | 15,000 | 20,000 | 25,000 | 30,000 |
| .50 | 10,000 | 15,000 | 20,000 | 25,000 | 30,000 |
| 1.0 | 10,000 | 15,000 | 20,000 | 25,000 | 25,000 |
| 1.7 | 10,000 | 15,000 | 20,000 | 25,000 | 25,000 |

These tests were repeated several times for both nozzles.

* Higher speeds were not possible because the turbine output at these low pressures is less than the losses in the dynamometer.

In most of these tests, the successive runs were made at increasing values of speed. In testing the second transonic turbine design, however, speed was increased stepwise from 8000 rpm to 31,000 rpm, then decreased stepwise to 8500 rpm in an effort to determine whether any flow instability, observed by other experimenters, was present.

The temperature of the gas (dry nitrogen) at turbine inlet was maintained at 300°F as nearly as possible during these tests. The efficiencies of the transonic turbine, described in Section 6. 1. 3 were much lower than expected. Many repetitions were made in testing the second transonic design in an effort to determine the cause of these low efficiencies. An explanation was obtained from the analysis described in Section 6. 2. 1. 1.

The test operation of the single stage turbine with a relative Mach number 1. 8 and of the two-stage turbine proceeded without special problems and valid results were obtained with few repeated tests. The turbine dynamometer described in Section 5. 0 operated in a very satisfactory manner. Consistent test results were obtained during most of the test program.

## 5.0　DESCRIPTION OF TEST APPARATUS

## 5.1　TURBINE DESIGNS

### 5.1.1　Turbine Wheel Design

The turbine arrangements were obtained by assembling various nozzle arrangements with the turbine wheel described in Reference 2. This wheel (see Figure 1) was originally designed for use with a two-stage re-entry turbine and may be described as follows:

| | |
|---|---|
| Rotor tip diameter: | 6.3" |
| Rotor mean diameter: | 5 95" |
| Rotor hub diameter: | 5.6" |
| Number of blades: | 120 |
| Blade heights. | .35" |
| Blade chord: | .3" |
| Blade type: | Symmetrical impulse |
| Inlet and exit angle: | 30$^c$ |
| Leading and trailing edge thickness: | .015" |
| Tip clearance: | .007" |
| Side clearance: | .008" |
| Ratio of tip clearance to blade heights: | .02 |
| Trailing edge blockage: | .239 |

The blade form is presented in Figure 2.

| | |
|---|---|
| Ratio of blade heights to rotor diameter | .0555 |

### 5.1.2　Nozzle Design

#### 5.1.2.1　Supersonic Nozzle (Single Stage)

The main design parameters of the nozzles in this configuration are summarized in the following table:

| | |
|---|---|
| Nozzle Type: | Converging-diverging circular cross-section |
| Number of Nozzles: | 16 |
| Nozzle Throat Diameter: | 0. 157" |
| Nozzle Diameter at Nominal Exit: | .331" |
| Nozzle Angle: | 20° |
| Area Ratio: | 4. 414 |
| Arc of Admission: | 75% |

A sectional view of a typical nozzle is shown in **Figure 3.** The trailing edge thickness at the mean radius was almost non-existent since the nozzle exit areas were overlapping.

5 1.2.2 First Transonic Design

A cross-section of a typical nozzle is shown in **Figure 4** and a photograph in **Figure 5.** The main design features may be described as follows:

| | |
|---|---|
| Type: | Converging-divergent circular cross-section |
| Throat Diameter: | .228 in. |
| Exit Diameter: | .262 in. |
| Nozzle Angle: | 21 degrees |
| Divergence Angle: | 4 degrees 15 minutes |

The design of this nozzle was such that the exit diameter quoted above was only attained at the point at which the nozzle centerline crossed the exit plane. That is, the nozzle walls did not give guidance to the gas over the full area ratio. In addition, the spacing and size of the nozzle was such that a flat area with a minimum width of 0. 15 inches existed between the nozzle exits. It was thought that these would give rise to thick wakes at the nozzle exit, and obscure the Reynolds number effect. A new nozzle was therefore designed.

5. 1. 2. 3        Second Transonic Design

The main design parameters of this nozzle are (Figure 6 and 7)

| | |
|---|---|
| Nozzle Type: | Convergent-divergent circular cross-section |
| Throat Diameter: | . 298 inch |
| Exit Diameter: | . 340 inch |
| Nozzle Angle: | 21 degrees |
| Divergence Angle: | 8 degrees |
| Number of Nozzles: | 14 |

These nozzles had expansion to the full design exit area within the nozzle and a minimum length parallel section leading to the exit plane.

5. 1. 2. 4        Re-Entry Axial Turbine

The second stage nozzle was the same as described in Section 5. 1. 2. 1.  For the two-stage tests the nozzle collector duct was provided with a side port for receiving the flow discharged from the first stage.  This arrangement is shown in Figure 8 and is similar to the re-entry turbine design described in Reference 2.  The nozzle of the first stage had the following data:

| | |
|---|---|
| Nozzle Type: | Convergent-divergent circular cross-section |
| Number of Nozzles: | 1 |
| Nozzle Throat Diameter: | . 167" |
| Nozzle Diameter at Nominal Exit: | . 343" |
| Area Ratio: | 4. 21 |
| Nozzle Angle: | 20° 50' |
| Arc of Admission: | 5. 45% |

A cross-section of this nozzle is shown in Figure 9.

## 5.2 DYNAMOMETER

### 5.2.1 General Description

The dynamometer used for measuring the output of the turbine was designed and built by Sundstrand specifically for this program and replaces the dynamometer described in Reference 3. It consists of a specially designed homopolar alternator with a ball bearing supported rotor, the entire machine being supported on nitrogen lubricated hydrostatic gas bearings. The torque produced by the turbine is measured by a pneumo-mechanical balance system which is described in detail in Section 5.2.7. The turbine wheel is mounted directly on the end of the dynamometer shaft as shown in Figures 10 and 11.

### 5.2.2 Rotor Design

The rotor is typical of the homopolar alternator, with four protruding pole pieces arranged in diametrically opposed pairs, one pair at each end of the rotor. The axes of the pairs are oriented at 90° to each other. The pole pieces are built up of laminations, arranged in planes normal to the axis of the rotor, assembled into dovetail slots in the solid forged rotor and held in place by welding beads along the axial edges of the slots. The rotor is supported in the frame of the dynamometer by special close tolerance, high-speed, angular contact ball bearings. The turbine-end or inner-end bearing, is located axially in the frame by retaining rings and has a tight fit in the frame. The outer end bearing has a close sliding fit inside the frame and is spring loaded against the rotor, and thus against the other bearing, by a coil spring that acts on the outer race. The design preload force is 30 pounds.

### 5.2.3 Stator and Frame Design

The stator of the dynamometer is built of two stacks of laminations with space between them for the field coils. The stator is wound as a three-phase machine with a design frequency of 2000 cps at 60,000 rpm. The field coil is wound in a plane normal to the axis of the rotor and is housed in a rectangular-section annular channel formed in the outer frame of the machine.

The frame of the dynamometer consists of a cylindrical shell and two thick end plates. The cylindrical shell is made of two sections bolted together in the plane of the field coil recess. Cooling fins are machined around the exterior of the outer shell sections and the end plates have integrally machined hubs, which form trunnion journals. The entire frame was designed for extreme stability of alignment, together with good conduction of heat from the stator stacks.

### 5.2.4 Support Structure

The dynamometer is supported on gas bearings installed in two massive end brackets fabricated from one-inch thick plate. The bracket at the turbine end is made of low carbon steel plate and is welded on to the base plate, which is also one-inch thick plate. The base plate and turbine end bracket assembly is stiffened by the addition of 1/2-inch thick gusset plates. The nozzle ring assembly of the turbine is bolted directly to the support bracket and is aligned with the axis of the dynamometer by a pilot machined on the face of the bracket. The outer end bracket is fabricated of one-inch thick aluminum alloy plate and is bolted directly to the machine base plate. Shims are provided for the alignment of the trunnion bores located in the end brackets. Passages for the gas supply to the trunnion bearings are drilled through the support brackets.

### 5.2.5 Trunnion Bearings

The trunnion bearings are hydrostatic gas-supported journal and thrust bearings. A combined journal and thrust bearing is provided in the turbine end bracket by shrinking a hardened steel ring into the bracket, of sufficient radial depth to provide a thrust face on each side of the ring. Gas passages are formed in the ring and communicate between a deep groove in the outer diameter and the side faces and inner surface. The groove and holes together therefore act as a distributing manifold, carrying gas from the passages drilled in the end bracket to the thrust and journal faces of the bearing ring. One thrust face of the turbine-end trunnion is formed by a shoulder on the end plate; the other by a removable thrust ring retained by a spring clip. The thrust shoulder and ring on the dynamometer frame boss, assemble on either side of the bearing ring in the support bracket. These, together with the close-tolerance-machined outer diameter of the boss, form the combined thrust and journal trunnion bearing. The journal trunnion bearing at the outer end of the dynamometer is a plain bearing formed between a hardened insert in the outer end bracket and the outer diameter of the boss on the outer dynamometer end plate. Gas is distributed from a single supply passage in the end support bracket through a groove machined in the outer diameter of the bearing insert and small-diameter radial holes from the groove to the inner surface of the insert.

### 5.2.6 Dynamometer Loading System

The electrical output of the dynamometer is absorbed by an air-cooled load bank. The resistance of the load bank can be varied in steps and this provides the coarse load control of the dynamometer. Fine control of the dynamometer power absorption is obtained by variation of the field current.

## 5.2.7  Torque Reading System

The principle of operation of the torque measuring system is that the torque, produced by the turbine, and absorbed by the alternator, is transmitted to the dynamometer support system through a loading arm made of 3/4-inch diameter steel rod. The steel rod is screwed radially into the alternator outer casing at one end and is supported at the other end by a piston working in a vertical cylinder, mounted on an extension of the base plate. The downward force exerted by the loading arm on the piston is opposed by gas under pressure in the cylinder and the pressure of the gas is adjusted until the loading arm is exactly horizontal. The position of the loading arm is detected by an electrical-induction type of proximity gage, mounted on the opposite side of the dynamometer to the loading cylinder. This proximity gage senses the position of a probe mounted on the end of a second rod, similar to the loading arm, which is screwed into the dynamometer diametrically opposite to the loading arm. When the proximity gage indicator shows that the torque loading arm is in the required position, the pressure in the cylinder can be read on a manometer connected to the cylinder. The dynamometer has three manometers containing respectively; Merriam No. 1 oil, Merriam No. 3 oil, and mercury. The manometers are connected in parallel to a load cylinder with selector valves to isolate the inactive manometer. Thus a wide range of torque measurements may be made with the greatest possible accuracy. The readings of these manometers may be calibrated against the torque produced by known weights applied to the load arm. These weights are permanently suspended on a wire from the load arm. They are applied or removed by lowering or raising a scale pan suspended on a wire that  ises through a gland in the wall of the altitude chamber. This arrang  ..ent was made so that the torque reading system could be calibrated when exposed to the 100,000 foot simulated altitude, the normal operating environment of the turbine-dynamometer assembly. For further accuracy, the piston is centered in the cylinder by a separate gas supply fed through the cylinder walls forming a sliding gas bearing around the piston.

## 5.2.8  Turbine Back Pressure Control and Dynamometer Cooling

These two functions are integrated into the turbine exhaust system since turbine exhaust gas is at low temperature and can be used to cool the dynamometer. The Sundstrand altitude simulation system cannot maintain a given pressure with sufficient accurac, at simulated altitudes other than the maximum possible altitude. It is therefore necessary to immerse the turbine-dynamometer assembly in an altitude chamber connected to the altitude simulation system and vary the back pressure on the turbine by means of a valve in the exhaust ducting. This valve consists of a cone which has the same diameter as the exhaust duct and slides axially inside

the duct. Two exit ports are provided in the sides of the duct and axial motion of the cone alternatively partly covers or uncovers these ports. The cone is moved axially in the duct by an electrically driven linear actuator, which is remotely controlled from the test cell control panel. The position of the actuator is indicated on the control panel by a potentiometer-voltmeter combination.

Gas leaving the ports in the exhaust duct walls is carried back through two rectangular ducts to either side of the dynamometer alternator. The ends of the ducts deflect this exhaust gas against the sides of the alternator so that it flows over the cooling fins and regulates the alternator temperature. Adjustable doors in the sides of the ducts bypass a controllable amount of gas from the dynamometer if the cooling should become excessive with full turbine flow.

## 5.3    TURBINE INSTRUMENTATION

### 5.3.1  Gas Pressures

In the re-entry turbine test program, pressures were measured by means of static taps located in the inlet duct, at the first stage nozzle exit, at four points in the interstage duct (see Figure 8), at the exit of one of the second stage nozzles, and at four points in the exhaust duct (see Figure 13).

In the single stage supersonic and the first transonic turbine tests, the pressure taps in the inlet duct (the interstage duct of the two-stage machine) and the exhaust duct were the same as those in the two-stage machine. The static taps in the original nozzle ring were located on the inner and outer side of the exit from the ninth nozzle, approximately .05 inches, measured axially, from the exit plane.

More static taps were installed in the nozzles in the single stage second transonic turbine tests. At each end of the nozzle arc, a static tap was made in the outer side of the nozzle, opposite the centerline, approximately .05 inch from the exit plane. In the eighth nozzle, a tap was made at the end of the diverging portion of the nozzle; in the ninth nozzle a tap was made at the throat of the nozzle; and in the tenth nozzle two taps were made .050 inches from the exit plane offset to either side of the nozzle. (See Figure 6).

All the static taps were connected through the test cell piping system to manometers. The manometers used either Merriam No. 1 oil, Merriam No. 3 oil, or mercury, according to the pressure range being measured. All manometers connected to static pressure taps in the turbine flow channels used altitude chamber pressure as a reference during start-up of the turbine test rig, but switched to an accurately measured vacuum reference for the test runs.

## 5.3.2  Gas Temperatures

All gas temperatures in the turbine were measured by means of copper constantan thermocouples connected to a cold-junction-compensated multiple print-out recording indicator.  One thermocouple was located in the inlet duct, three more were equally spaced in the interstage duct, and four equally spaced around the large-diameter exhaust duct in a plane approximately 6 inches downstream from the exit plane of the turbine.

## 5.3.3  Gas Mass Flow Rate

The mass flow rate of the working fluid was calculated according to perfect gas isentropic flow theory, for flow through a choked nozzle, using the measured inlet total pressure and temperature, and the area of the first nozzle with an area coefficient of .98.

## 6.0    RESULTS AND DISCUSSION

## 6.1    TEST RESULTS

### 6.1.1   Accuracy of Results

In reviewing the complete set of data collected for the various turbine configurations tested, all factors which enter into the turbine efficiency determination were given a final check.   The primary factors are:

Torque $(T^*)$

Mass flow rate (W)

Pressure ratio (r)

Rotational speed (N)

The mass flow rate was measured by means of the choked turbine nozzles for all tests at design relative Mach number of 1.8.   However, some of the tests conducted at transonic rotor approach velocities utilized orifices (designed to ASME specifications) for flow measurement, installed in series with the turbine nozzles.   An attempt was made to determine flow coefficients for the turbine nozzles by using the orifices as a standard. The results indicated that unacceptable dispersions in the flow rate measurements existed when the measurement was based on the orifice. These dispersions are possible due to errors in the measurement of pressure level at the orifice inlet.   Although the pressure drop across the orifice was measured accurately with a manometer, the inlet pressure was measured with a bourdon gage.

It was decided that the turbine nozzles would be used as a basis for flow measurement for all the tests.   Since these nozzles were operating in the choked condition, the only measurements required were the inlet total pressure and temperature.   The coefficient of discharge was assumed to correspond to that of an ASME long radius nozzle (Reference 1) with a diameter ratio of 0.6.   This diameter ratio is representative of the actual ratios in the turbine nozzles (0.309 to 0.785), but is biased toward the high ratio (low discharge coefficient) value to compensate for the fact that the nozzles, although smooth, do not conform to the ASME standards in shape.   A polynomial curve fit of the discharge coefficient curve was developed and all test data were reprocessed in a digital computer program. The estimated error in flow measurement is ±3.0 percent.

Torque measurements are believed to be excellent due to the torque measurement technique developed for these tests (Section 5.2.7).   The error in the torque measurement is estimated to be 0.5 percent or lower.

Rotational speed and pressure ratio were relatively straightforward measurements and are estimated to be in the 0.2 percent category. The pressure ratio, together with the inlet temperature and gas properties, enters into the calculation of the isentropic enthalpy drop. The error in the isentropic head is estimated at 0.4 percent.

The estimated errors were combined into a root-mean-square avera to provide an estimate of the overall accuracy of the efficiency measuremen

$$\left(\frac{\Delta\eta}{\eta}\right)^2 = \left(\frac{\Delta T^*}{T^*}\right)^2 + \left(\frac{\Delta N}{N}\right)^2 + \left(\frac{\Delta W}{W}\right)^2 + \left(\frac{\Delta(h_{is})}{h_{is}}\right)^2 \tag{1}$$

As a result, the turbine efficiency measurements are estimated to bε accurate to within 3.08 percent, the error being primarily due to flow rate measurement uncertainty.

Since the primary objective was to obtain the variation in turbine efficiency with Reynolds number, the absolute accuracy of the efficiency measurement is actually of secondary importance. Thus, the curves which will present normalized efficiency, $\eta/\eta_{Re=\infty}$, are held to be more accurate than the 3.08 percent quoted above. This is particularly true in cases wherε a large range in Reynolds number was tested in a given day's testing, thus eliminating any effect of systematic errors which might appear when the tests are conducted over a long period of time.

## 6.1.2 Single Stage Axial Turbine Tests

The test data were evaluated by calculating the torque coefficient $\tau$ efficiency $\eta$ and turbine velocity ratio u/co for different back pressures. The turbine velocity ratio was computed from the mean wheel speed (referre to the mean rotor diameter D = 5.95") and the isentropic velocity

$$c_o = \sqrt{2g \frac{k}{k-1} RT_1 \left[1 - \left(\frac{P_3}{P_1}\right)^{\frac{k-1}{k}}\right]} \tag{2}$$

when $P_1/P_3$ denotes the overall turbine pressure ratio, R the gas constant, k the ratio of specific heats and $T_1$ the total turbine inlet temperature.

The test data are plotted by presenting the torque coefficient as a function of turbine velocity ratio whereby the torque coefficient is defined by

$$\tau = \frac{T^*g}{c_o W D} \tag{3}$$

when $T^*$ denotes the torque and W the turbine weight flow.

This method of presentation allows a fair assessment of the accuracy of the data since the torque coefficient is expected (in impulse turbines) to vary in inverse proportion to the turbine velocity ratio. The turbine efficiency is directly interrelated with the torque coefficient since

$$\eta = 4\tau \, \frac{u}{c_o} \tag{4}$$

The turbine efficiency was then calculated from the linearized interrelation between torque coefficient and turbine velocity ratio.

### 6.1.2.1    Supersonic Design (Single Stage)

The test data are shown in Figure 14 by plotting the torque coefficient as function of turbine velocity ratio for constant back pressures. The expected linear interrelation was confirmed by the test data; the torque decreases with decreasing back pressures. The efficiency was calculated from these data. These data are shown in Figure 15 indicating that the peak efficiency decreases with decreasing back pressures, i.e., decreasing Reynolds numbers and that the optimum turbine velocity ratio also decreases with decreasing Reynolds numbers. The Reynolds numbers listed at the different curves is the machine Reynolds number or peripheral Reynolds number for the optimum turbine velocity ratio where the peripheral Reynolds number is defined

$$Re^* = \frac{u \, D}{v_3} \tag{5}$$

u denoting the wheel speed at the mean wheel diameter D and $v_3$ denoting the kinematic viscosity at rotor exit.

### 6.1.2.2    First Transonic Design

The calculated torque coefficients for this configuration are shown in Figure 16 as a function of the turbine velocity ratio, showing again a linear tendency and a decrease in torque coefficient with decreasing back pressures. The measured data agree fairly well with the expected tendencies. The efficiency as function of turbine velocity ratio is shown in Figure 17. These indicate the same trends as found in the supersonic design, but considerably lower efficiency levels for corresponding Reynolds numbers. The unexpected low efficiency was attributed to the comparatively large trailing edge thickness (te/t = .172 at mean radius but larger at all other places due to the elliptical nozzle exit shape) and the large difference

between nozzle heights and rotor blade heights ($h_R/h_N$ = .75).  These

design features cause large wakes behind the nozzles and thus comparatively high losses.  The Reynolds numbers indicated in Figure 17 refer to the peripheral Reynolds numbers at the optimum turbine velocity ratio.

It is likely that the torque coefficient and efficiencies are quoted low by 1.5 percent since a nozzle area coefficient of .98 has been assumed for the evaluation whereas actually in later tests (Section 6.1.2.3) an area coefficient of .965 was found experimentally.

6.1.2.3      Second Transonic Design

The calculated torque coefficients for this configuration are shown in Figure 18 as a function of turbine velocity ratio for different back pressures.  Considerable scatter in the data is evident which makes it difficult to coordinate the data and to arrive at definite conclusions. Figure 19 shows a likely estimate of the efficiency values, again revealing comparatively low efficiencies.

It was suspected that the data scatter might be due to aerodynamic instability observed in the Reynolds number experiments of Reference 4. In order to investigate this aspect, additional test runs were made where the sequence of the test operation was changed in such a manner that the turbine was started and the speed gradually increased up to the maximum value, then reduced, then increased again and then reduced.  The data obtained this way for an inlet pressure of 1.3 psia are indicated by circles in Figure 20, the numbers indicate the order of sequence.  No definite trend pointing to an aerodynamic instability could be associated with these test data.  It was discovered during these runs that the speed indication w.s erratic.  A subsequent check of the instrumentation indicated malfunctioning of the speed indicators.

The weight flow in these tests was measured separately by a metering orifice.  The resulting data are plotted in Figure 21 by showing the weight flow parameter as function of the gas inlet temperature.  A constant value for the weight flow parameter would be expected since the nozzles were choked.  Figure 21 shows, however, increasing values of the weight flow parameter with increasing gas temperatures for the original runs.  This implies erroneous readings or falsification of the indicated temperatures by heat transfer phenomena.  More consistent data regarding the weight flow parameter were obtained in the repeat runs, indicated in

Figure 21 by circles. These data show no temperature trend but a comparatively large scatter. It is also observed that for choked nozzles a somewhat higher weight flow would have to be expected as indicated by the solid line in Figure 21. This line was calculated by the relation

$$\frac{W\sqrt{T_1}}{P_1} = \frac{A_N}{\sqrt{R}} \ \psi^* \tag{6}$$

with

$$\psi^* = \sqrt{2g \ \frac{k}{k-1} \left[ \left(\frac{P_2}{P_1}\right)_{cr}^{\frac{2}{k}} - \left(\frac{P_2}{P_1}\right)_{cr}^{\frac{k-1}{k}} \right]} \tag{7}$$

assuming that the effective nozzle area is equal to the geometric nozzles area. The test data indicate that the ratio of effective throat area to geometrical nozzle area is about .965, a reasonable value. Actually this value would be expected to decrease with decreasing back pressures, i.e., decreasing Reynolds numbers. The accuracy of the test data was insufficient to establish such a relationship.

The nozzle section of this design was instrumented in great detail in order to learn more about the flow mechanism. Pressure taps were provided in the throat area of nozzle 8 (measuring station 51) at the down-stream area of the nozzle 7 (measuring station 61) at the exit area of nozzle 1 (measuring station 80) and nozzle 14 (measuring station 81) and at the exit of nozzle 9 and 10 (measuring stations 62 and 63). The pressure along the flow path in the collector was also measured at the beginning, in the middle and at the end of the collector. The average value indicated by these taps was considered a valid indication of the turbine inlet pressure and denoted as $P_{in}$. The total pressure at the inlet of the first nozzle was also measured and denoted as $P_{4-c}$. The static pressure at the inlet of the last nozzle was denoted with the symbol $P_{4-B}$. All these pressures were evaluated and are plotted as a function of the turbine velocity ratio for the different test runs in Figures 22, 23 and 24. The trends indicated by these data may be discussed as follows: The total pressure at the inlet of the first nozzle was slightly lower than the average inlet pressure in the collector indicating an erroneous reading of the total pressure or an optimistic assessment of the averaged inlet pressure. When the measured total pressure at the inlet of

the first nozzle is compared with the measured static pressure at the inlet of the last nozzle, a comparatively small difference between these readings is evident. Since the velocity at the inlet of the last nozzle is of fair magnitude and since additional losses in the collector have to be accounted for, it appears that the total pressure reading at the first nozzle is on the low side

The static pressure in the nozzle throat differs from the turbine inle pressure by a constant value as was expected. A different and initially surprising trend is shown by the static pressure readings at nozzle exit. All these pressures (61, 62, 63, 80, 81) increases with increasing turbine velocity ratios. It is evident for example in Figure 22 that the pressure at nozzle exit is even higher than the pressure at the throat. The pressure readings indicate that the degree of reaction increases with increasing turbine velocity ratios and that at high $u/c_o$ operation the diverging section

of the converging diverging supersonic nozzle acts as a diffuser. This is particularly evident at low back pressure operation (Figure 22) still evident at the mean back pressure value (Figure 23) and to a lesser degree at the high back pressure runs (Figure 25). These data imply that the desired impulse action is not achieved. This is shown more conclusively in Figure 25 by calculating the degree of reaction for the different runs defined by

$$\rho = \frac{H_{rotor}}{H_{turbine}} \tag{8}$$

where $H_{rotor}$ is calculated from turbine inlet temperature, the pressure $P_{in}$ and $P_{80}$, and where $H_{turbine}$ is calculated from turbine inlet temperatur $P_{in}$ and $P_{ex}$. The arrows in this diagram refer to the approximate location of the peak efficiency. It is evident that degrees of reaction as high as 78 percent were obtained in the optimum efficiency regime for low Reynolds numbers but that the degree of reaction at optimum $u/c_o$ decreased to about

66 percent for the high Reynolds Number operation.

The ratio of averaged inlet pressure to measured nozzle throat static pressure is shown in Figure 26 for the different runs, indicating an average ratio of 1.64 instead of 1.88, expected for choked nozzle conditions. An inspection of the location of pressure tap 51 revealed that it was actually located before the geometrical throat and thus did not measure the static throat pressure but a somewhat higher value.

Reentry Axial Turbine

The calculated torque coefficient and efficiencies for this
turbine are shown in Figures 27 and 28 indicating the expected trends.  The
efficiency decreases with decreasing back pressures, i. e., decreasing
Reynolds numbers together with the optimum turbine velocity ratio.

6. 2      ANALYSIS OF TEST DATA

6. 2. 1   Single Stage Axial Turbines

6. 2. 1. 1           Special Aspects of Transonic Turbine Designs

Flow phenomena associated with rotor choking are likely
to occur in impulse turbines operated at pressure ratios of 5 to 1.   These
phenomena can be recognized by a simplified analysis of the flow process.
The most important aspects are brought to light if the continuity relation
is applied to the flow process between nozzle and rotor.   The detailed
derivation of the pertinent relations are quoted in the appendix.   The
significant relation here is Equation 31 which indicates that a certain
minimum degree of reaction is required in order to satisfy the continuity
relation and that this minimum degree of reaction is a function of the nozzle
throat area $A_N$, rotor throat area $A_R$, turbine velocity ratio and overall
turbine pressure ratio.   Using now the pertinent data of the supersonic design
(single stage) and calculating the minimum degree of reaction, according to
Equation 31, Figure 29 is obtained which indicates (solid line) that the
minimum degree of reaction is negative for an $x^*$ value of 1, i. e., if the
full geometrical rotor throat area is available for the flow.   Thus this
turbine could still operate as a true impulse turbine for the ideal case.
Actually, a boundary layer displacement thickness has to be anticipated
which decreases the effective rotor throat area.   The effect of the boundary
displacement thickness is indicated by the dashed lines in Figure 29.   These
are denoted by $x^* = 0.8$ and $x^* = 0.6$, meaning that the effective rotor throat
area is only 80 percent or 60 percent respectively of the geometrical throat
area.   It is evident from these lines that even with an $x^*$ value of 0.6 impulse
action can still be accomplished by the turbine at turbine velocity ratios of
0.48.   No rotor choking effects to impair the characteristic, would have to
be anticipated for this design.

The situation is somewhat different for the first transonic design.
The pertinent data are shown in Figure 30 by plotting the minimum required
degree of reaction for different values.   It is evident that for $x^* = 0.8$ impulse
action can still be accomplished at velocity ratios as high as 0.51 but that
for an $x^*$ value of 0.6 impulse action can only be expected up to turbine

velocity ratios of .32 and that a minimum degree of reaction of about 0.31 would have to be anticipated for a turbine velocity ratio of 0.45 in cases where $x^* = 0.6$. Thus for a moderate boundary layer displacement thickness, this turbine geometry would be likely to operate as an impulse turbine over most of the operating range.

A different situation exists in the second transonic design as indicated in Figure 31. Even for the ideal case ($x^* = 1$), true impulse action can only be expected up to turbine velocity ratio of 0.31. At a turbine velocity ratio of 0.4 a reaction of about 60 percent would have to be expected with a value of 0.8 for $x^*$ and 91 percent for $x^*$ values of 0.6

Thus this turbine design is highly sensitive to any boundary layer displacement thickness occurring in the rotor throat. This is due to the elimination of the comparatively large trailing edge thickness in the first transonic design and to the selection of nozzle exit heights almost equal to the rotor blade heights (in contrast to the first transonic design where the nozzle exit heights were significantly smaller than the rotor blade heights).

It is interesting to compare the measured degrees of reaction reported in Figure 25 with the calculated minimum degrees of reaction. This comparison is shown in Figure 32 and indicates that x values of about 0.65 occurred at low Reynolds numbers but only $x^*$ values of 0.75 at high Reynolds number operation. The rotor approach vector was mismatched with the blade angle. This caused the second transonic design to operate with a considerable degree of incidence and have very high losses in the maximum efficiency range. Thus it cannot be expected that the experimental data shown for the second transonic design indicate the maximum possible efficiency values and therefore reflect a somewhat distorted Reynolds number influence. These data are nevertheless typical for the particular turbine type described, a symmetrical rotor blade design intended for impulse action and operated at varying Reynolds numbers.

The test data of the first transonic design also reflect a somewhat distorted Reynolds number influence since high wake and mixing losses have occurred due to the comparatively large nozzle trailing edge losses and due to the large ratio of blade heights to nozzle heights. This means that both transonic designs had undue losses, probably of the non-viscous type and therefore not significantly affected by the Reynolds number. In contrast, the supersonic design did not suffer from these shortcomings so that in this case most of the losses would tend to be of the viscous type so that the measured efficiency trends are more likely to represent a typical Reynolds number influence.

It is also interesting to apply Equation 31 of the appendix to the geometry of the turbine used in the Reynolds number program reported in Reference 4 and to calculate the minimum degree of reaction for varying

$x^*$ values. A diagram as shown in Figure 33 results for this turbine, which operates at a pressure ratio of two. Figure 32 indicates no impairment in impulse operation at $x^* = 1$, but a significant influence of boundary displacement thickness on the minimum degree of reaction requiring for example degrees of reaction of 62 percent at a turbine velocity ratio of .4 for an $x^*$ value of .8. This indicates that, although turbines operating at pressure ratios of 5 to 1 are most sensitive to rotor choking affects as demonstrated in Figure 49 of the appendix, impulse turbines operating at pressure ratios of 2 can also show severe effects of choking and therefore an unduly high degree of reaction in cases where a comparatively large boundary layer displacement thickness has to be anticipated. This would tend to explain the surprisingly low efficiencies and the compr atively small Reynolds number effects found in Reference 4. It appears that the turbine was operating at high degrees of reaction in the optimum efficiency regime. This mode of operation would cause incidence losses which would tend to increase the percentage of the non-viscous type losses unduly so that the true Reynolds number effect is obscured. Since it is known from single airfoil tests, (Reference 5) that aerodynamic instability is likely to occur at incidence conditions (but less likely at zero incidence) and low Reynolds number operation, it could be thought that the aerodynamic instability described in Reference 4 was at least partly due to oblique angles of attack at rotor inlet. The test data are nevertheless typical for the particular type of geometry tested.

### 6.2.1.2    Available Information on Reynolds Number Influence

In order to recognize the significance of the test data it is helpful to give a short resume of the theoretical aspects of the Reynolds number influence and of the experimental data found in the literature.

The Reynolds number is a parameter which expresses the ratio of the viscous and dynamic forces acting on the flow. It refers to phenomena taking place in the boundary layer, i.e., in the immediate vicinity of the channel wall surfaces. The classical considerations dealing with similarity in flow phenomena state that the flow characteristic of two geometrically similar channels are identical only as long as the Reynolds number has the same numerical value when the Reynolds number is defined by

$$Re = \frac{v L}{\nu} \tag{9}$$

i.e., the product of a characteristic velocity v and a characteristic length L divided by the kinematic viscosity $\nu$. It is customary for airfoil con-siderations to use the chord length C as the characteristic length and the

approach velocity as the characteristic velocity.  For channel flows the hydraulic diameter or hydraulic radius is usually taken as the characteristic dimension.  This 's particularly the case when a definite flow pattern has been established, that is after the "initial length", whereby "initial length" refers to that section of the channel where the boundary layer starts forming and develops into a laminar or turbulent pattern.  This length is a multiple of the channel diameter so that typical turbomachinery cascades will be in the "initial length" zone if viewed from a channel flow point of view.  This regime is little explored so that channel flow considerations contribute comparatively little to the recognition of the flow characteristic to be expected in typical turbomachinery cascades.  In contrast the airfoil theory, particularly the boundary layer behavior around the airfoil, is investigated in great detail experimentally as well as theoretically.

It thus appears that the airfoil theory provides a better frame of reference for investigating the essential characteristics of typical turbomachinery cascades.  Thus the chord length appears to be the most suitable expression for the characteristic length.  The proper selection of the reference velocity poses a problem since in most cascades (with the possible exception of typical impulse rotors) the velocity changes with chord length and in typical turbine cascades is usually larger at cascade exit than at cascade inlet.  Since the boundary layer behavior is particularly critical at the first section of the chord it appears reasonable to retain the inlet velocity, i. e. , approach velocity to the cascade, as the reference velocity.  It must be realized, however, that most of the published turbine cascade data refer the Reynolds number to either the exit velocity or to an average velocity (e. g. Reference 6, 7).

A typical behavior of the boundary layer is shown in Figure 34 which indicates that the boundary layer is laminar in the first part of the chord until the Reynolds number (formed by using the running chord length x as the characteristic dimension) reaches a critical value.  In this regime the displacement thickness $\delta^*$ grows with the square root of the distance x from the leading edge (Reference 8).

$$\delta^*_{lam} = 1.73\sqrt{\frac{x\nu}{c_i}} \tag{10}$$

where $c_i$ denotes the velocity outside of the boundary layer.  In Equation (10) the boundary layer displacement thickness is defined by the relation

$$\delta^* = \int_0^\delta \left(1 - \frac{v}{c_i}\right) dy \tag{11}$$

i. e. , expresses the geometrical displacement of the outer flow due to
boundary growths. The boundary layer transforms into a turbulent boundary
layer at the instability point. At this point the displacement thickness
decreases to one-half of its previous value and increases now in the
turbulent regime with the 0. 8 power of the distance. The turbulent boundary
layer grows with this rate until it becomes separated. A criterion for the
point of boundary layer separation is found by the form factor

$$H = \frac{\delta^*}{\theta}$$                                 (12)

when $\theta$ denotes the boundary layer momentum thickness defined by

$$\theta = \int_0^\delta \frac{v}{c_i} \left(1 - \frac{v}{c_i}\right) dy$$                (13)

Usually form factor values of $H = 4$ are considered critical and indicate
separation of a laminar boundary layer whereas a form factor of 2 is
associated with the separation of a turbulent boundary layer (Reference 6).

These relations were first established by investigations of a flat plate.
This is a comparatively simple case aerodynamically, since the velocity in
the outer flow remains almost constant and no change in velocity vectors is
intended. This is not the case for typical turbomachinery cascades, since
it is the purpose of these cascades to effect a flow deflection which usually
is connected with a change in velocity. This change in velocity causes a
decrease in the pressure, i. e. , a positive pressure gradient in compressor
cascades, which tends to make the boundary layer even more unstable and
in most cases causes early separaion. In contrast the flow in typical
turbine cascades (with the possible exception of the impulse rotor blade)
tends to be accelerated, i. e. , has a negative pressure gradient which tends
to stabilize the boundary layer and thus affects the point of transition.
It also has to be recognized that the degree of turbulence influences the
critical Reynolds number (Reference 9) and thus the point of transition, and
that the degree of turbulence tends to be different in typical stators and
typical rotors of single stage machines.

It must be emphasized that the above considerations deal only with
design point operation, i. e. , "zero incidence" approach vector to the
cascade. Additional variations of the characteristic, particularly in regard
to the transition point and separation point of the boundary layer have to be
anticipated in cases where "incidence effects" are also considered
(Reference 10).

The development of a boundary layer along the wall surface causes energy losses which are commonly referred to as profile losses or primary losses. Additional losses occur at the hub and tip section of the cascade. The interrelation of these losses with the cascade geometry and Reynolds number is not too well established at present. This is partly due to the difficulty in distinguishing clearly between primary and secondary losses in the available test evidence. This may be demonstrated by Figure 35 where the observed local losses are plotted against blade length (Reference 11). It is evident that the losses in the middle section are fairly constant but increase toward the hub shroud and the tip. The losses in the tip regime are particularly large due to the finite clearance between blade tip and (stationary) tip shroud. It appears reasonable to assume that the primary (profile) losses are constant over the blade lengths so that the shaded area in Figure 35 may be considered to represent the primary losses and the cross hatched area may be considered to represent the secondary losses.

It appears to be generally agreed that the hub losses depend on the aspect ratio and the Reynolds number, but are comparatively small. In contrast the tip clearance losses in unshrouded rotors can be of significant magnitude, particularly in cases where the ratio of clearance to blade heights is more than 3 percent. Test data reported in Reference 11 seem to indicate that these losses are entirely independent of Reynolds numbers whereas other sources (Reference 7) indicate that they might be dependent on Reynolds number (but possibly not to the same degree as the primary losses).

Furthermore the wheel disc friction losses have to be considered. They are comparatively well investigated analytically as well as experimental (Reference 12) and show a definite dependency on the Reynolds number.

In summarizing the available information it appears justified to distinguish between losses which are of the viscous nature (interrelated with the Reynolds number) and losses which are of the non-viscous nature, (caused primarily by eddy formation or mixing), and which may depend on the Reynolds number to a small degree, if at all.

For the lack of more definite evidence it may be assumed that the losses in turbomachines are of two different types; the viscous losses depend on Reynolds number, and the non-viscous losses independent of Reynolds number. On this basis the ratio of the viscous to the non viscous losses deno. as $v^*$ becomes an important criterion for the assessment of the Reynolds number influence.

It is therefore evident that the Reynolds number influence tends to be complex and will depend on many different parameters; the most important ones being the degree of turbulence, the critical Reynolds number and the

ratio of viscous to non-viscous losses. The expected trends of the different influences are described in detail in Reference 13 where an attempt has been made to estimate the influence of the Reynolds number on the losses in typical turbomachines by speculating on the likely numerical values of the different parameters. It was found convenient to define a turbomachine Reynolds number

$$Re^* = \frac{u\,D}{\nu} \tag{14}$$

i.e., to use the wheel speed as reference velocity and the rotor diameter as reference values, and to relate the stator and rotor Reynolds parameter to $Re^*$. This interrelation was made on the basis of similarity considerations, so that the similarity parameters, specific speed ($N_s$) and Mach number

(represented by density ratio across the turbine), became distinguishing parameters. On this basis an interrelation between efficiency (represented by an efficiency ratio) turbomachine Reynolds number, specific speed and Mach number (represented by density ratio) was calculated. This is shown in Figure 36. This diagram indicates that the Reynolds number effect is large for low pressure ratio, (low Mach number machines and low specific speed designs), but less pronounced in high Mach number operation and high specific speed designs. These calculated trends agree fairly well with the available test evidence as indicated by the dotted line and shaded area in Figure 36.

6.2.1.3      Comparison of Test Data with Data From Other Sources

Figure 37 shows the maximum efficiency values for the supersonic turbine quoted in Figure 15, plotted against the machine Reynolds number $Re^*$ (solid line) together with the maximum efficiencies of the two transonic designs quoted in Figures 17 and 19. A Reynolds number regime from $1.4 \times 10^4$ to $3 \times 10^5$ is covered by these data. It is evident from the considerations reported in Reference 13, that the Reynolds number influence can not be presented by a simple power law since several factors with sometimes opposing trends have to be considered. It is customary to express the Reynolds number influence on the turbine efficiency by a relation of the form

$$\frac{1 - \eta_1}{1 - \eta_0} = \left(\frac{R_{e-0}}{R_{e-1}}\right)^x \tag{15}$$

and to assume that the exponent x has a value of 0.5 in the laminar flow regime and a value of 0.2 to 0.25 in the turbulent flow regime. These values would be

appropriate when all the losses are of the viscous type.  Since some of the losses appear of the non-viscous type and therefore are not dependent on the Reynolds number, lower values for the exponent have to be expected. Actually, the x-values would be expected to decrease with decreasing v ' values

It almost must be observed that the boundary layer in typical turbine cascades may be partly laminar and partly turbulent.  Thus some of the losses may be comparatively high but will have a low Reynolds numbe exponent (turbulent boundary layer), whereas other losses may be comparatively small at high Reynolds numbers but will rise steeply with decreasing Reynolds numbers (laminar boundary layer).  A criterion for the partition of the losses into laminar and turbulent is the critical Reynolds number.  This Reynolds number depends on the pressure gradient along the flow path, on the Mach number and on the degree of turbulence, i.e., it is different in the rotor and stator.

Figure 38 shows the local (as contrasted to integrated) values of the exponent x as a function of the machine Reynolds number, calculated from Figure 36.  The trends may be described as follows:  For $N_s$ = 60 and $\gamma_{1/\gamma_3}$ = 2, the ratio $v^*$ is high but the critical Reynolds number is low. Thus the percentage of the viscous losses is high.  At $Re^*$ = 2 × 10$^6$ most of the boundary layer is turbulent and therefore x is small.  At lower $Re^*$ value the boundary layer becomes increasingly laminar and x increases, approachi the "all laminar" value of .5.  For $N_s$ = 60 and $\gamma_{1/\gamma_3}$ = 10, the $v^*$ value is . ' Thus smaller x values would be expected than the ones shown for $\gamma_{1/\gamma_3}$ = 2. However, since the critical Reynolds number has increased, a larger part of the boundary layer is now laminar, causing a larger x value than calculate for $N_s$ = 60 and $\gamma_{1/\gamma_3}$ = 2.  This trend is continued for $N_s$ = 300 and $\gamma_{1/\gamma_3}$ = i At $N_s$ = 300 and $\gamma_{1/\gamma_3}$ = 10, the critical Reynolds number is again higher thar for the previous cases but the $v^*$ value is particularly low.  Thus low x value: occur at high Reynolds numbers.

Figure 39 shows the local Reynolds number exponent calculated from the test data of the supersonic (single stage) turbine.  This was done after correcting the measured (total to static) efficiency to the (total to total) efficiency used for the calculated Reynolds number data in Figure 38.  For this correction the relation

$$\eta_t = \frac{\eta_{st}}{1 - \left(c_3/c_o\right)^2}$$

(16)

was used when $c_3$ denotes the absolute leaving velocity at rotor exit
$(c_3^2/c_0^2 \cdot 1)$   The test data would be expected to approximate the x values calculated for $N_s = 60$ and $\gamma_1/\gamma_3 = 10$ (dashed line in Figure 41), but to be of generally smaller magnitude since $v^*$ for $N_s = 38$ (test turbine) tends to be lower than $v^*$ for $N_s = 60$ (Reference 14). Also the test turbine had a larger trailing edge thickness (te/$t$ = .239) than assumed (te/$t$ = .02) for the calculated Reynolds data, i.e. the test turbine had a larger amount of "non-viscous" losses. Assuming that these losses absorb 11 percent of the energy, the dotted line in Figure 39 is obtained which shows fair agreement with the dashed line but indicates lower x values at low Reynolds numbers and higher x values than precalculated at high Reynolds numbers. This implies that the studies presented in Reference 13 tend to overestimate the Reynolds number influence somewhat at low Reynolds numbers but underestimate its effect somewhat at high Reynolds numbers.

A comparison of the tested efficiencies for the first transonic design (corrected to total to total efficiency) with the precalculated data is shown in Figure 40. A considerable discrepancy is evident, the test data showing significantly lower x values than precalculated. It must be observed however, that the specific speed of the test turbine is again lower than assumed for the precalculated data. Comparatively large (non-viscous type) wake losses have also occurred in the test turbine. This is due to the difference in nozzle heights and rotor blade heights ($h_N/h_R$ = .75) and to the large nozzle edge trailing edge thickness, in addition to the large rotor blade trailing edge losses. Assuming that these losses have absorbed 21 percent of the energy, the dotted line in Figure 42 is obtained which shows reasonable agreement with the precalculated data.

It is evident from an inspection of Figure 37 that the test data of the second transonic design exhibit a trend similar to the test data of the first transonic design, i.e., they have a lower $v^*$ value than originally expected. This is attributed to the comparatively large incidence losses in the maximum efficiency regime, caused by rotor choking effects demonstrated and discussed in Section 6.2.1.1. These losses can be classified as a type which is influenced by the Reynolds number only to a comparatively small degree. It is therefore apparent that the test data will reflect a smaller Reynolds number influence (and lower efficiency level) than should be expected from a design which operates without incidence at the optimum velocity ratio.

Thus no valid comparison between test and calculated data can be made for the transonic designs on the basis of the presently obtained experimental evidence.

6.2.1.4    Re-entry Turbine

An analysis of the interstage leakage losses is of particular interest for this design. These losses can be evaluated from the measurements since a first-stage choked nozzle and a second stage choked nozzle can be assumed. Thus the weight flow passing through the first stage and the weight flow passing through the second stage can be evaluated on the basis of the pressure and temperature measurements at first and second stage nozzle. The difference between these two values is the interstage leakage. The calculated data are plotted in Figure 41 as a function of turbine velocity ratio for the different back pressures. Two different types of leakages have to be anticipated, a static leakage occurring behind the first nozzle and behind rotor exit of the first stage, and a carry-over leakage due to the rotation of the wheel. These are described in detail in Reference 2. The carry-over leakage would be expected to be proportional to the turbine velocity ratio. The static leakage would be expected to be independent of turbine velocity ratio and depend more on pressure ratio and possibly Reynolds number. The calculated data shown in Figure 41 indicate that at stall a comparatively high leakage of about 15 percent occurred for all back pressures, and that the leakage increases slightly with turbine velocity ratios at low back pressures and to a somewhat larger degree at high back pressures. This would imply that no Reynolds number effect exists for the static leakage but that a small Reynolds number effect may exist for the carry over leakage. It was originally expected that the static leakage would decrease slightly with decreasing pressures since this leakage should be affected by the resistance coefficient in the leakage area. which in turn would be expected to increase with decreasing Reynolds numbers. Comparing the tested leakage data with calculated data from Reference 2 (dashed line in Figure 41) it is found that the actual observed leakage is about twice the calculated amount. It is evident that this discrepancy is due mainly to a difference in the static leakage.

The test data can be used to calculate the performance of the first-stage since the second-stage of the re-entry turbine is identical to the single-stage turbine described in Section 6.1.2.1. Assuming that all leakage has occurred between the rotor exit of the first-stage and the re-entry duct inlet, torque coefficients as shown in Figure 42 are calculated for the first-stage. The data show the expected trend; there is no appreciable Reynolds number influence due to the high pressure level. From these data the efficiency is calculated, Figure 43 revealing a peak efficiency of 68.5 percent for a specific speed of $N_s = 10.5$. Considering that some leakage actually occurred between first stage nozzle exit and first stage rotor inlet, the actual first stage efficiency would be higher by this leakage than shown in Figure 43 (in percent of total flow). It is

interesting to note that the efficiency obtained in the first stage is higher than could be expected from a single stage partial admission turbine designed for a specific speed of 10.5 (Reference 14). This was to be expected since a single stage partial admission turbine will have losses in the unadmitted part of the rotor due to friction and pumping i e losses which will not occur in the re-entry turbine.

Figure 44 shows the head and power split between first and second stage indicating that the first stage expands more head than the second stage The first stage also develops more power than the second stage and that this trend increases with increasing turbine velocity ratios. This trend was to be expected since the inlet temperature to the second stage decreases with increasing velocity ratios due to the temperature drop in the first stage. The pressure ratio in the first stage increases with increasing velocity ratios since this value is fixed by the relation

$$\left(\frac{P_1}{P_3}\right)_I = \frac{A_{N-II}}{A_{N-I}} \frac{\psi_{II}^*}{\psi_I^*} \sqrt{\frac{T_I}{T_{II}}} \frac{1}{1 - \% \text{ leakage}} \tag{17}$$

derived from the continuity condition, ($T_{I/T_{II}}$ and the leakage increase with increasing turbine velocity ratios.)

The peak efficiencies of the reentry turbine shown in Figure 28 are presented in Figure 45 as a function of the machine Reynolds number. It is apparent that the Reynolds number influence is small. This was to be expected since the first stage is hardly affected by the Reynolds number and contributes about 70 to 80 percent of the total power at the optimum velocity ratio.

## 7 0  SYMBOLS AND REFERENCES

## 7 1  LIST OF FIGURES

## 7.2    LIST OF SYMBOLS

A       Area

c       Velocity

$c_o$     Spouting Velocity

D       Mean Wheel Diameter

$D_s$     Specific Diameter

g       Gravitational Constant

H       Shape Factor

h       Blade Heights

L       Length

M       Mach Number

N       Rotational Speed

$N_s$     Specific Speed

p       Pressure

R       Gas Constant

Re      Reynolds Number

r       Pressure Ratio

s       Tip Clearance

T       Temperature

$T^*$     Torque

t       Blade Spacing

$t_e$     Trailing Edge Thickness

u       Mean Wheel Speed

| | |
|---|---|
| V | Velocity |
| V | Ratio of Viscous to Non-Viscous Losses |
| W | Weight Flow |
| w | Relative Velocity |
| x | Distance from Leading Edge   Reynolds Number Exponent |
| x' | Ratio of Free Flow Area to Geometrical Area |
| $\alpha$ | Nozzle Angle |
| $\beta$ | Rotor Angle |
| $\gamma$ | Density |
| $\delta$' | Boundary Layer Displacement Thickness |
| $\delta$ | Boundary Layer Displacement Thickness |
| $\eta$ | Efficiency |
| k | Ratio of Specific Heats |
| $\rho$ | Degree of Reaction |
| $\tau$ | Torque Coefficient |
| $\nu$ | Kinematic Viscosity |
| $\psi$ | Nozzle Coefficient |

Subscripts

| | |
|---|---|
| N | Nozzle |
| R | Rotor |
| i | Ideal |
| in | Inlet to the Turbine |
| ex | Turbine Exit |
| 2 | Before Rotor |
| 3 | After Rotor |
| I | First Stage |
| II | Second Stage |

## 7.3    REFERENCES

1.  Amendment Number 6 to ONR Contract Number NONR 2292(00)
February 1, 1960

2.  H. D. Linhardt:"Study of Turbine and Turbopump Design Parameters. "
Final Report, Volume I, A Study of High Pressure Reentry Turbines"
Sundstrand Aviation-Denver Report No. STD 1735

3.  R. G. Adams: "The Effect of Back Pressure on Reentry Turbine
Performance" Interim Report Sundstrand Aviation Denver, Report Number
CDR D 62:7012

4.  R. Y. Wong and W. J. Nusbaum: "Air Performance Evaluation of a 4. 0
Mean Diameter Single Stage Turbine at Various Inlet Pressures from . 14
to 1.88 Atmospheres and Corresponding Reynolds Numbers from 2500 to
50, 000".   NASA Report TS Number D-1315

5.  K. Kramer:  "Airfoils in the Critical Reynolds Number Regime"
(in German) Forschung auf dem Gebiete des Ingenieur wesens,  1961
Page 33 to 46

6.  H. Schlichting:  "Application of Boundary Layer Theory in Turbomachinery".
ASME Journal of Basic Engineering Volume 81, Series D, 1959, Page 543 to 551

7.  Stuart, Whitney and Wong: "A Study of Boundary Layer Characteristics in
Turbomachine Blade Rows and their Relation to Overall Blade Loss".
Transactions ASME Journal of Basic Engineering Volume 83, Series D
Number 3, September 1960

8. Betz: "Introduction into the Theory of Flow Machines" (In German) 1959 G. Braun, Karlsruhe

9. T. Bahr: "Investigations on the Influence of Reynolds Number and Mach Number of the Flow Through Cascades" (in German) TFL Report Number 078 Braunschweig 1960

10. H. G. Roden: "Effects of Reynolds Number on the Flow of Air Through a Cascade of Compress Blades" ARC Technical Report R and M No. 2919

11. H. Schlichting and A. Das: " Recent Research on Cascade Flow Problems" DFL Report 202 Braunschweig

12. H. Schlichting: "Boundary Layers Theory" McGraw-Hill 1961

13. O. E. Baljé: "A Study on Reynolds Number Effects in Turbomachines" Presented at the ASME Reynolds Number Symposium, 1963

14. O. E. Baljé: "A Study of Design Criteria on Matching of Turbomachine" ASME Transaction, Engineering for Power, January 1962

15. J. H. Horlock: "Further Comments on Losses and Efficiencies in Axial Flow Turbines" International Journal of Mechanical Sciences, Volume 2, No. 4, April 1961, page 3

16. J. Neustein: "Experiments at Low Reynolds Numbers" California Institute of Technology, Hydrodynamics Lab Report No. 6, 1957

8.0    ILLUSTRATIONS
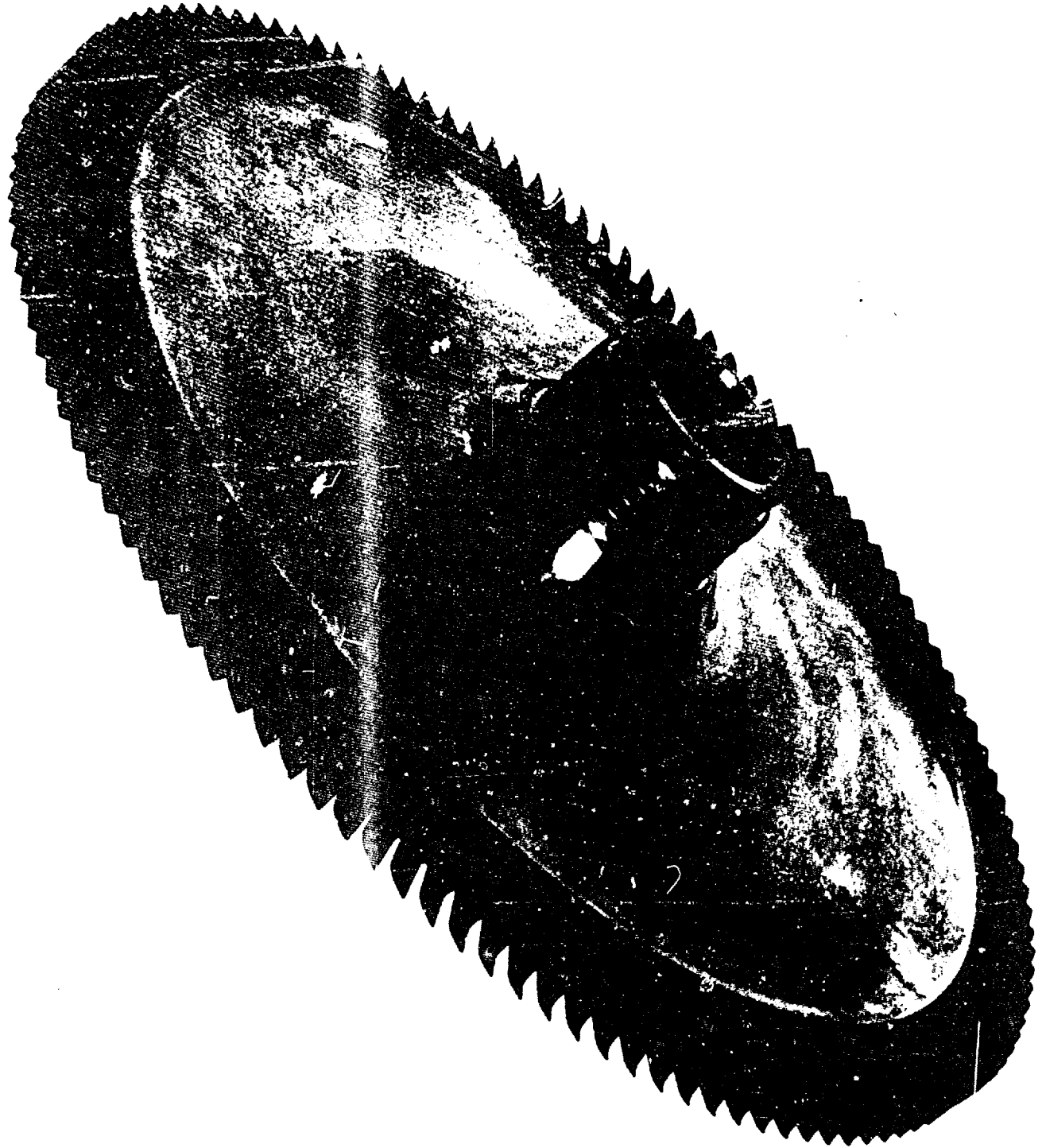
FIGURE 1. TURBINE WHEEL     A85918
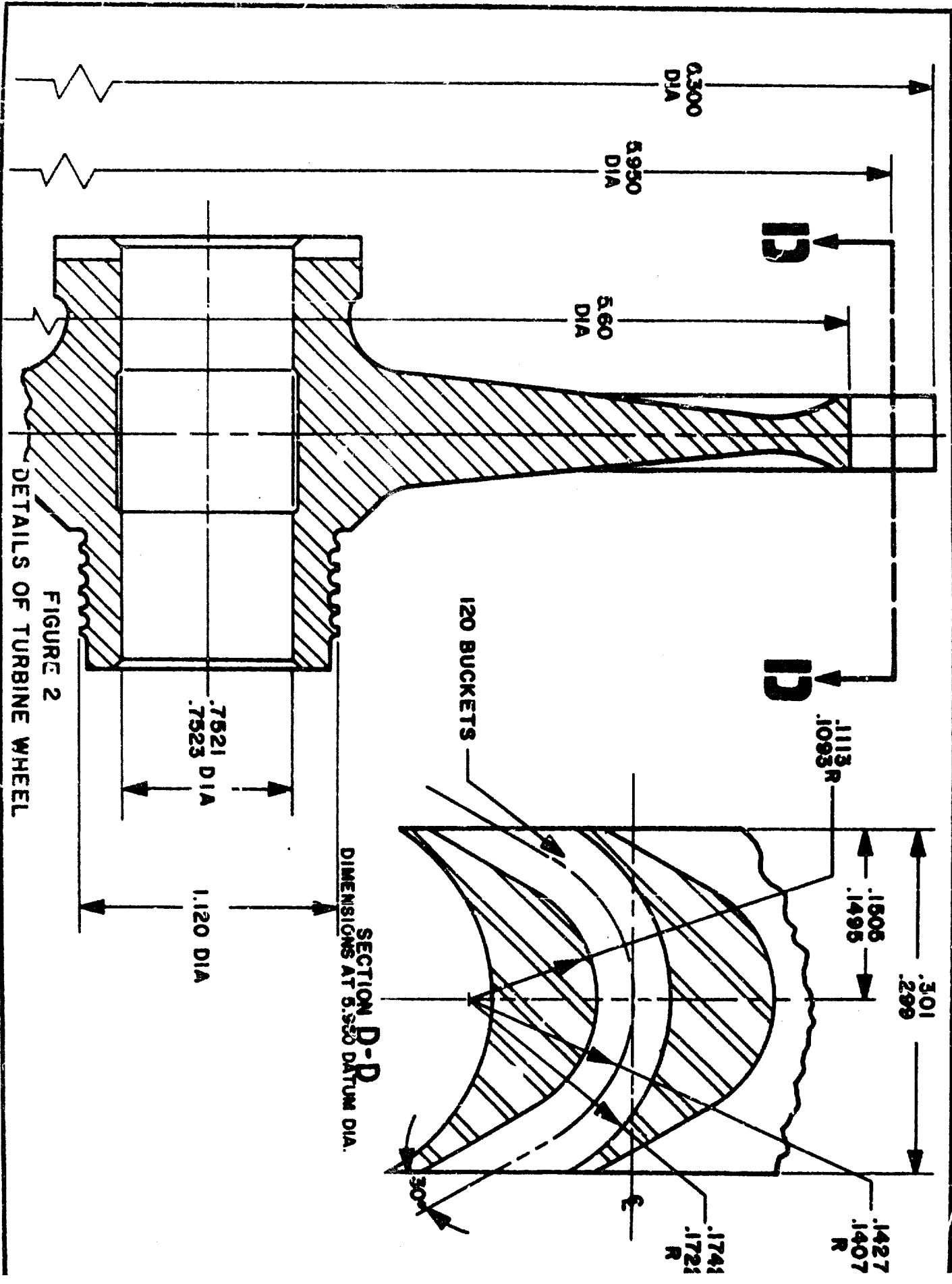
FIGURE 2
DETAILS OF TURBINE WHEEL

0.300 DIA
5.950 DIA
5.60 DIA
.7521 .7523 DIA
1.120 DIA
120 BUCKETS
SECTION D-D
DIMENSIONS AT 5.950 DATUM DIA.
.1113 .1093R
.1505 .1495
.501 .299
.1427 .1407 R
.1741 .1721 R
30°
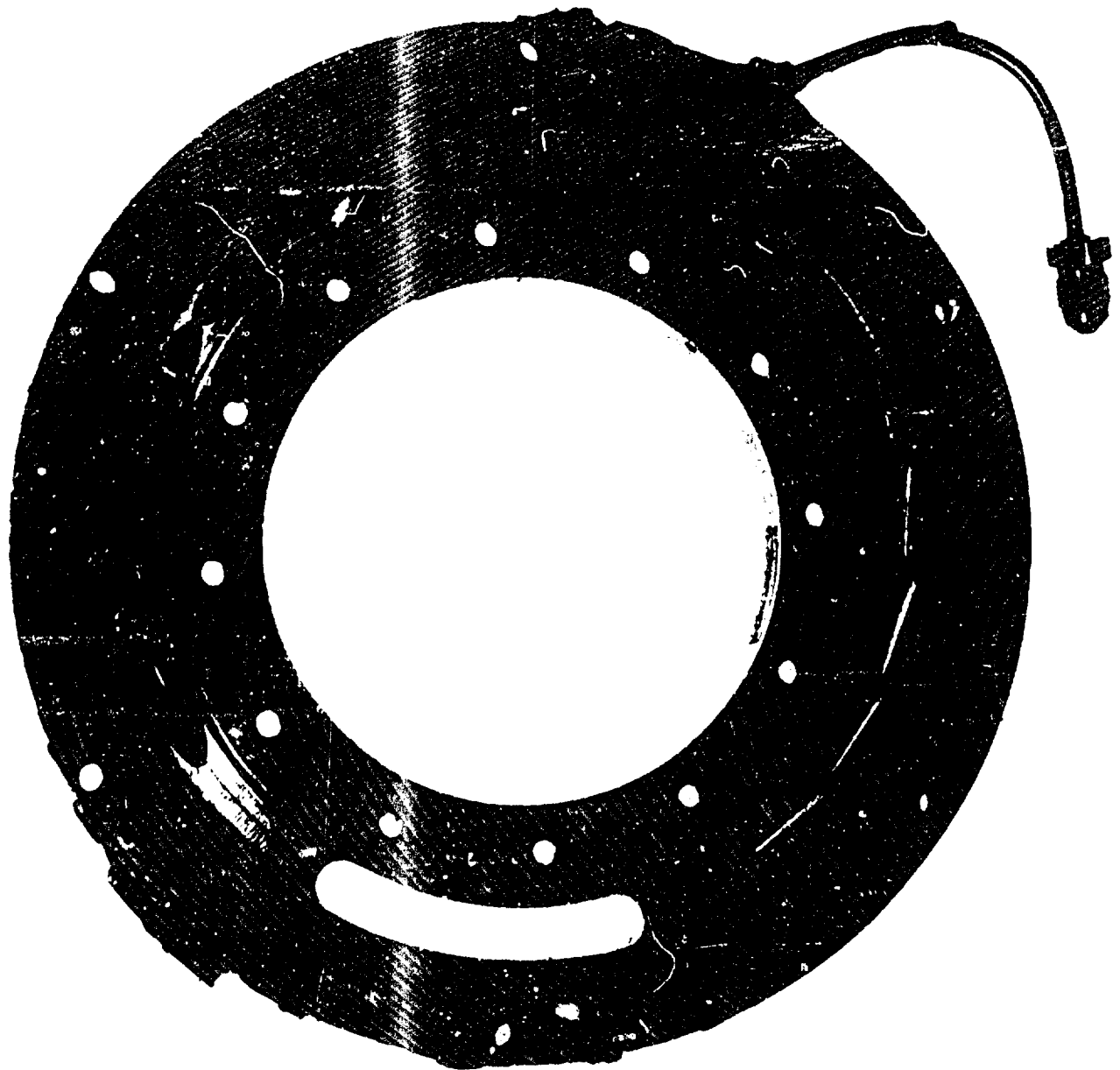
FIGURE 3. NOZZLE FOR RELATIVE MACH NUMBER 1.8      A65910

FIGURE 4. TYPICAL NOZZLE FOR RESEARCH TURBINE WITH RELATIVE MACH NO. 1.8

EFFECTIVE AREA RATIO = 4.45
FOR M = .96, EXIT MACH NO. = 2.6
TURBINE RELATIVE MACH NO. = 1.8
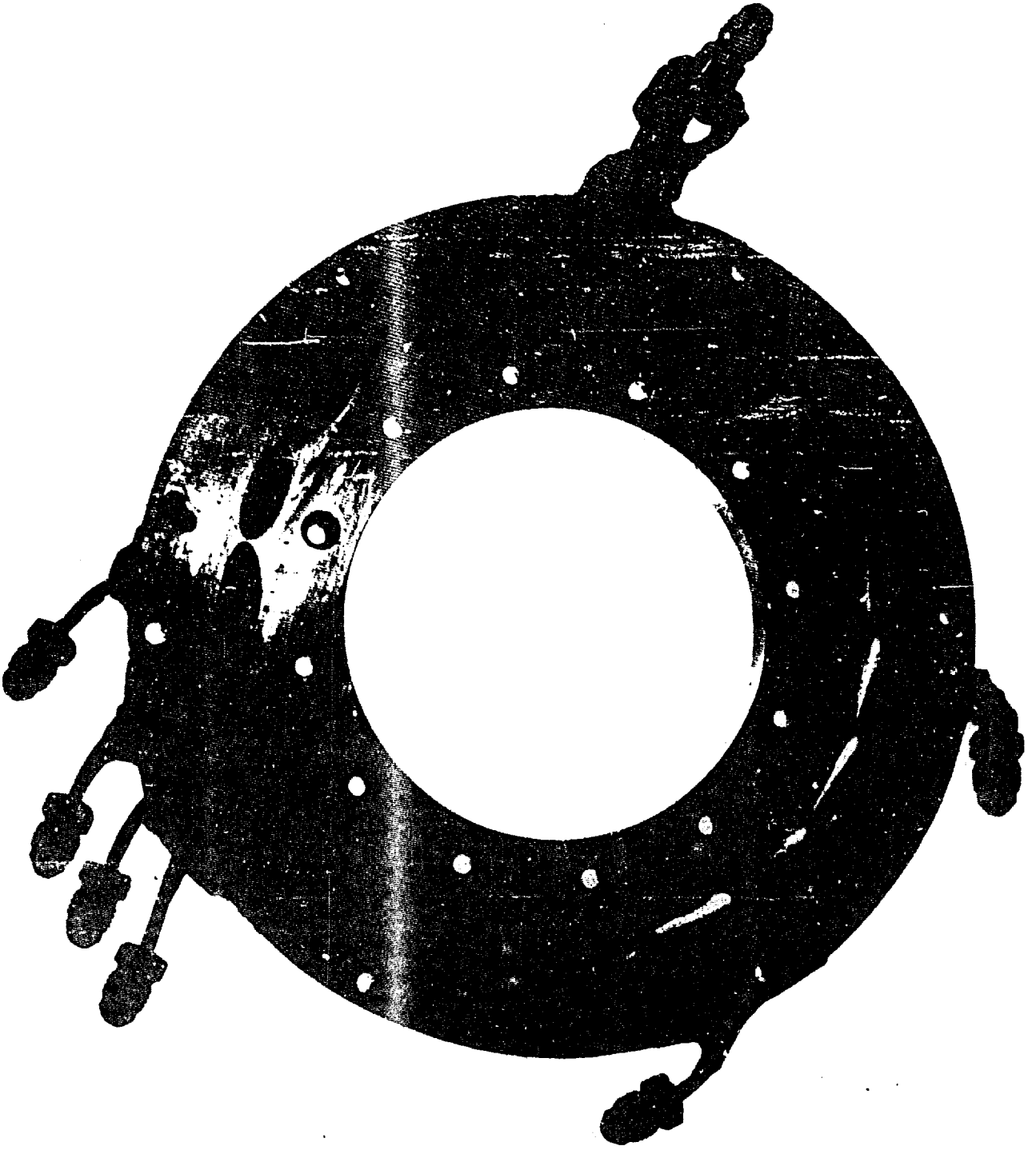
FIGURE 6. NOZZLE FOR RELATIVE MACH NUMBER 3.0    AG5897

FIGURE 5. FIRST TRANSONIC NOZZLE

AG5898

FIGURE 7. SECOND TRANSONIC NOZZLE
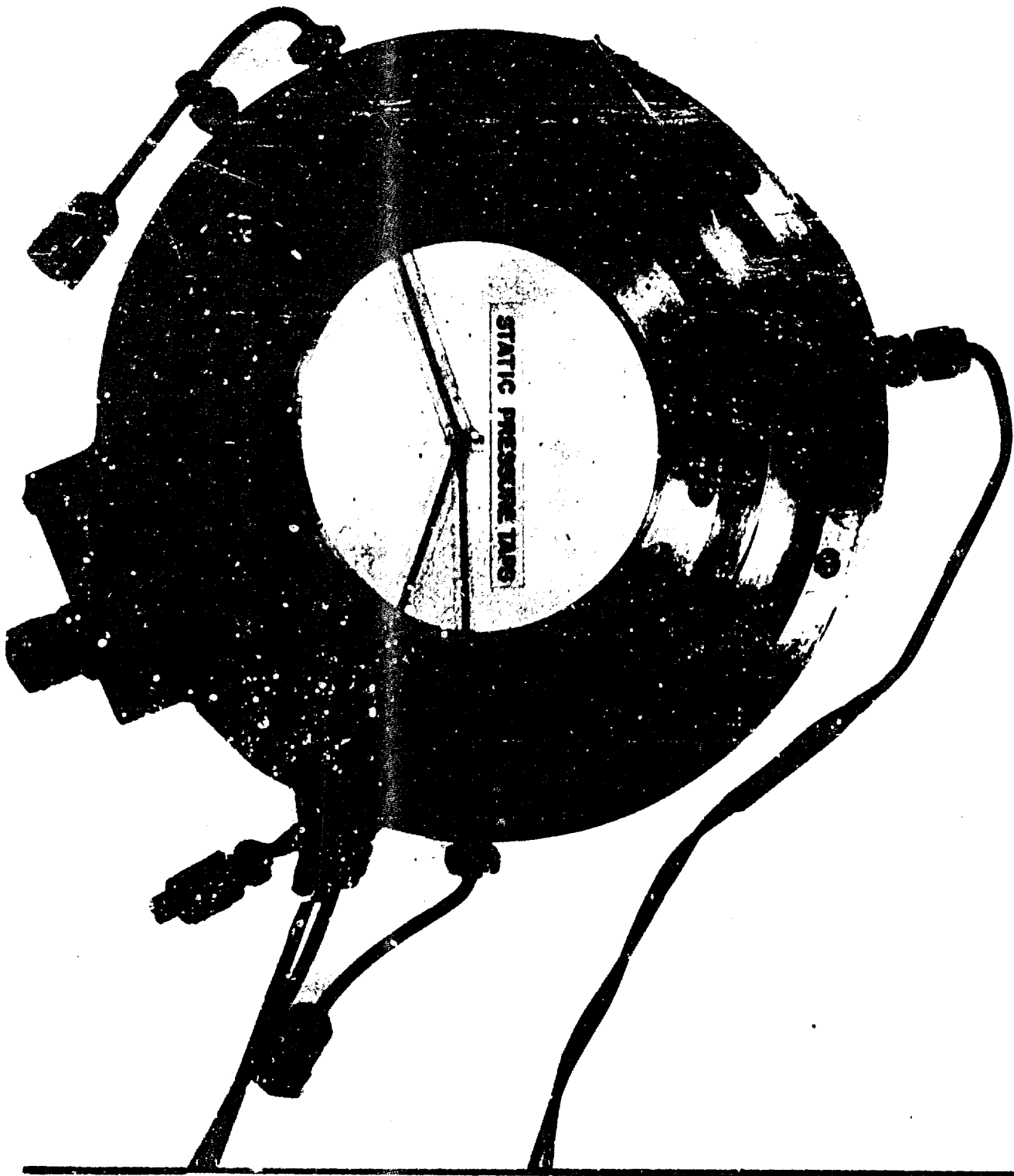
FIGURE 8. RE-ENTRY INTERSTAGE DUCT

STATIC PRESSURE TAP
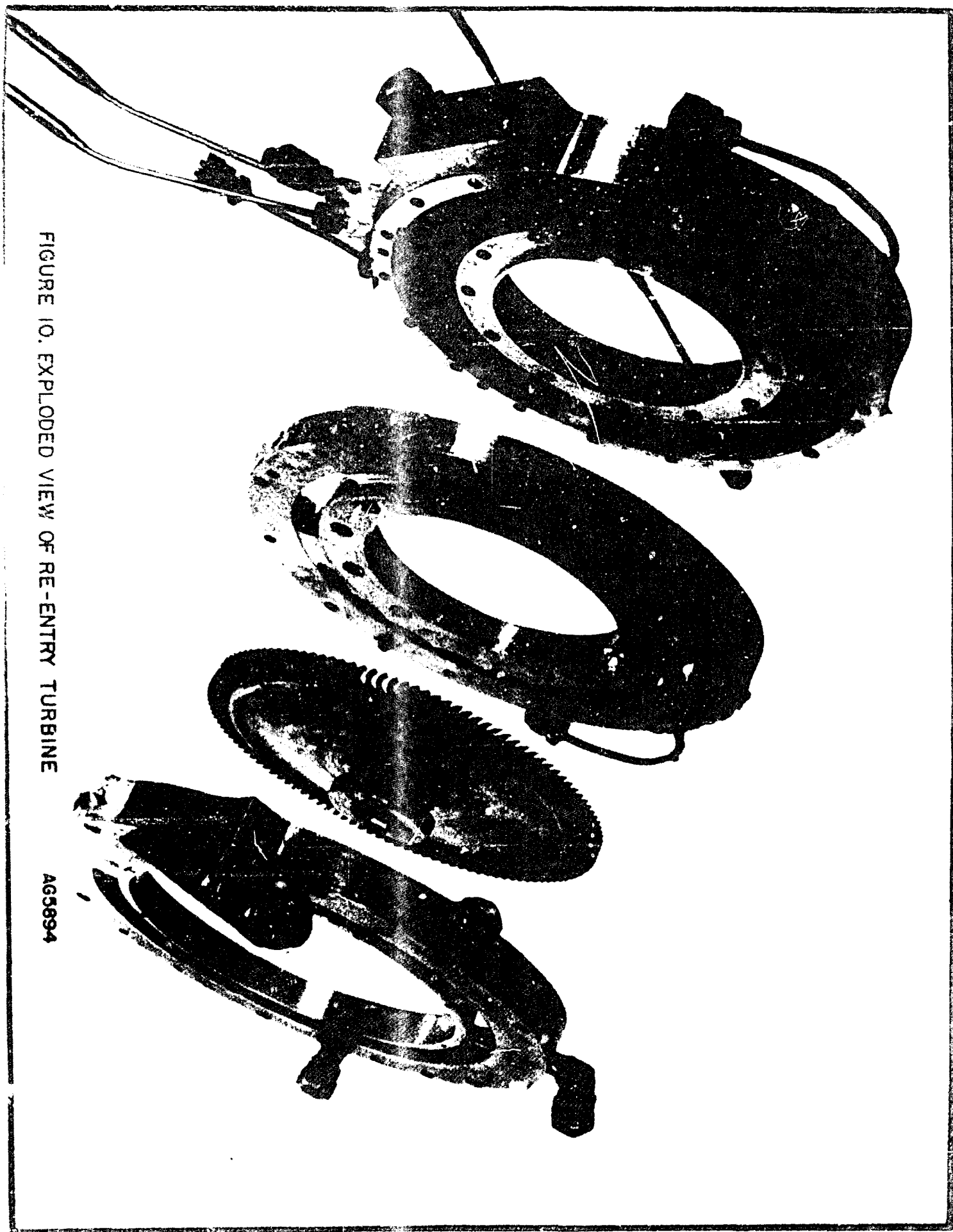
FIGURE 10. EXPLODED VIEW OF RE-ENTRY TURBINE

AG5894
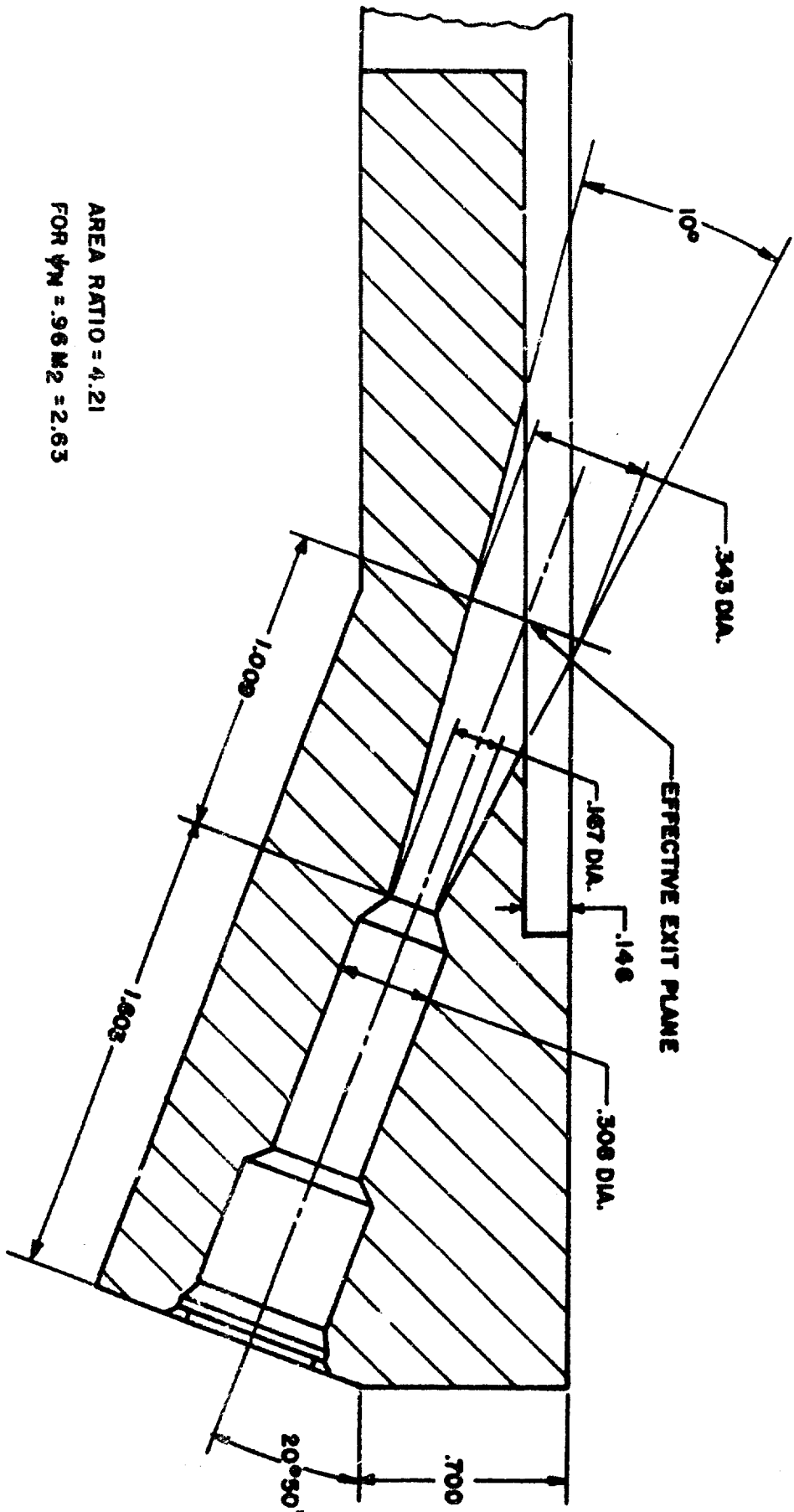
AREA RATIO = 4.21

FOR $\psi_N$ = .96 $M_2$ = 2.63

FIGURE 9. SECTION THROUGH FIRST STAGE NOZZLE—TWO STAGE RE-ENTRY TURB.

10°

.343 DIA.

.167 DIA.

EFFECTIVE EXIT PLANE

.146

.306 DIA.

1.009

1.303

20°30'

.700
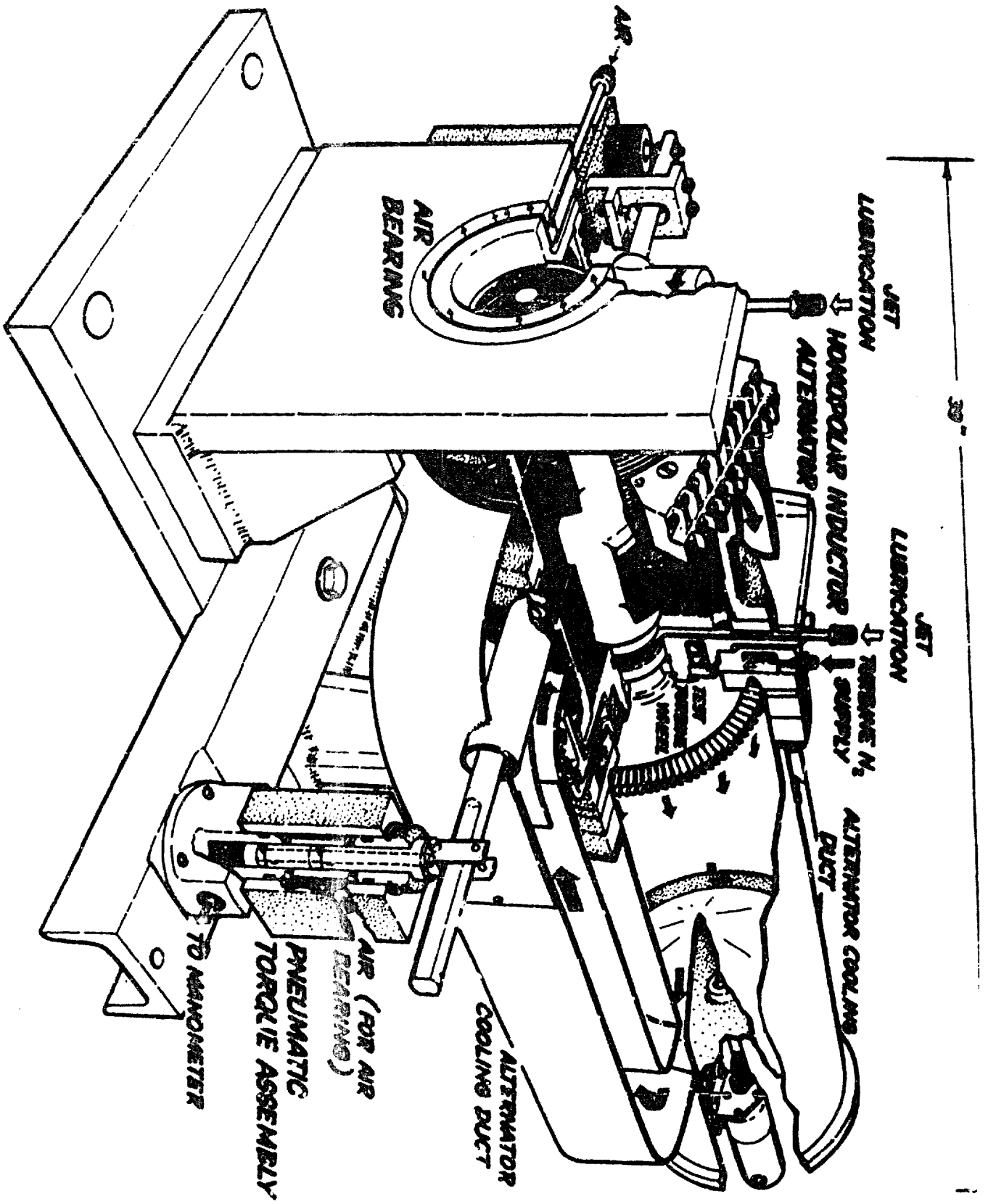
FIGURE II. SECTIONAL VIEW OF DYNAMOMETER
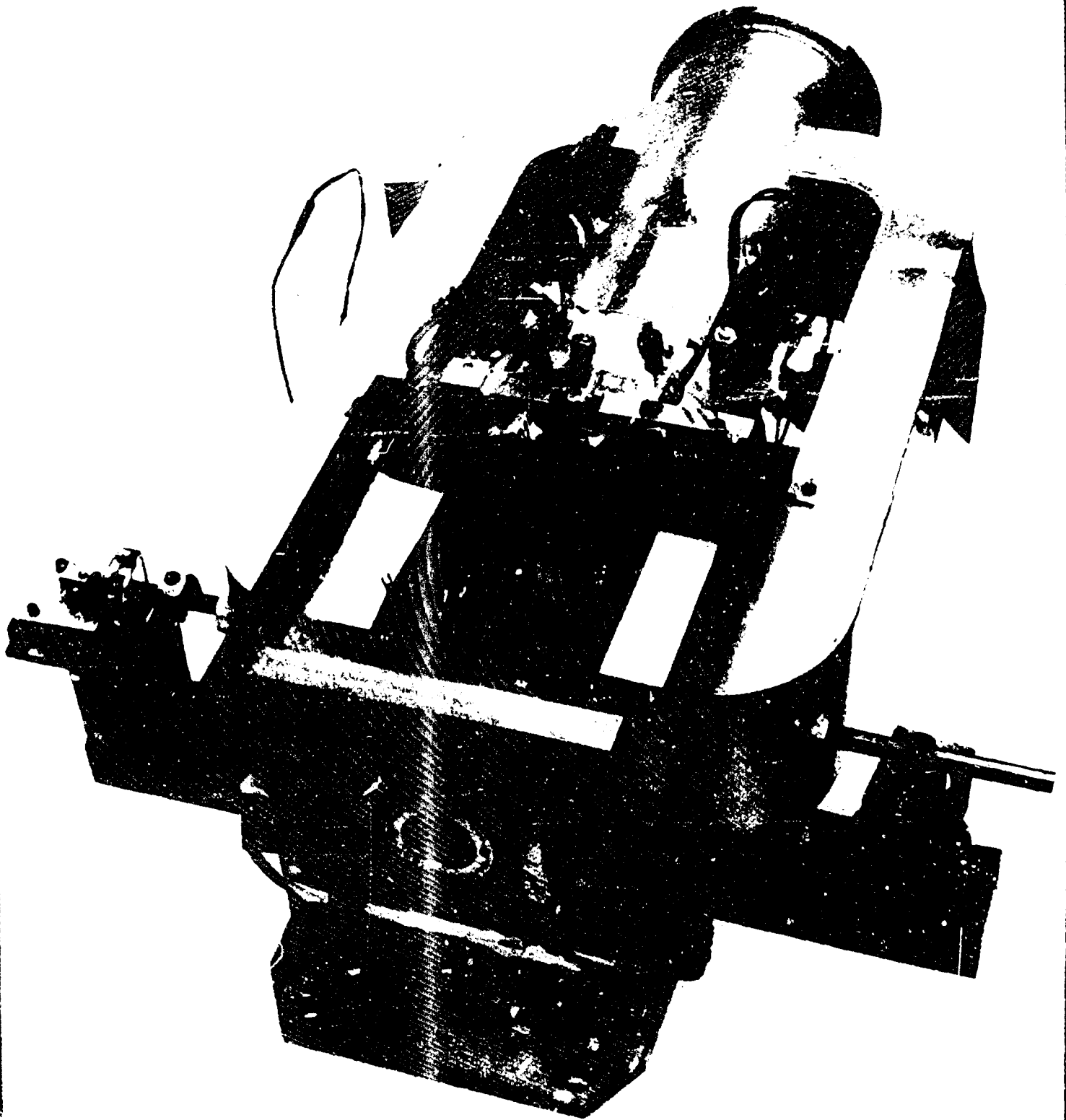
FIGURE 12. TURBINE DYNAMOMETER

AG 5896

STATIC PRESSURE TAPS
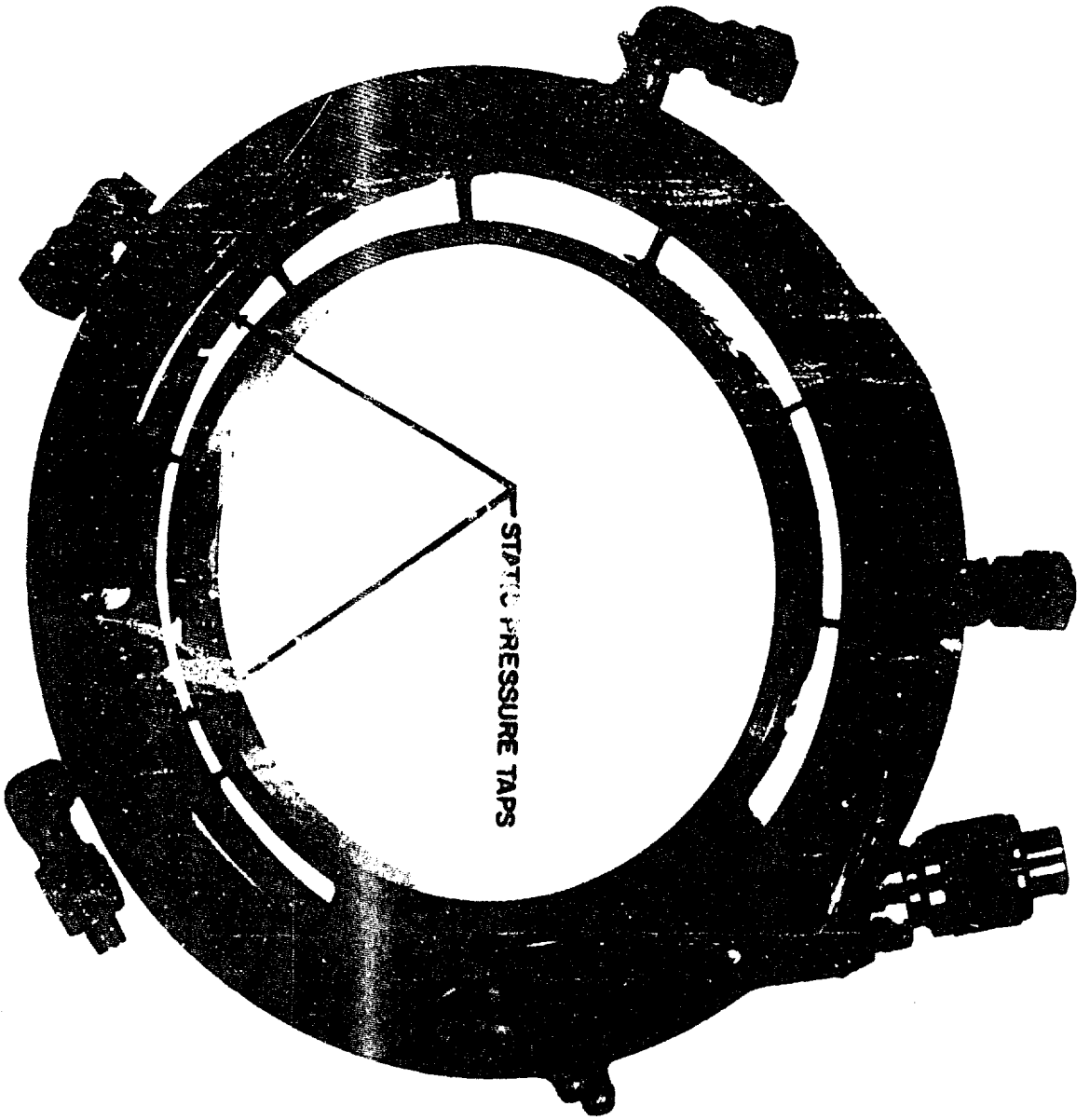
FIGURE 13(b). FIRST STAGE NOZZLE, SECOND STAGE EXHAUST
DUCT AND INSTRUMENTATION

AG 5901
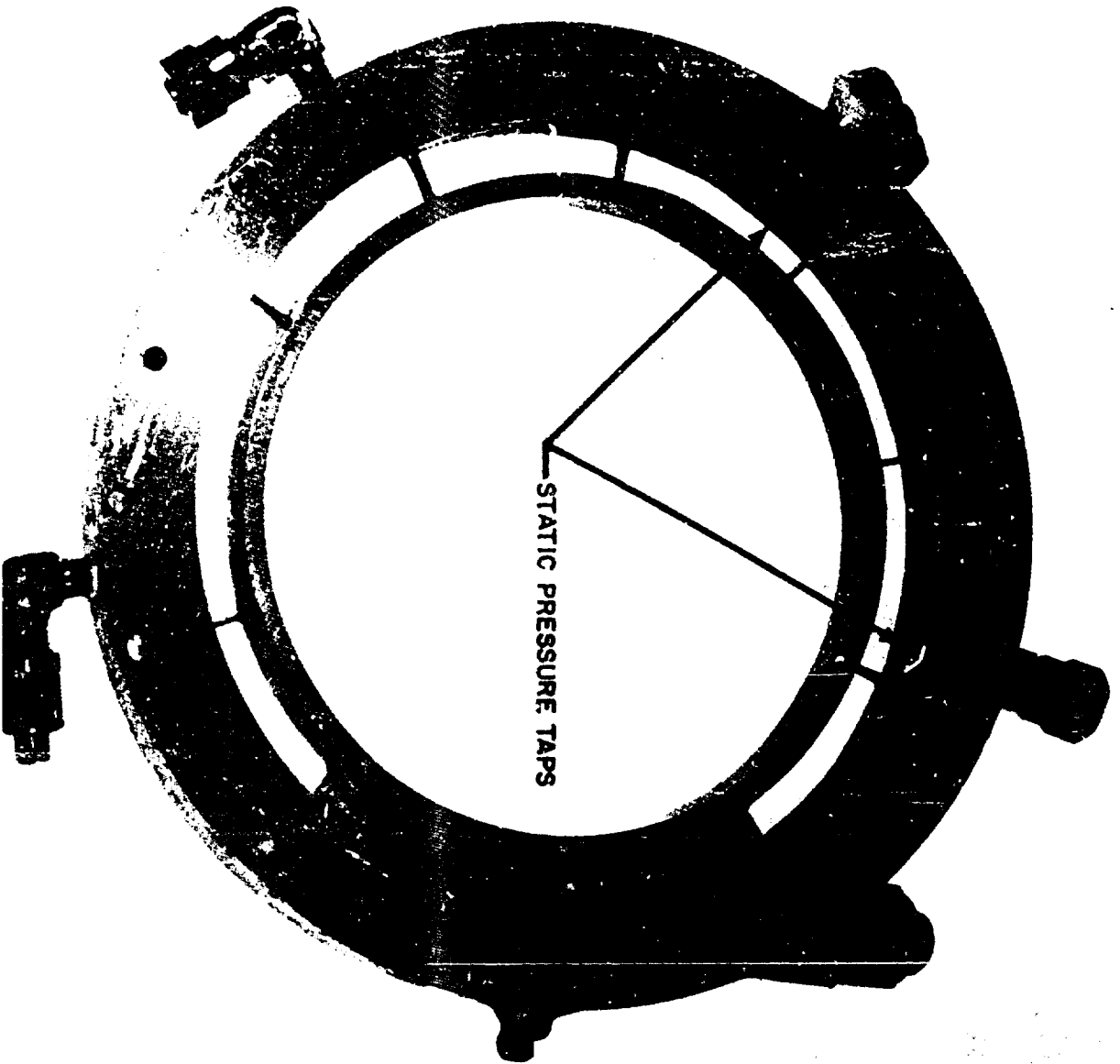
FIGURE 13(a). EXHAUST DUCT SHOWING INSTRUMENTATION    AG5904

STATIC PRESSURE TAPS
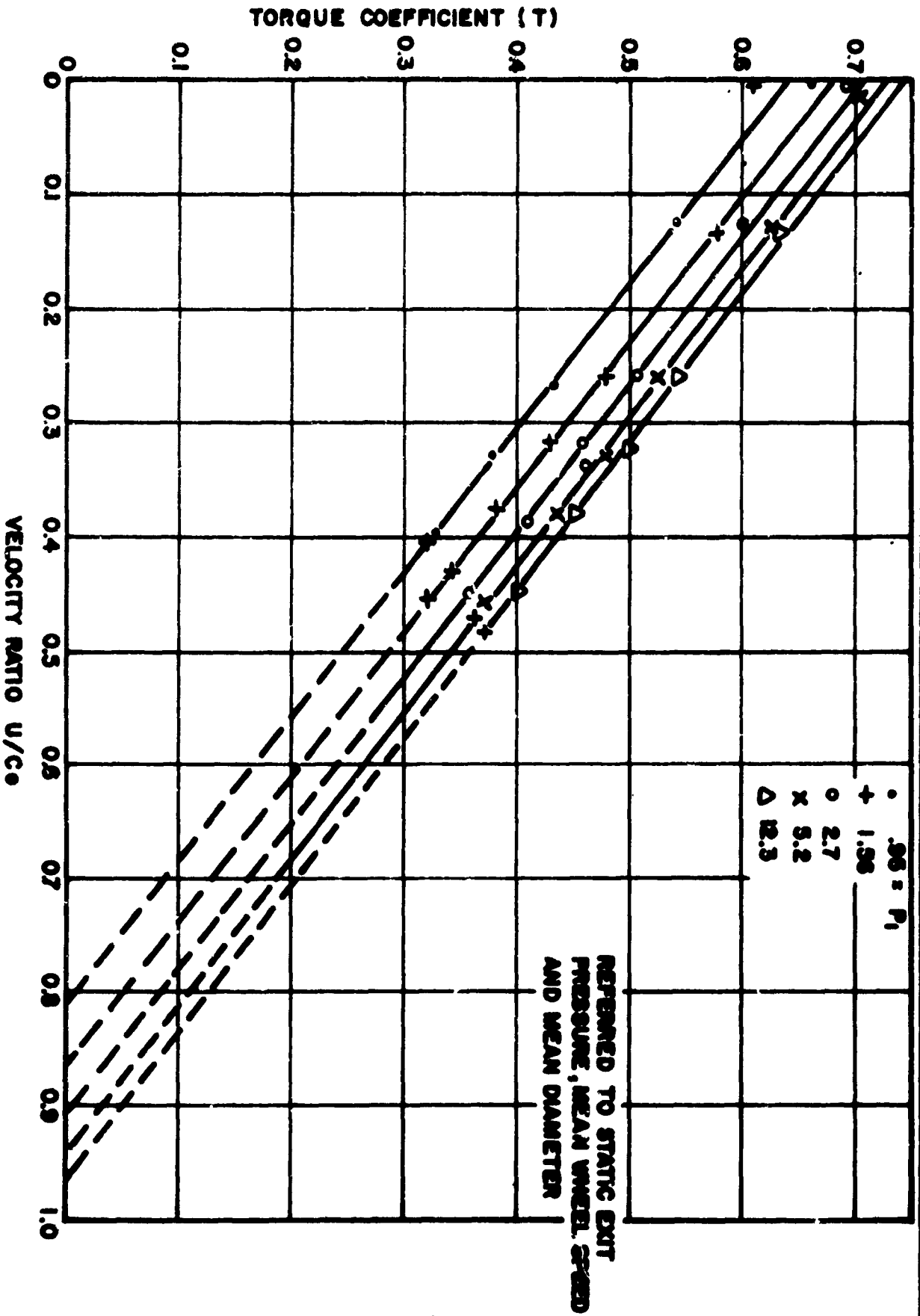
FIGURE 14. TEST DATA OF SUPERSONIC DESIGN (SINGLE STAGE)

AG 3954
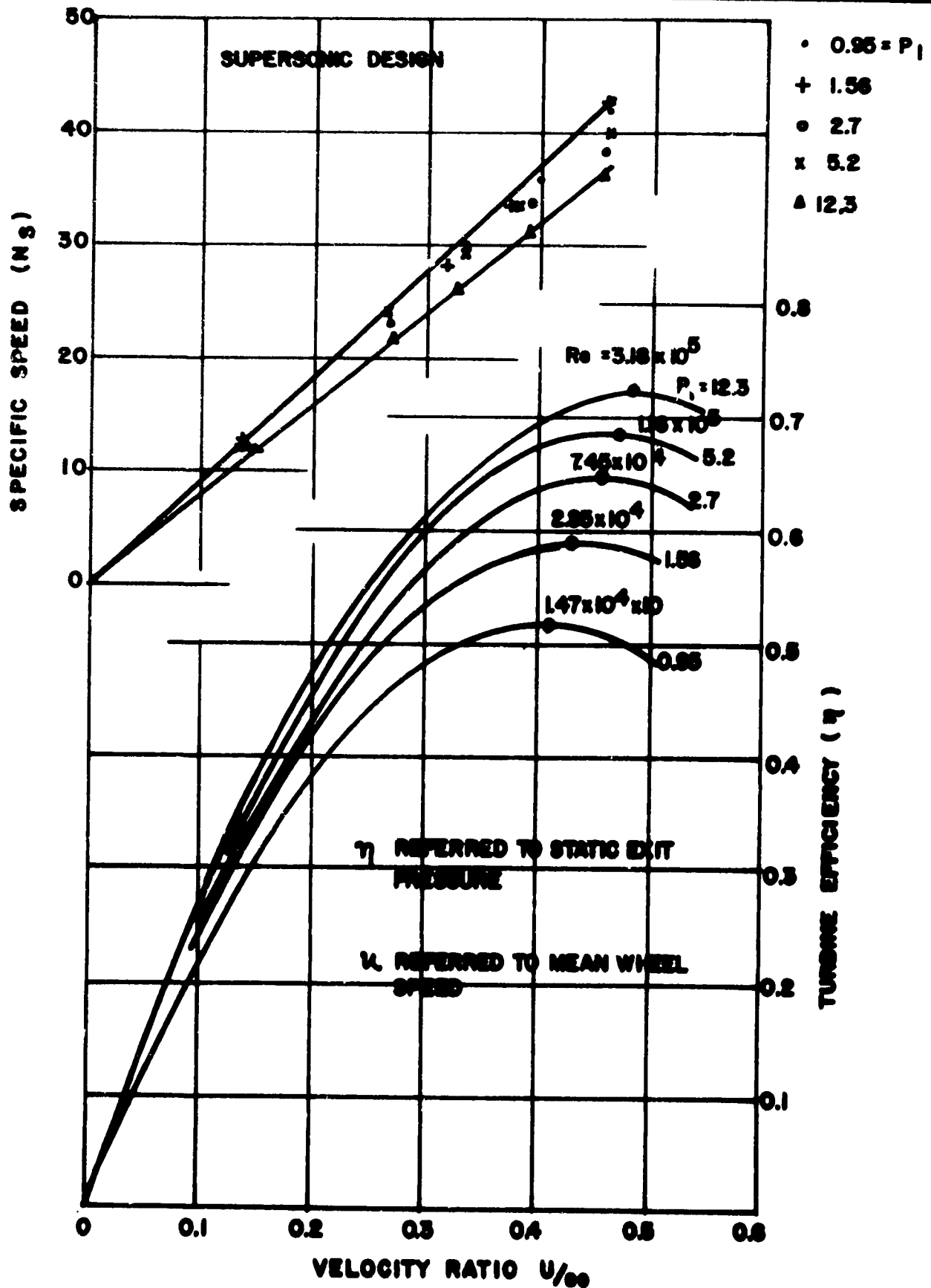
FIGURE 15. TEST DATA OF SUPERSONIC DESIGN (SINGLE STAGE)
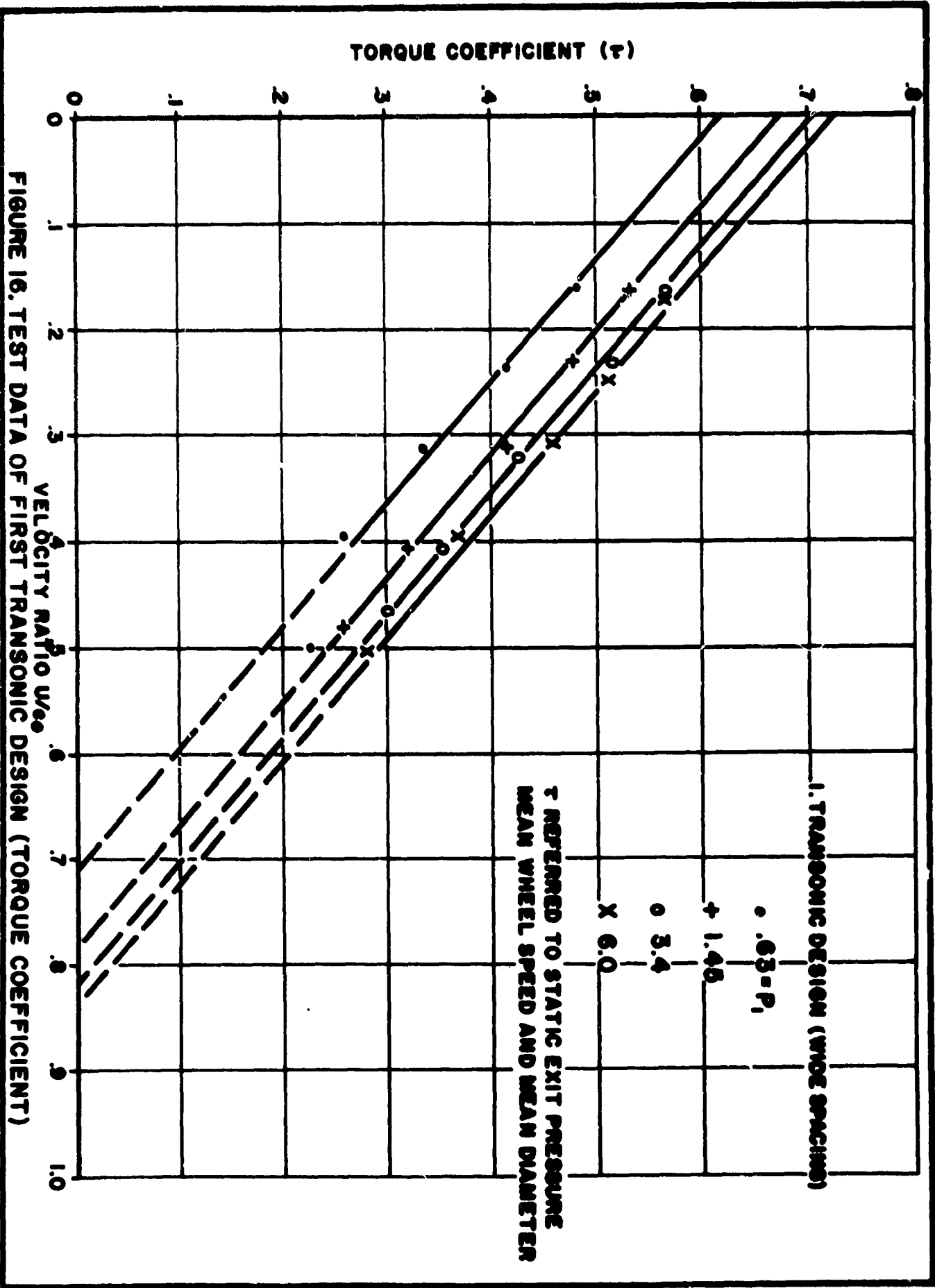
FIGURE 16. TEST DATA OF FIRST TRANSONIC DESIGN (TORQUE COEFFICIENT)

AG 5865
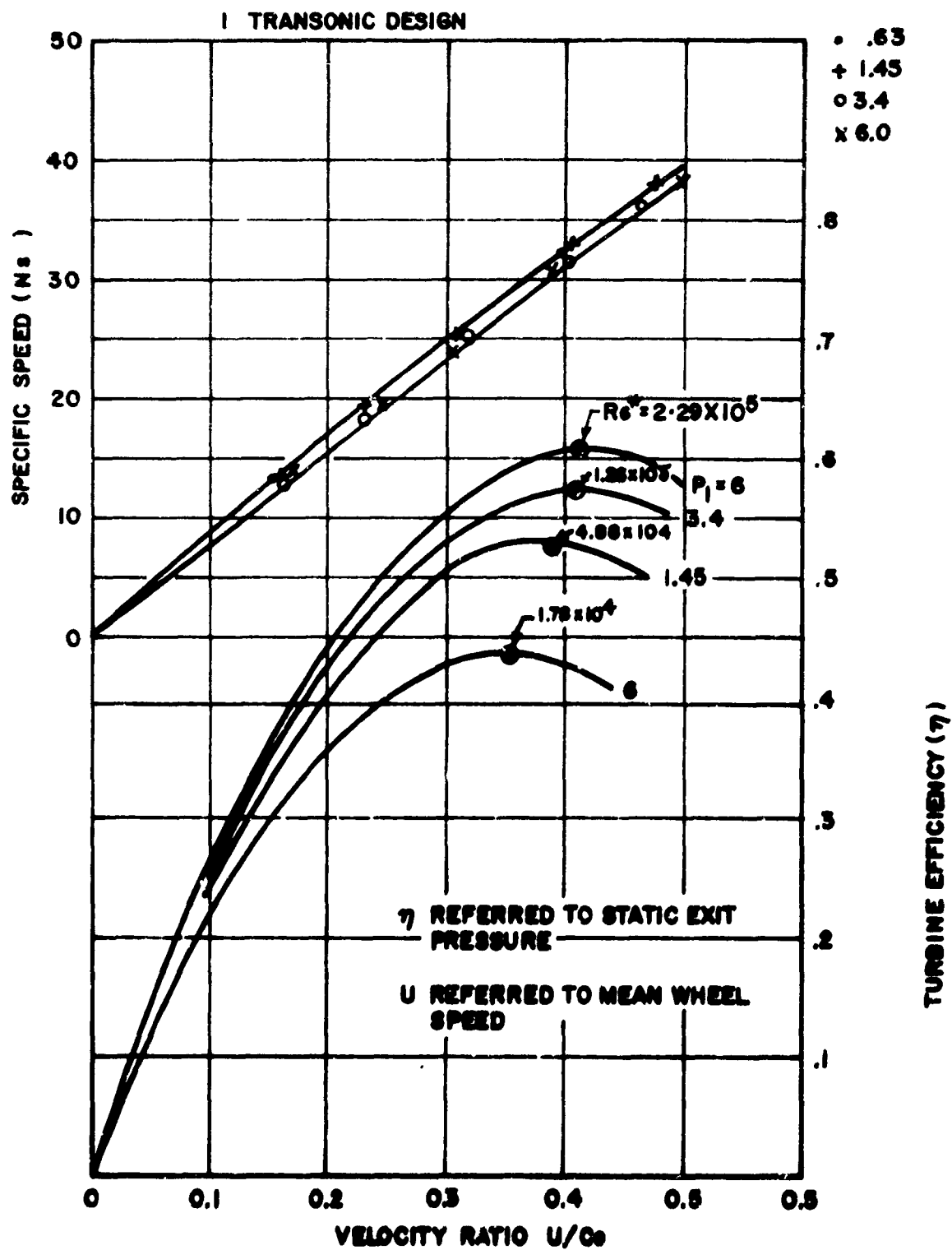
FIGURE 17. TEST DATA OF FIRST TRANSONIC DESIGN (EFFICIENCY)
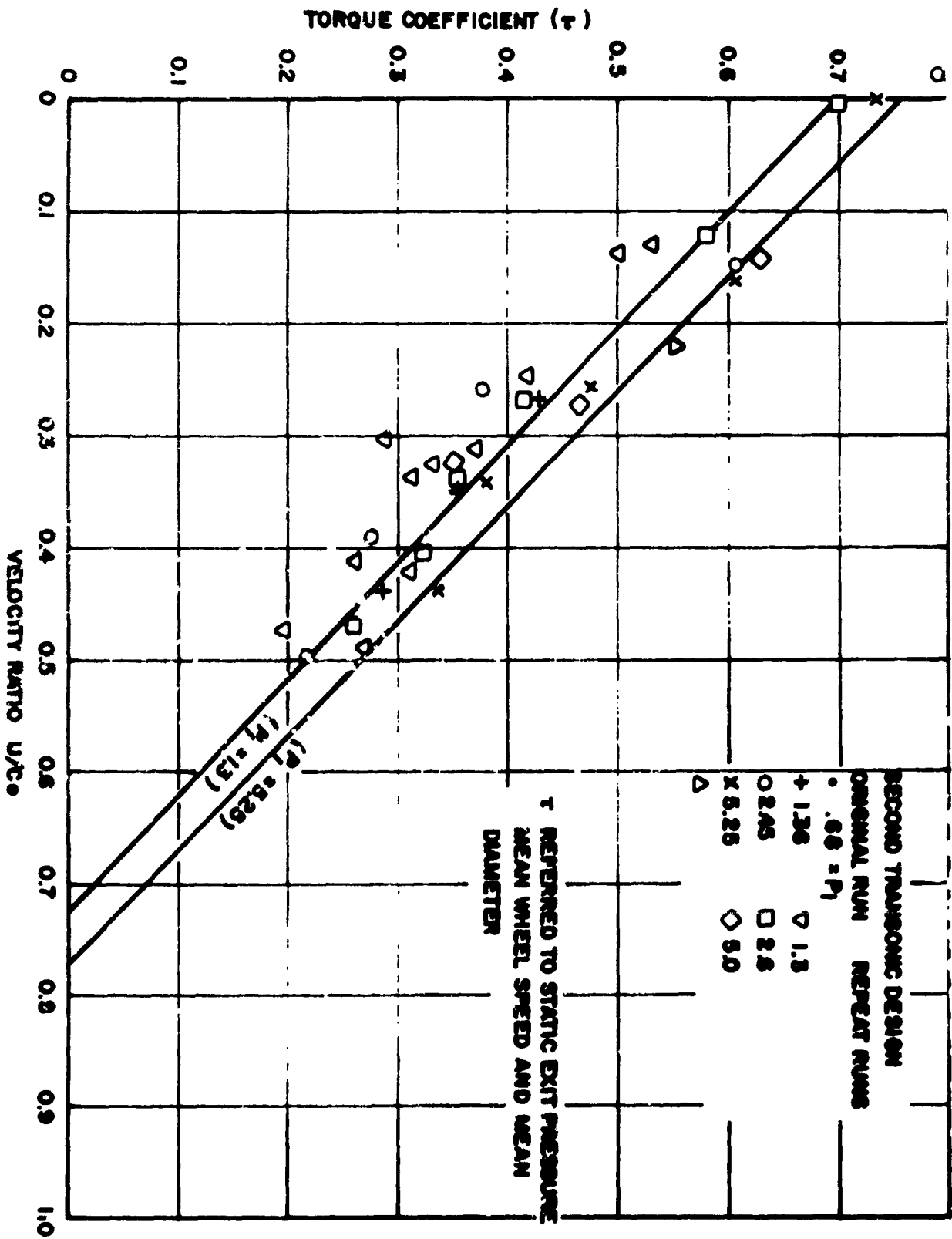
FIGURE 13. TEST DATA OF SECOND TRANSONIC DESIGN (TORQUE COEFFICIENT)
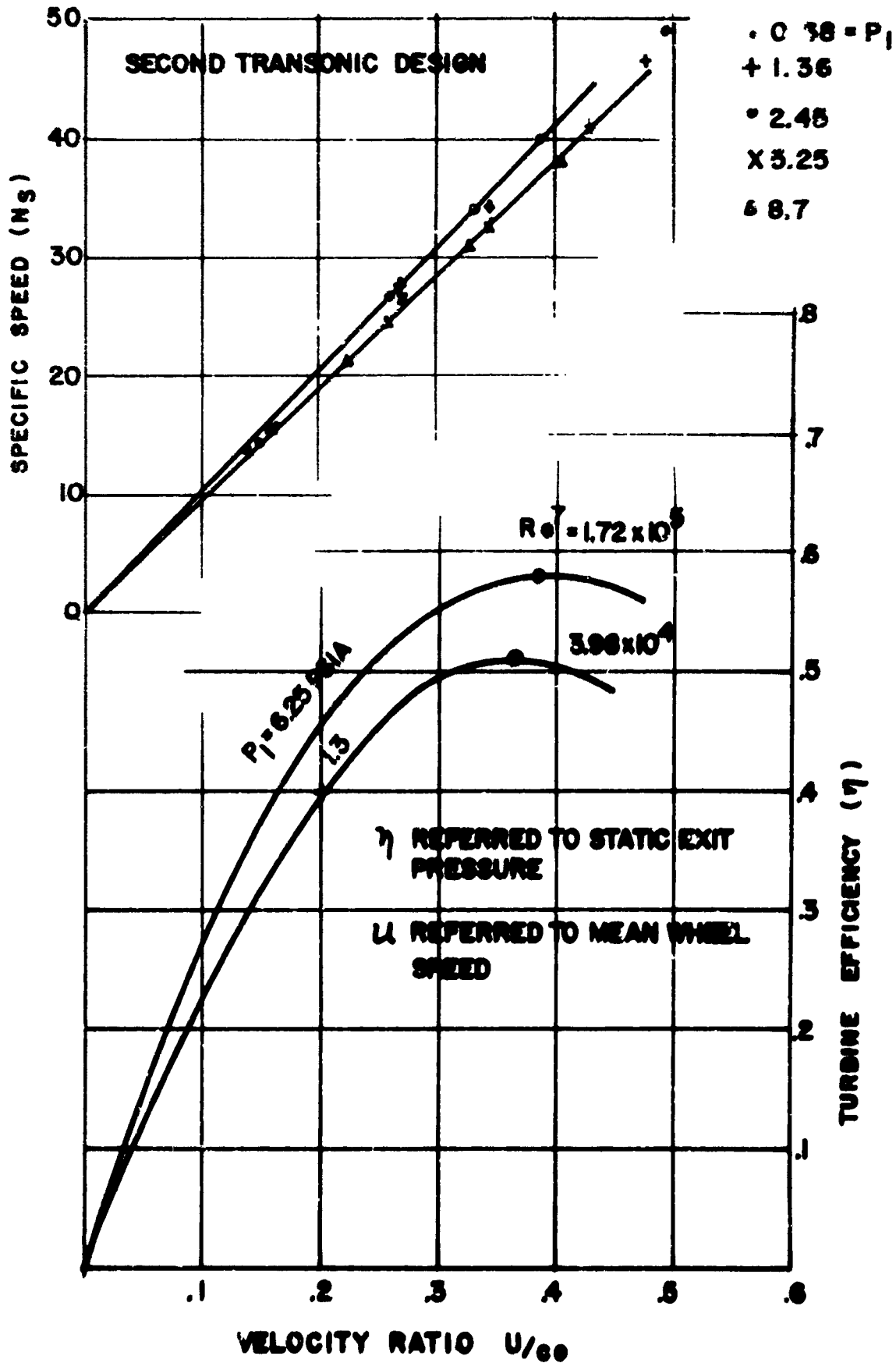
FIGURE 19. TEST DATA OF SECOND TRANSONIC DESIGN (EFFICIENCY)

TORQUE COEFFICIENT (τ)
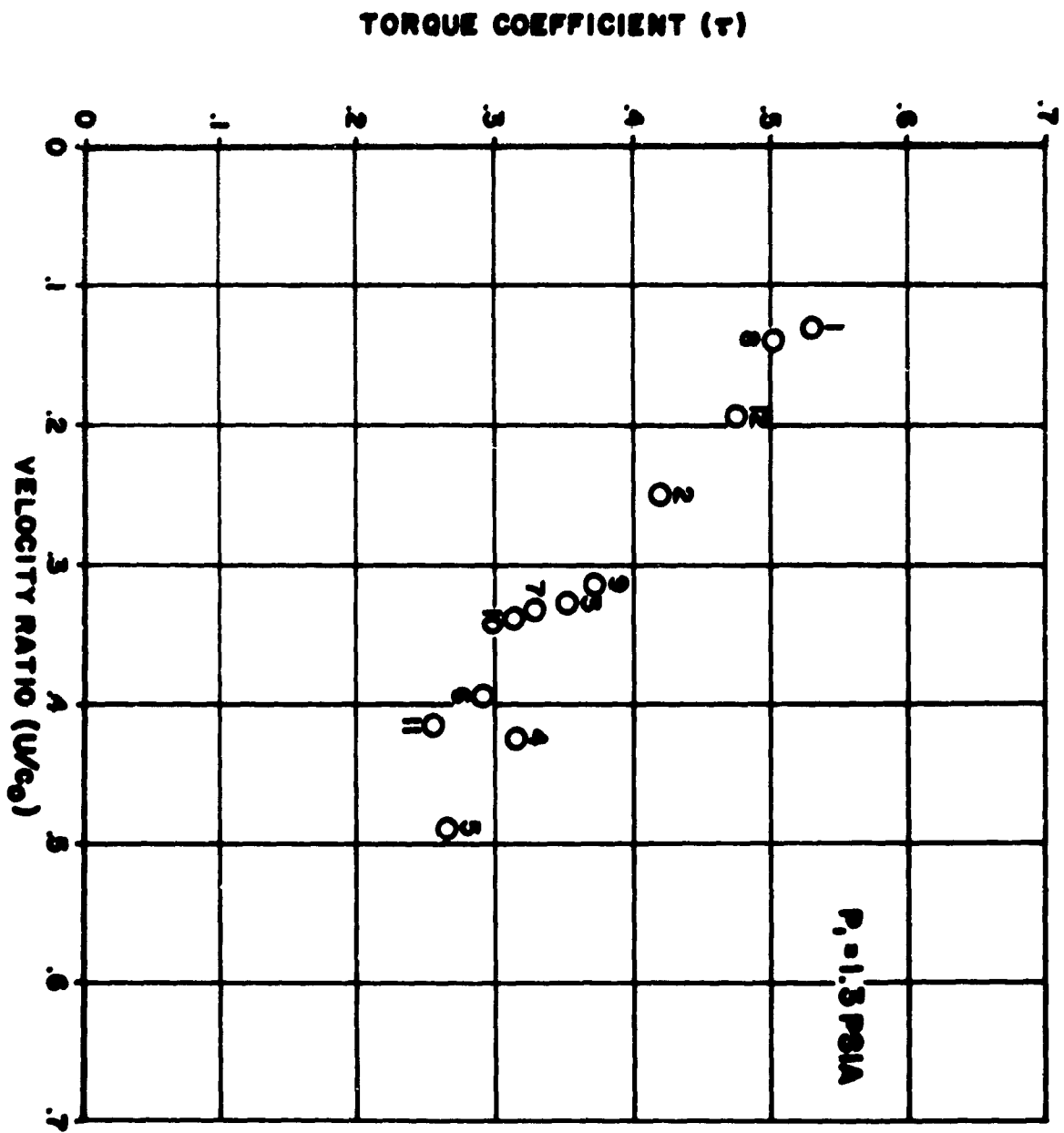
FIGURE 20. RERUN TEST DATA OF SECOND TRANSONIC DESIGN

VELOCITY RATIO (U/C₀)

P₁ = 1.3 PSIA
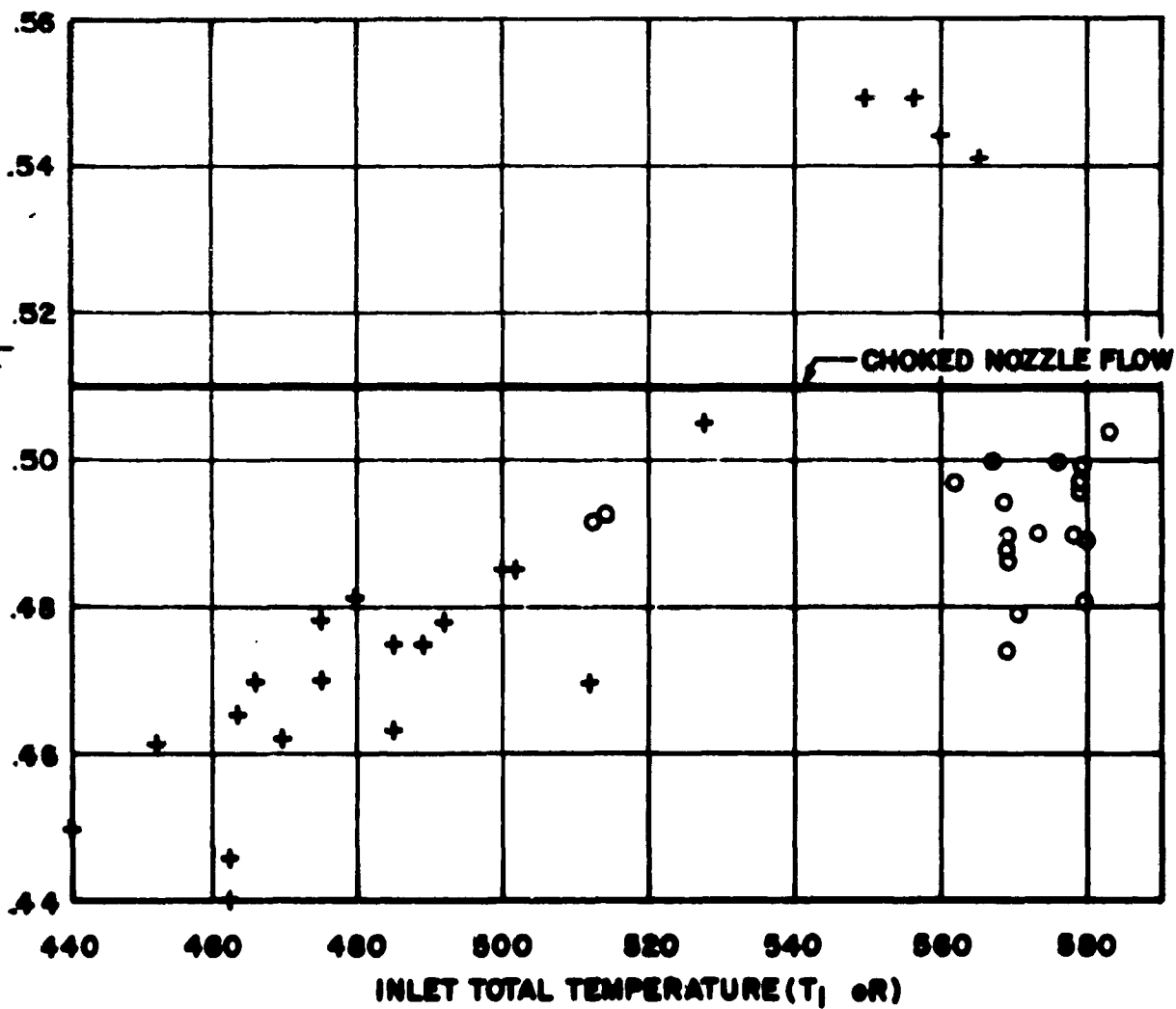
FIGURE 21. WEIGHT FLOW DATA OF SECOND TRANSONIC DESIGN
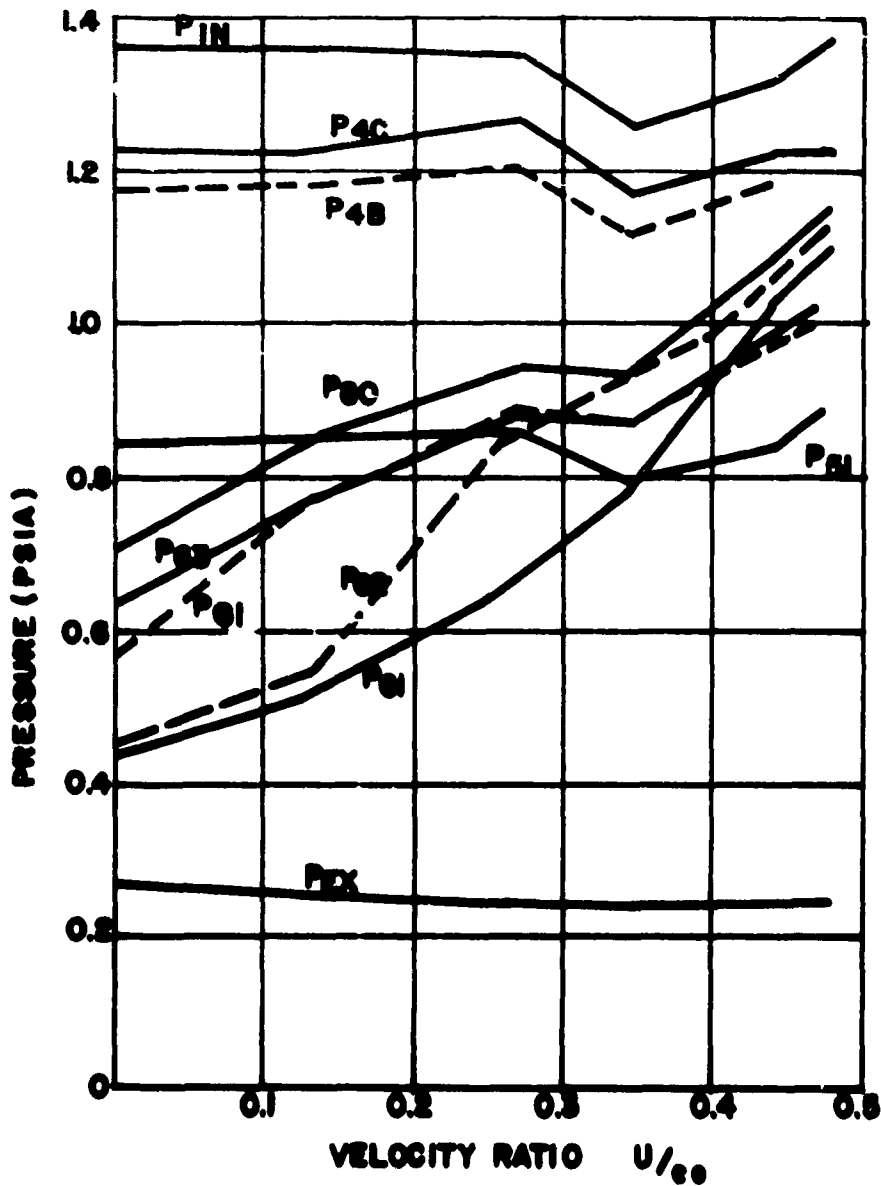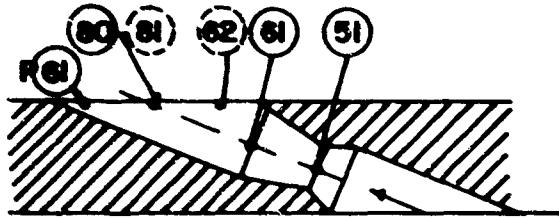
FIGURE 22. PRESSURE READING FOR SECOND TRANSONIC DESIGN $P_{IN}$ = 1.36

PRESSURE TAP NUMBER
CODE PER FIGURE 21.
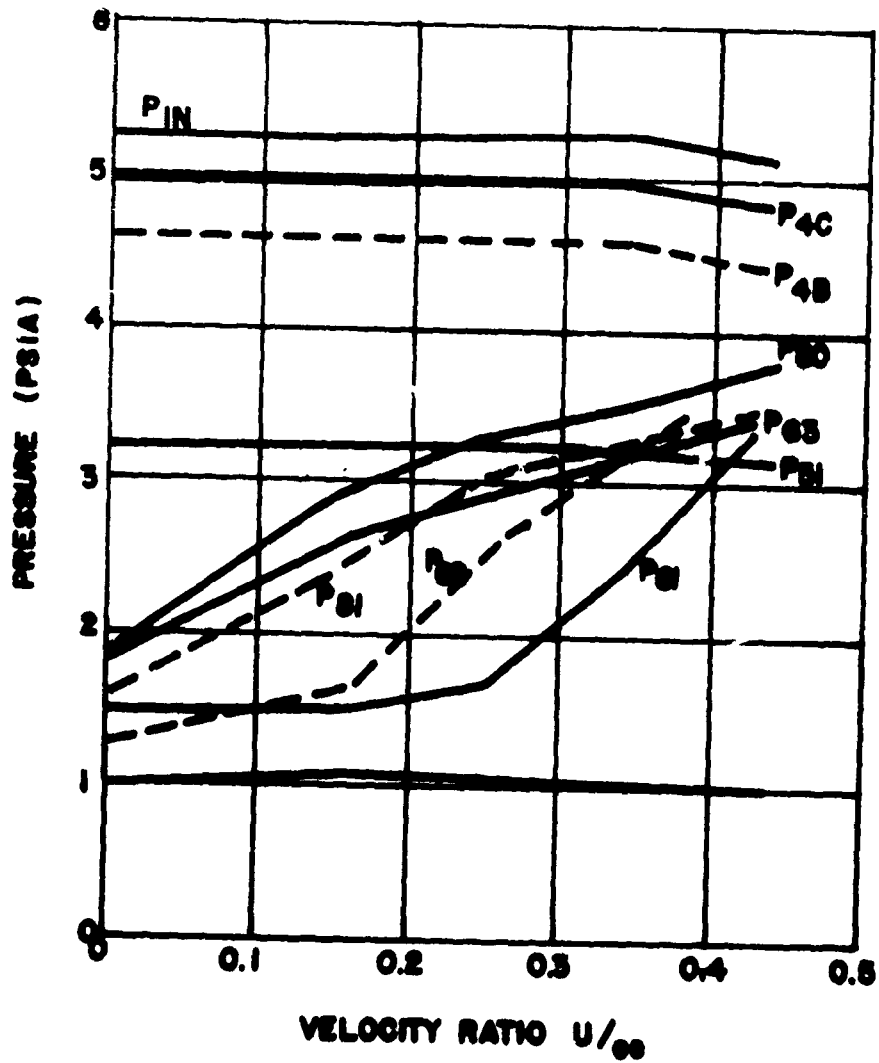
FIGURE 23. PRESSURE READINGS FOR SECOND TRANSONIC DESIGN $P_{IN}$ = 5.25 PSIA
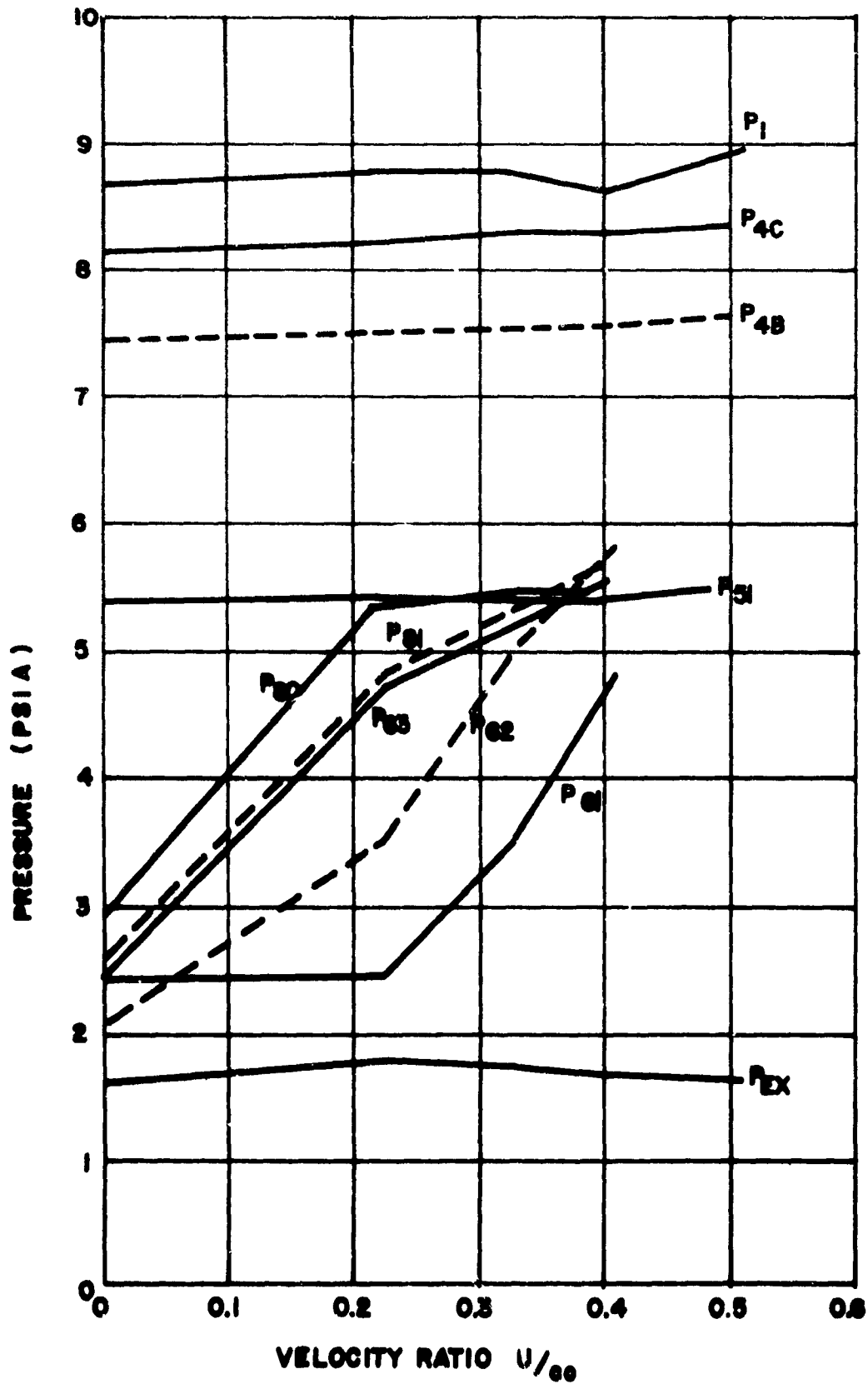
FIGURE 24. PRESSURE READING FOR SECOND TRANSONIC DESIGN    $P_{IN}$ = 9.3 PSI
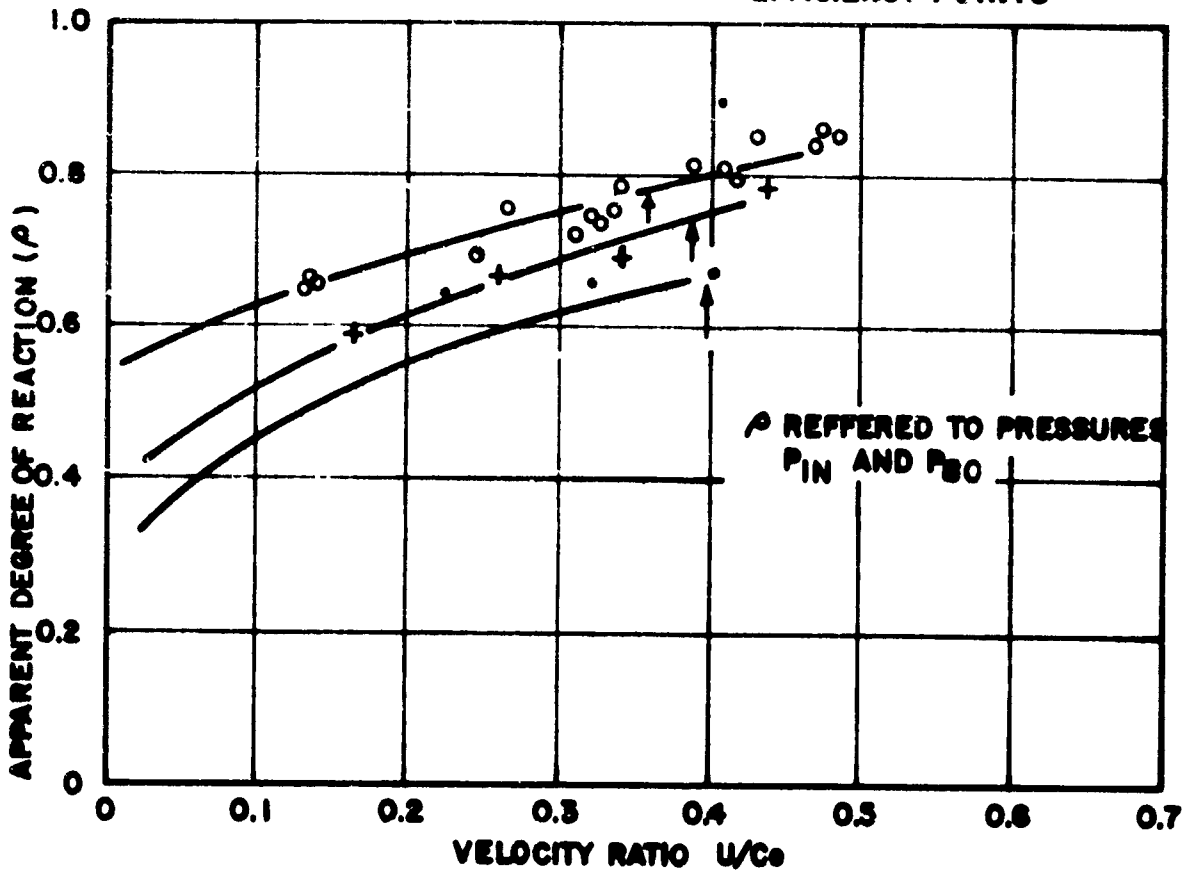
FIGURE 25. MEASURED DEGREE OF REACTION FOR SECOND TRANSONIC DESIGN
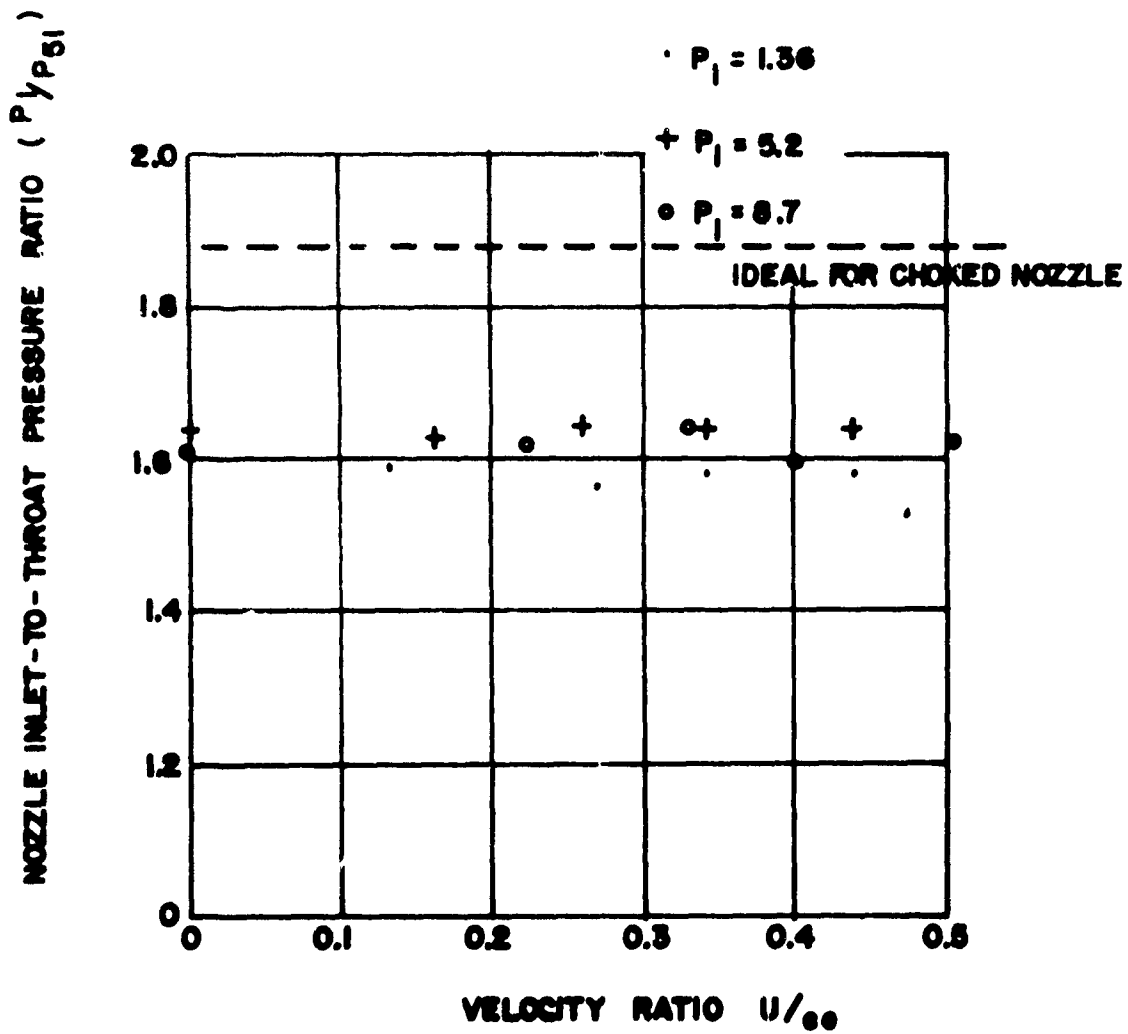
FIGURE 26. NOZZLE PRESSURE RATIOS FOR SECOND TRANSONIC DE
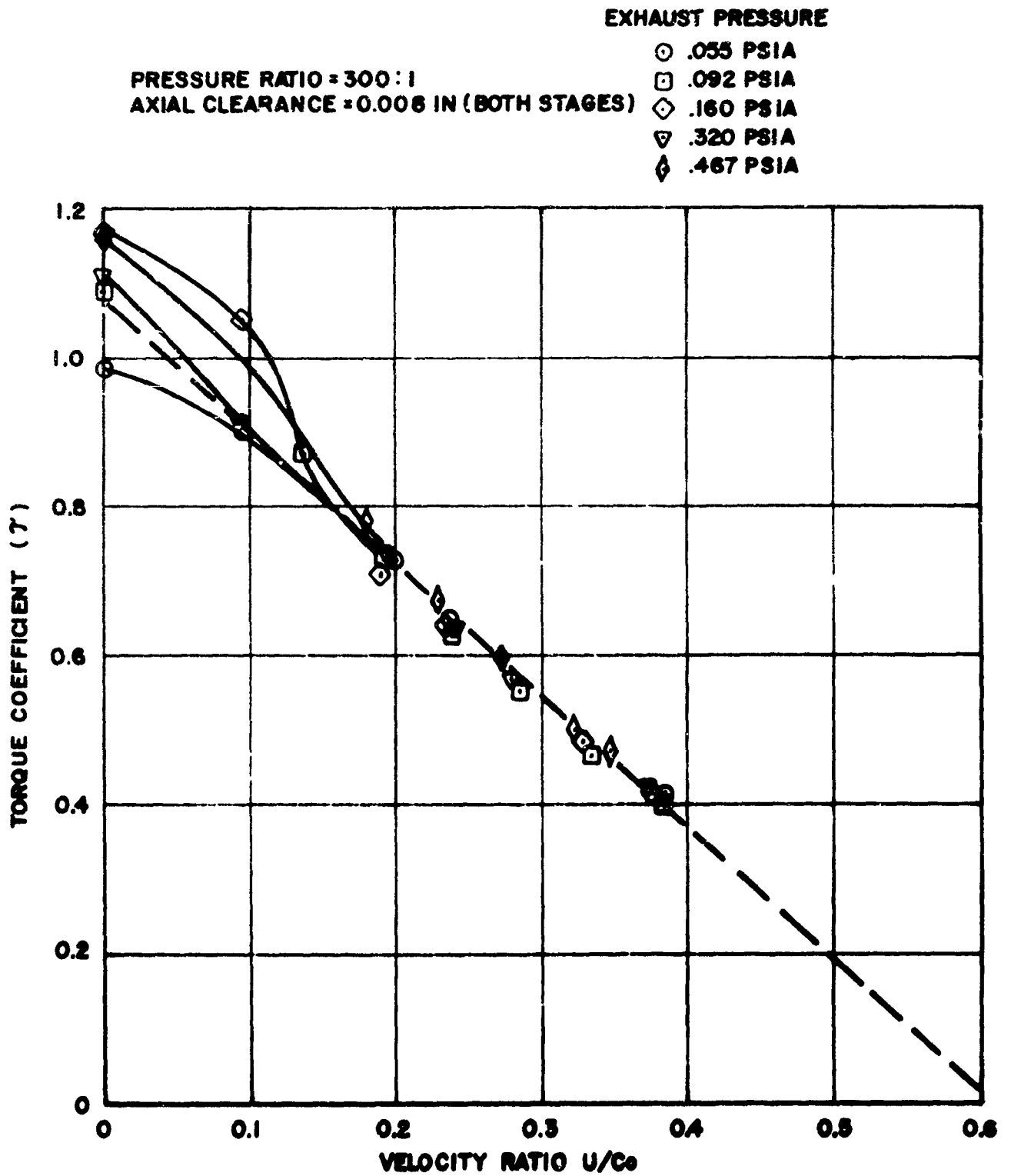
FIGURE 27. TEST DATA OF RE-ENTRY TURBINE (TORQUE COEFFICIENT)
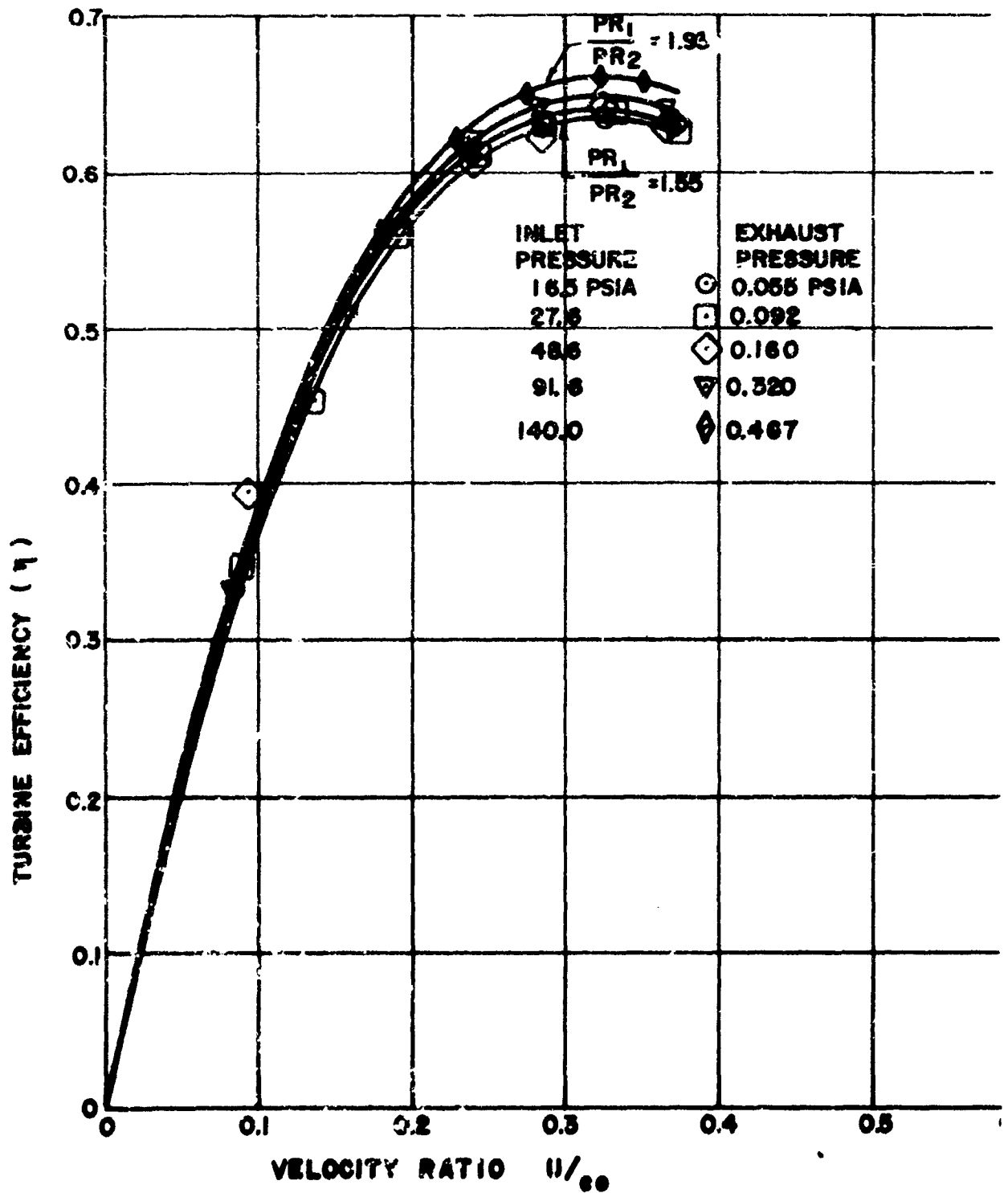
FIGURE 28. TEST DATA OF RE-ENTRY TURBINE (EFFICIENCY)
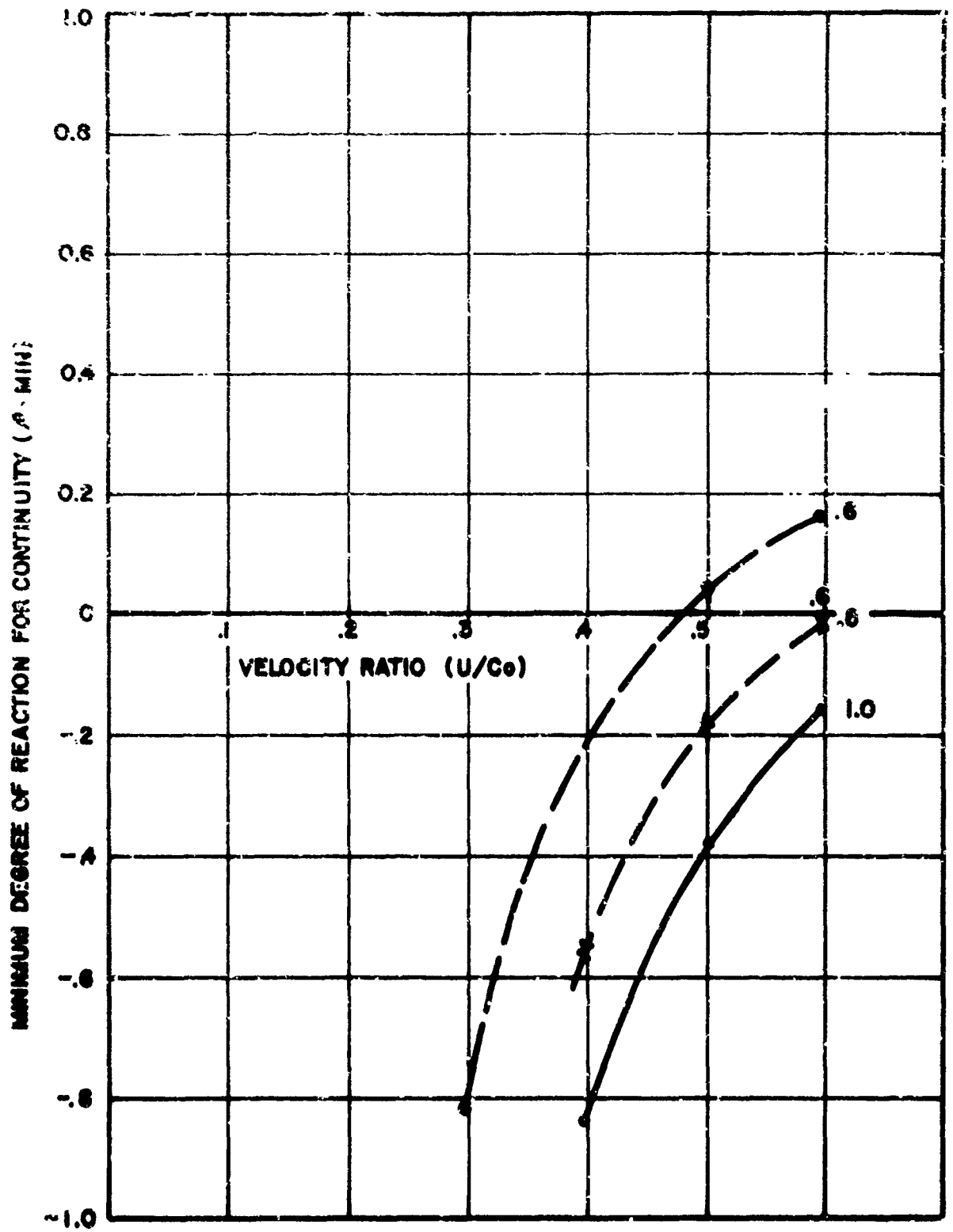
FIGURE 29. MINIMUM REQUIRED DEGREE OF REACTION FOR SUPER SONEC TURBI
(SINGLE STAGE)
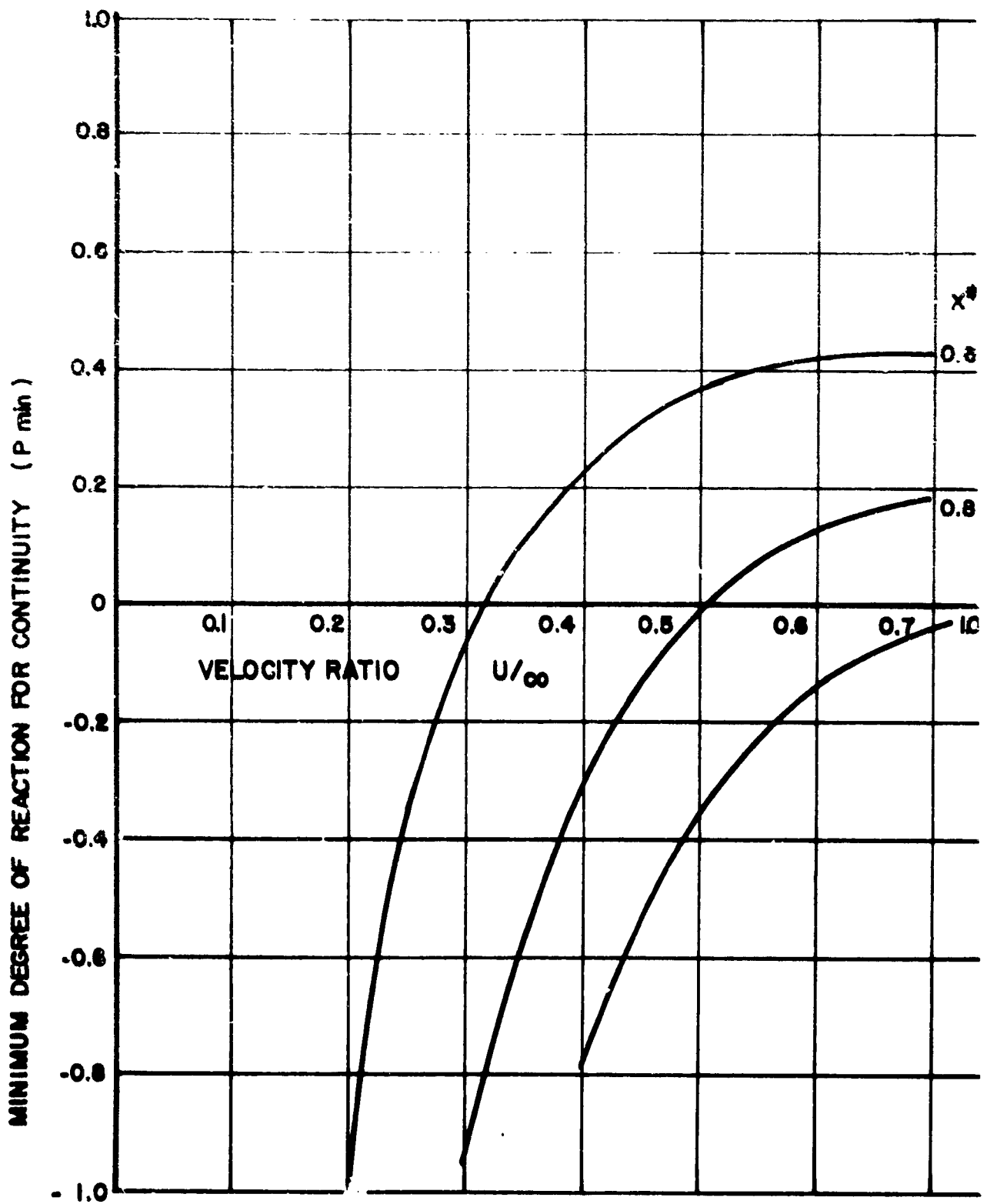
F:       .O. MINIMUM REQUIRED DEGREE OF REACTION FOR FIRST TRANSONIC
        DESIGN
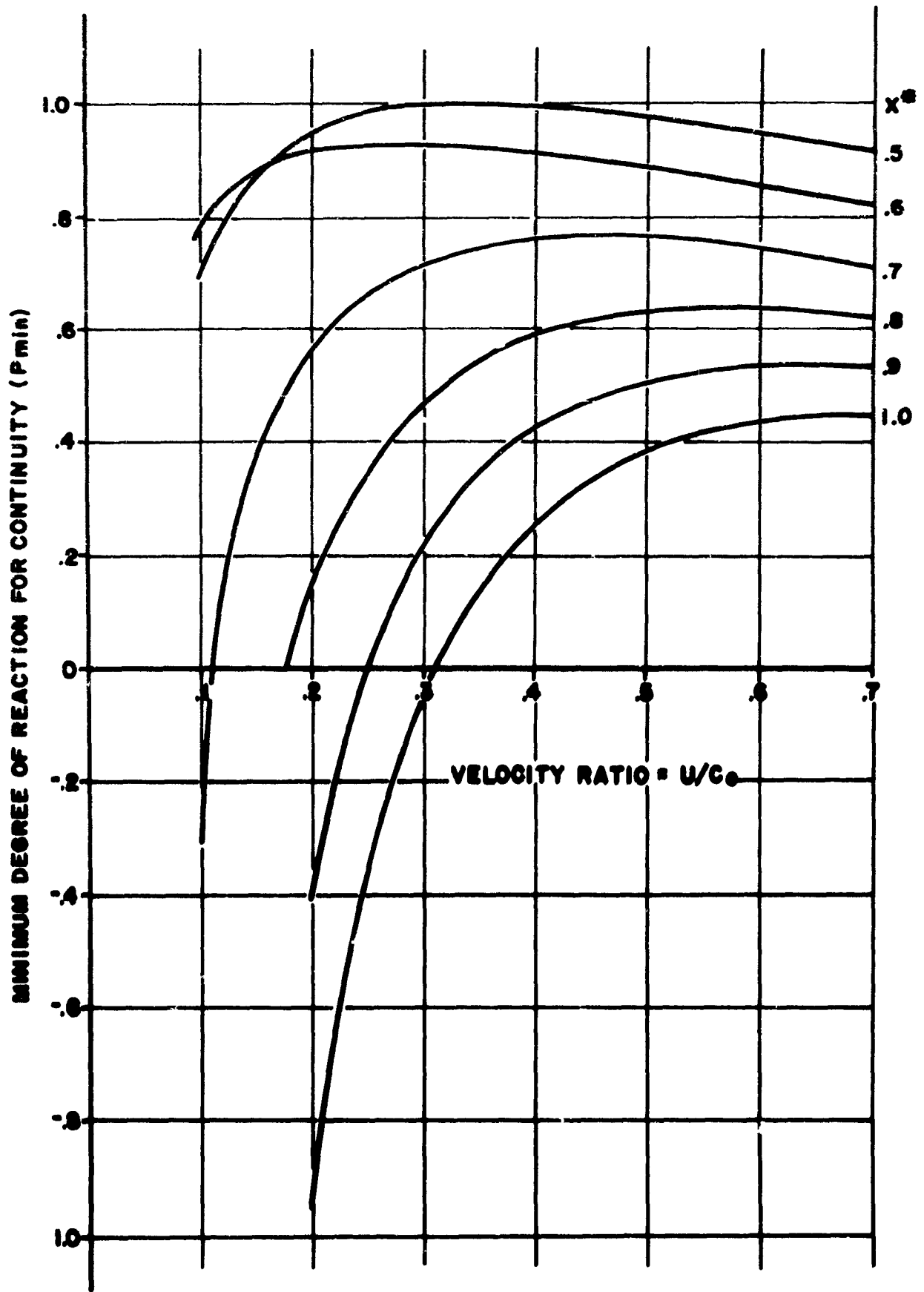
FIGURE 31. MINIMUM REQUIRED DEGREE OF REACTION FOR SECOND TRANSONIC DESIGN
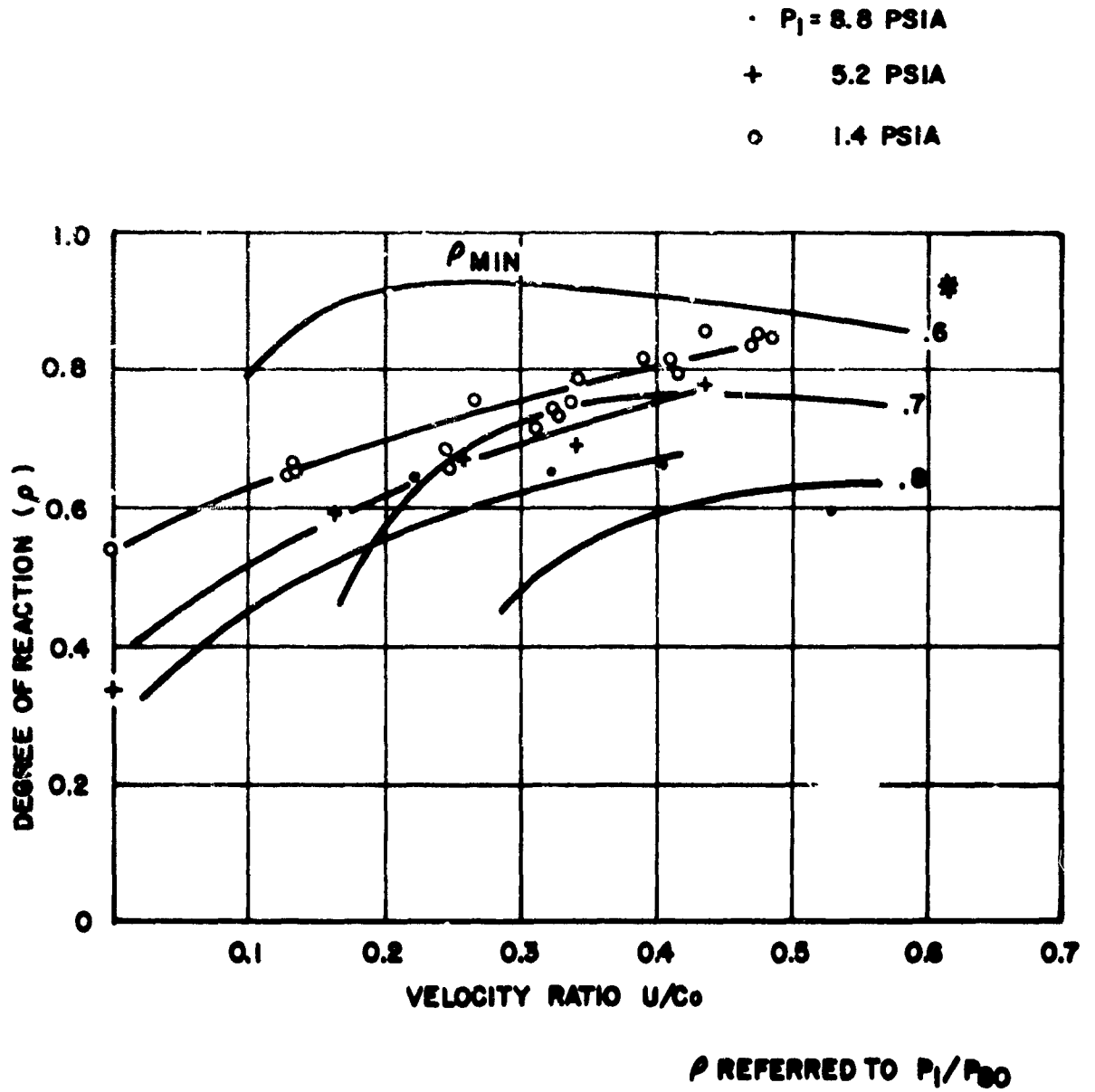
FIGURE 32. COMPARISON OF MEASURED DEGREE OF REACTION WITH ∂ MIN FOR SECO
TRANSONIC DESIGN
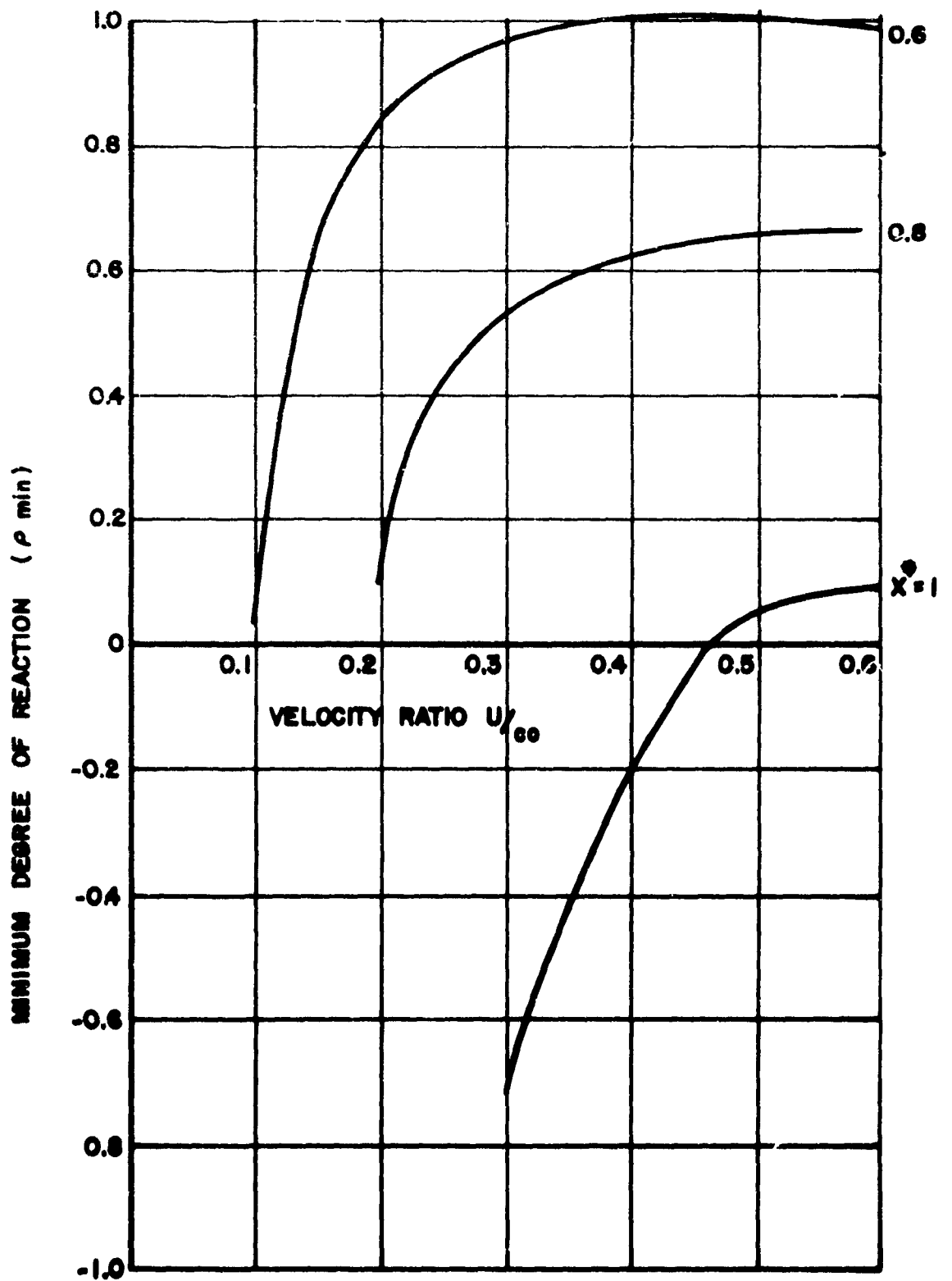
FIGURE 33. MINIMUM DEGREE OF REACTION FOR TURBINE GEOMETRY TESTED IN REF.
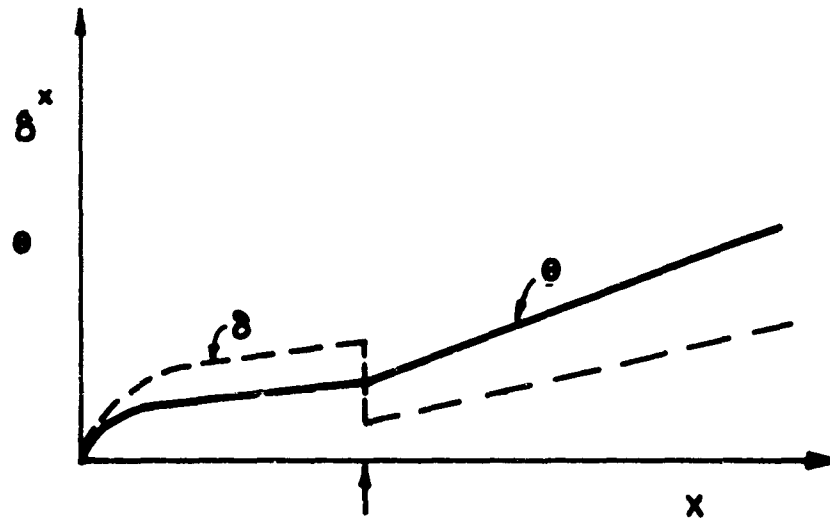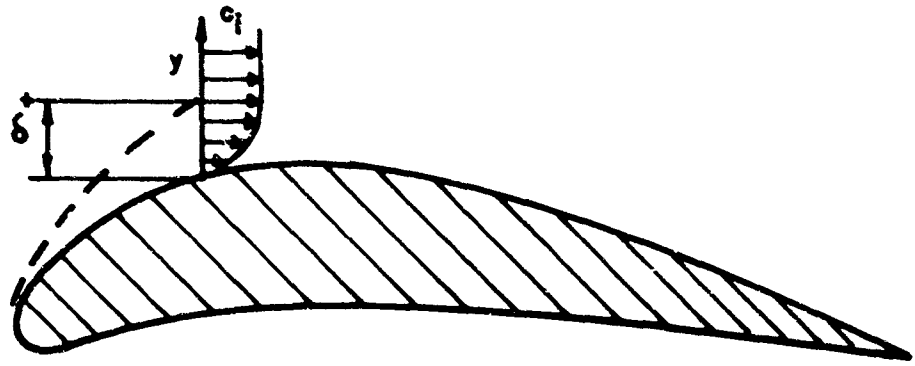
FIGURE 34. BOUNDARY LAYER GROWTH

LOCAL LOSS FACTOR
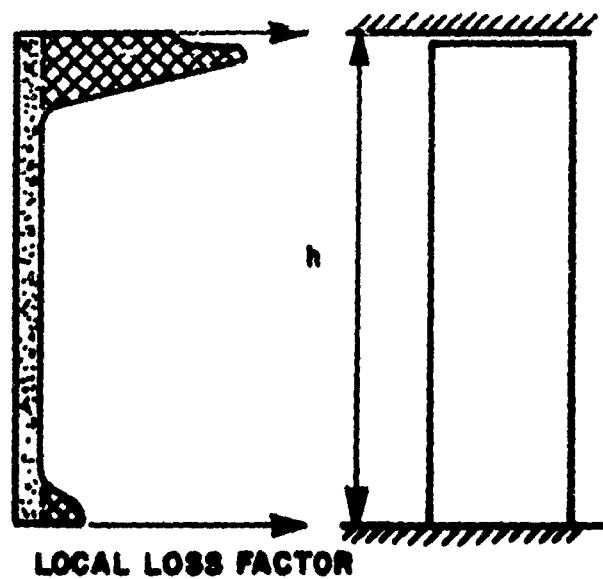
FIGURE 35. TYPICAL LOSS DISTRIBUTION IN AXIAL CASCADES
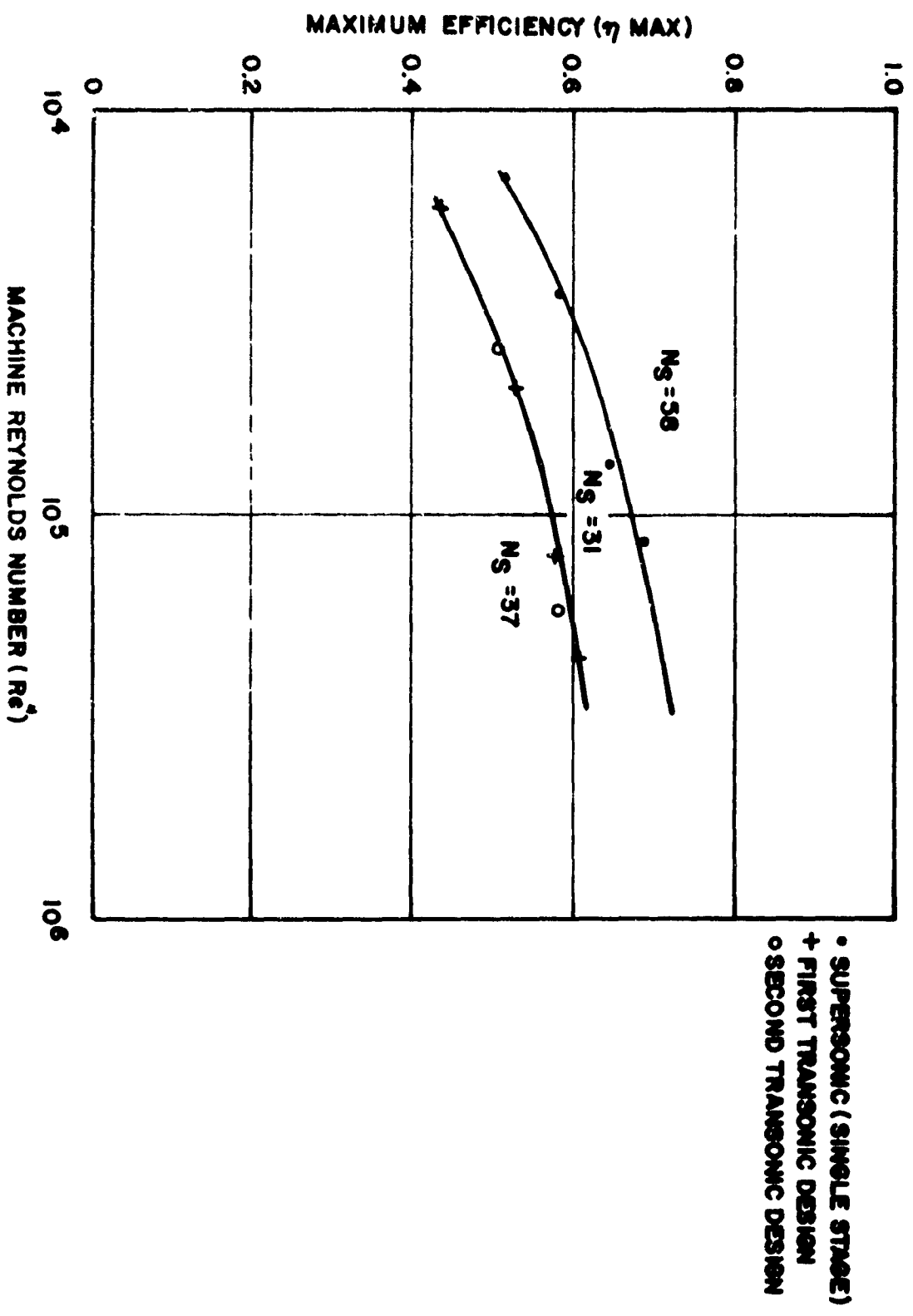
FIGURE 37. PEAK EFFICIENCY OF SINGLE STAGE TESTS AS FUNCTION OF MACHINE REYNOLDS NUMBER
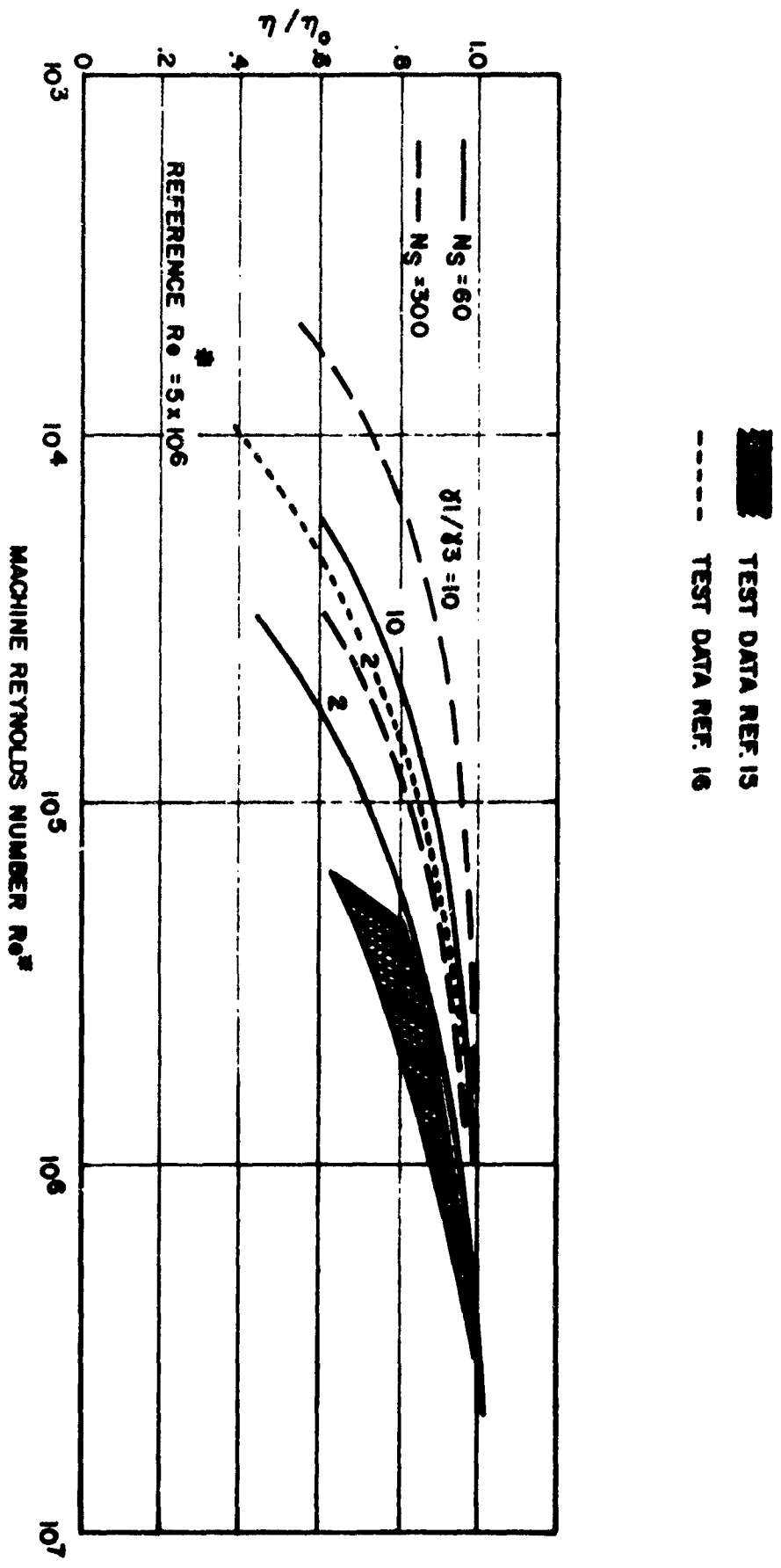
FIGURE 36. CALCULATED REYNOLDS NUMBER INFLUENCE DATA

AG 5676
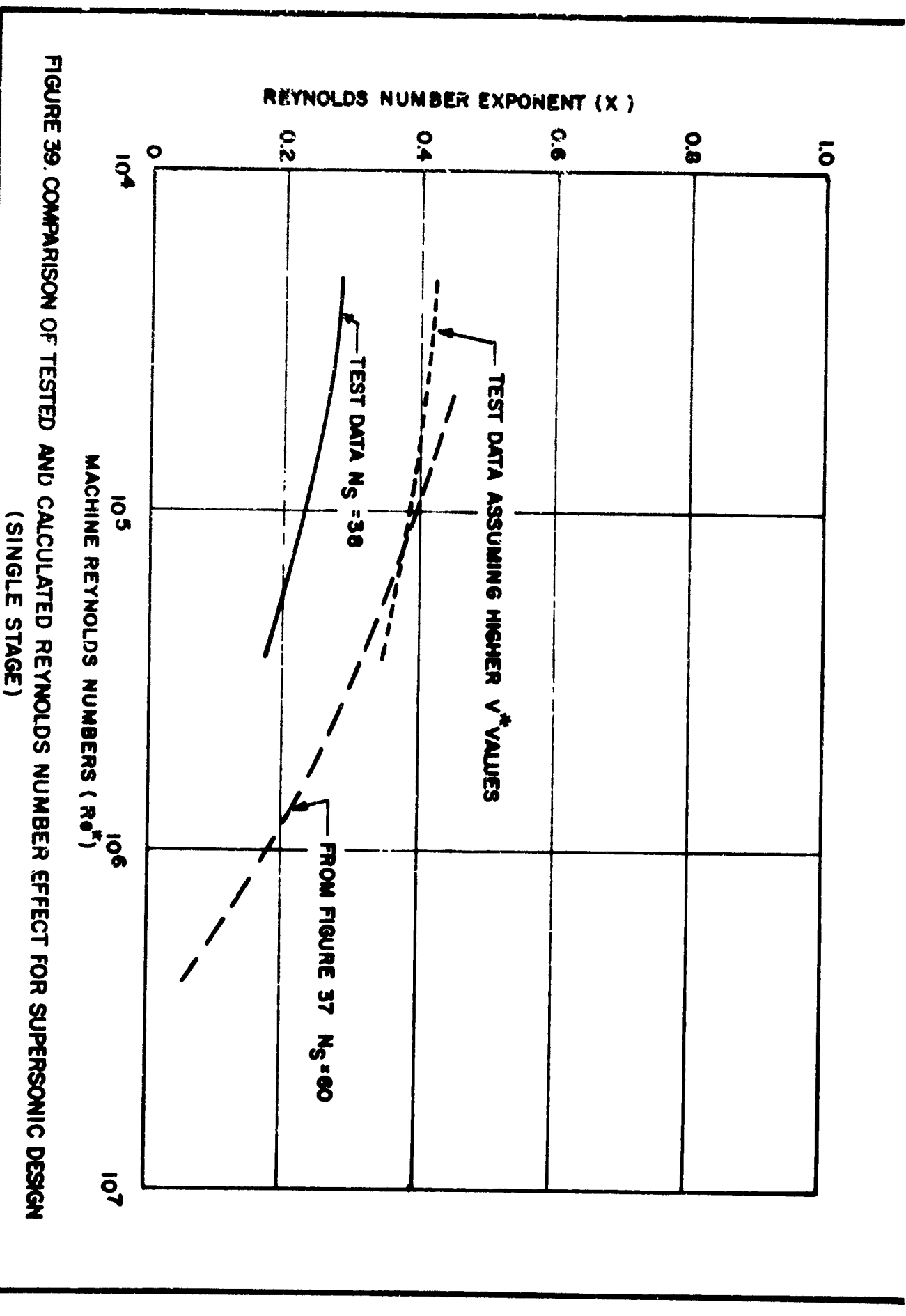
FIGURE 39. COMPARISON OF TESTED AND CALCULATED REYNOLDS NUMBER EFFECT FOR SUPERSONIC DESIGN (SINGLE STAGE)

REYNOLDS NUMBER EXPONENT (X)
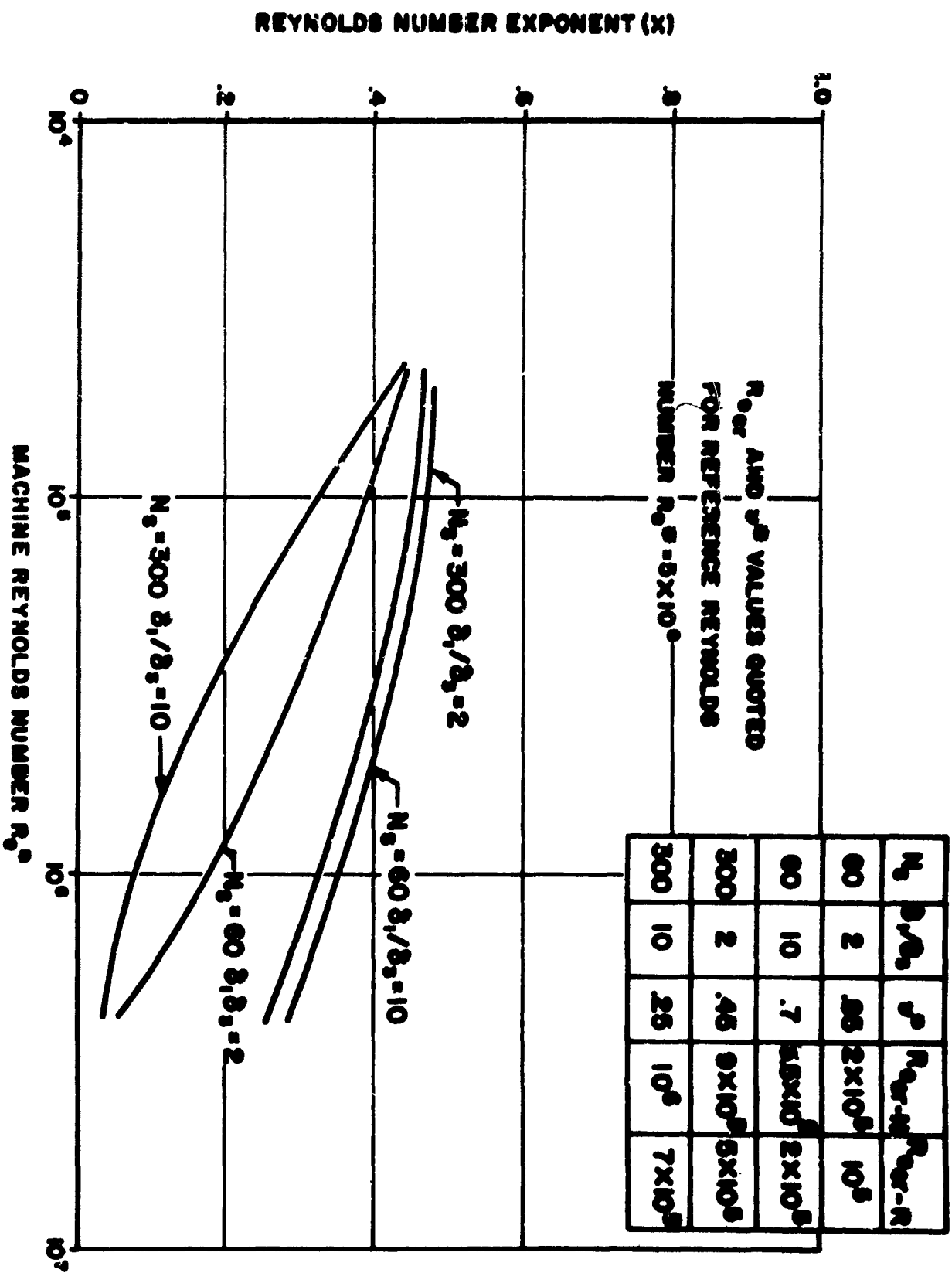
FIGURE 38. REYNOLDS NUMBER EXPONENT (X) ACCORDING TO FIGURE 36
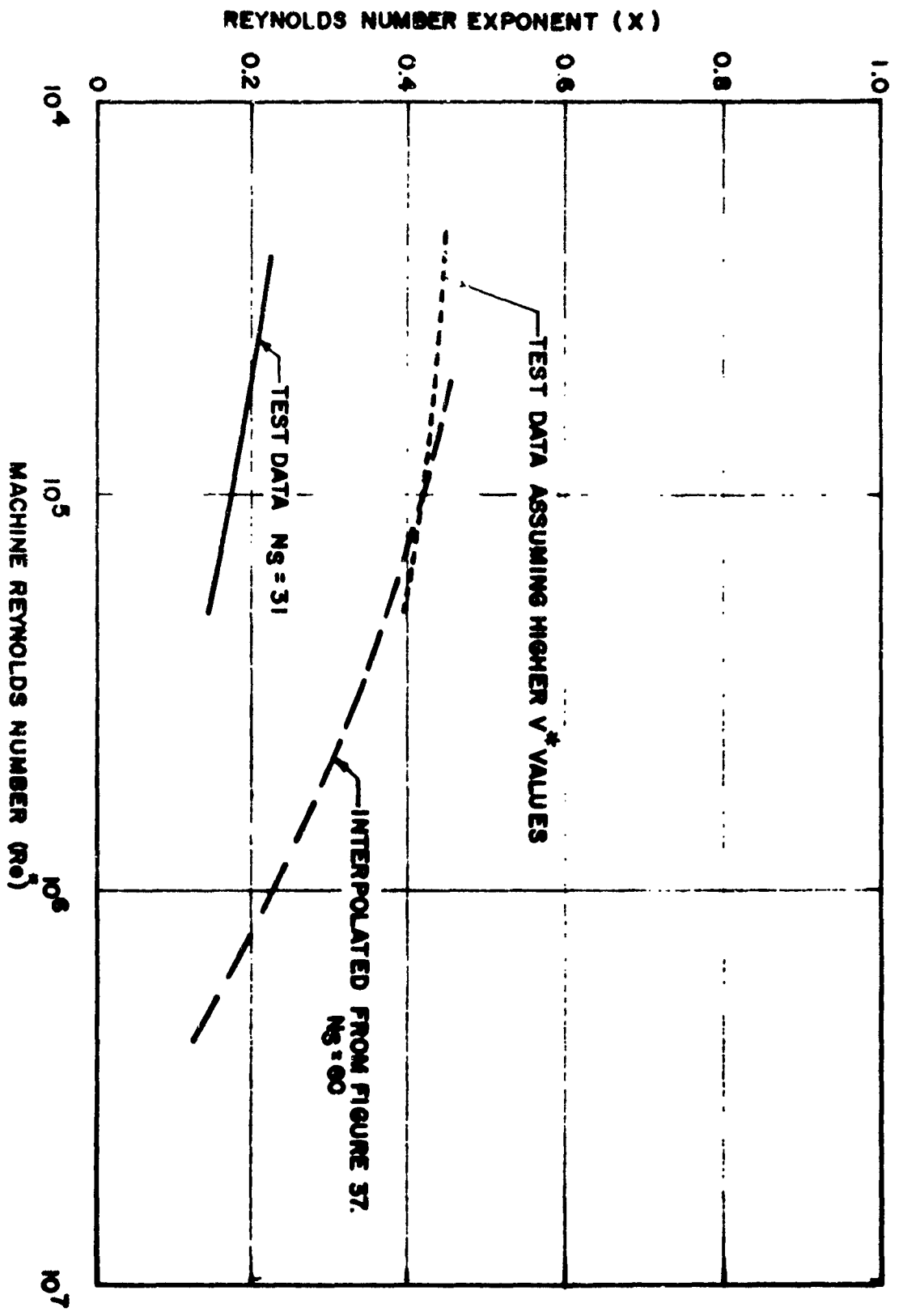
FIGURE 40. COMPARISON OF TESTED & CALCULATED REYNOLDS NUMBER EFFECT FOR FIRST TRANSONIC DESIGN
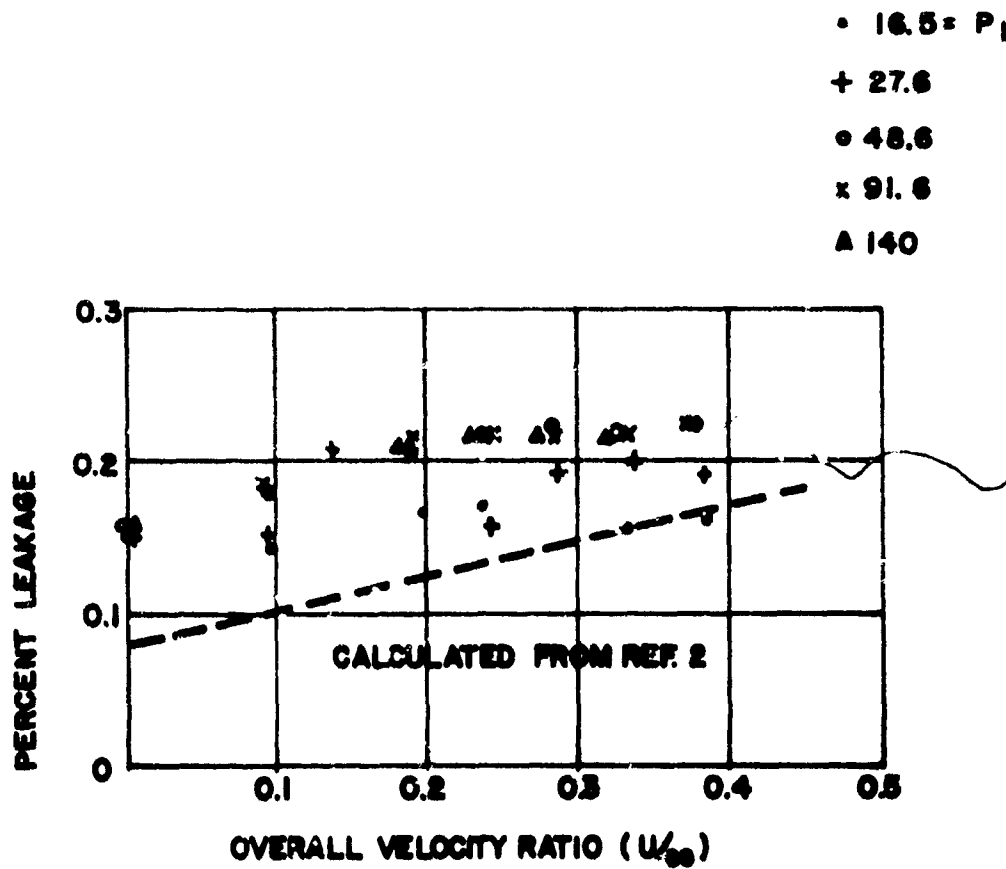
FIGURE 41. LEAKAGE DATA FOR RE-ENTRY TURBINE
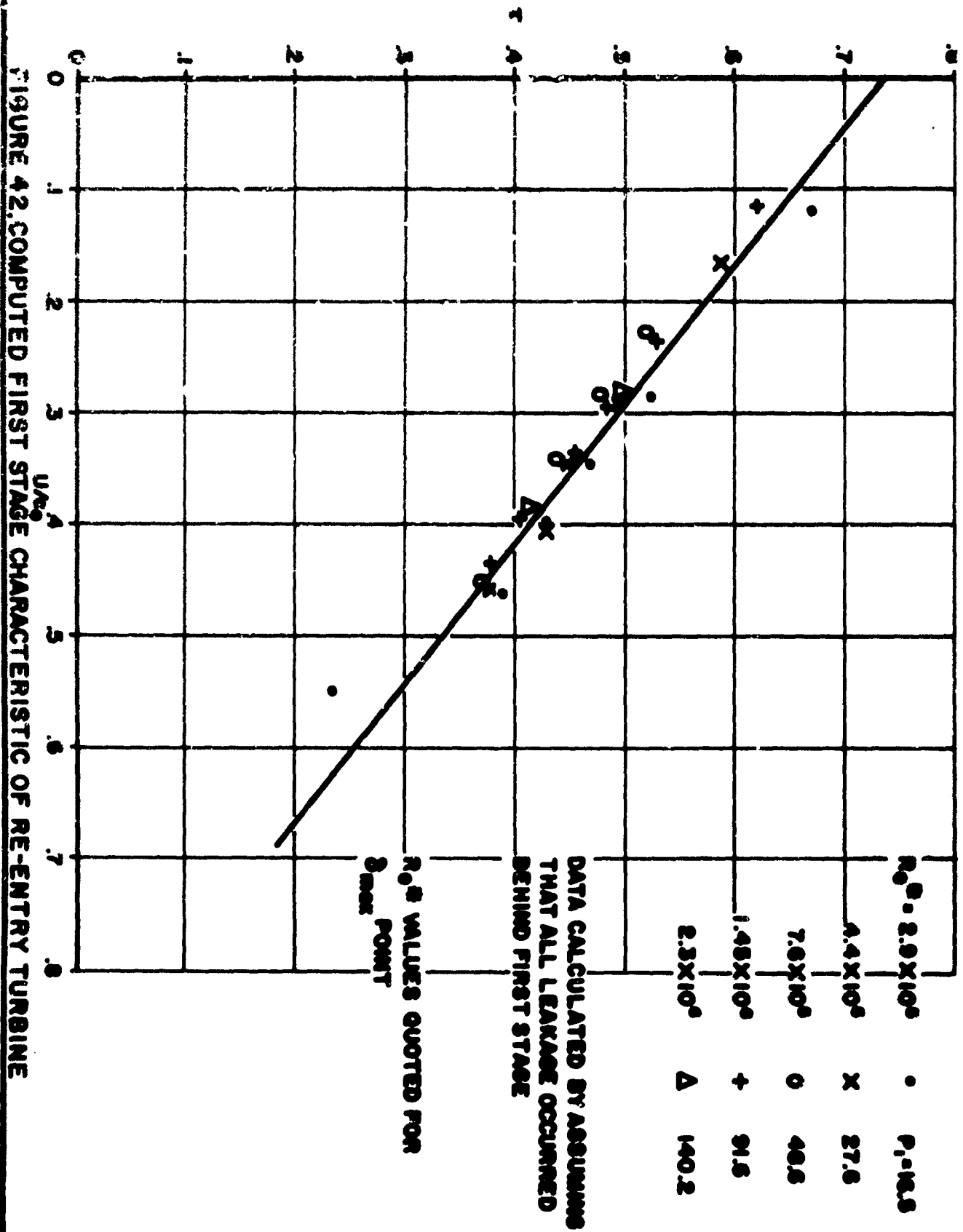
FIGURE 42. COMPUTED FIRST STAGE CHARACTERISTIC OF RE-ENTRY TURBINE
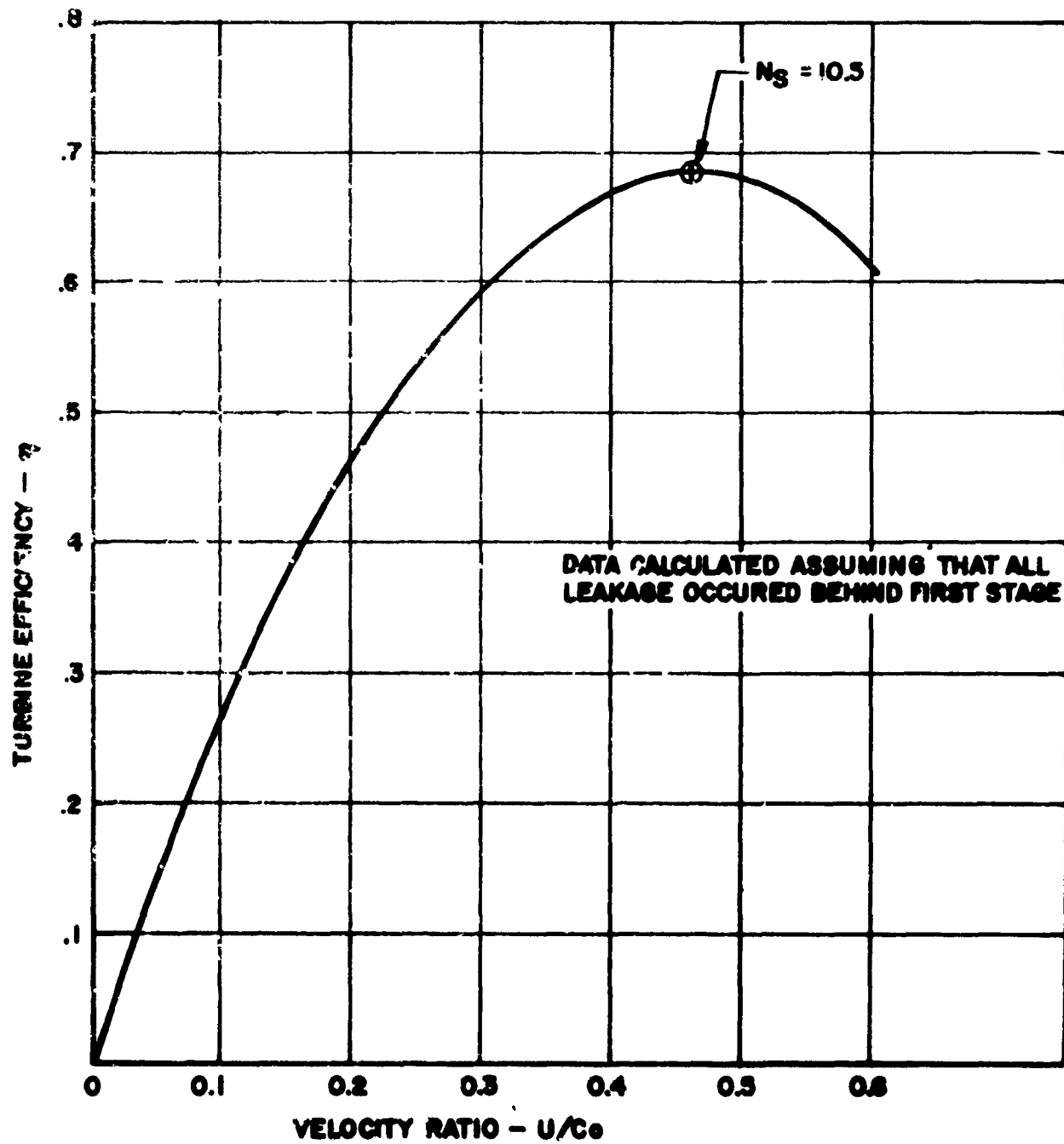
FIGURE 43. COMPUTED FIRST STAGE CHARACTERISTIC OF REENTRY TURBINE
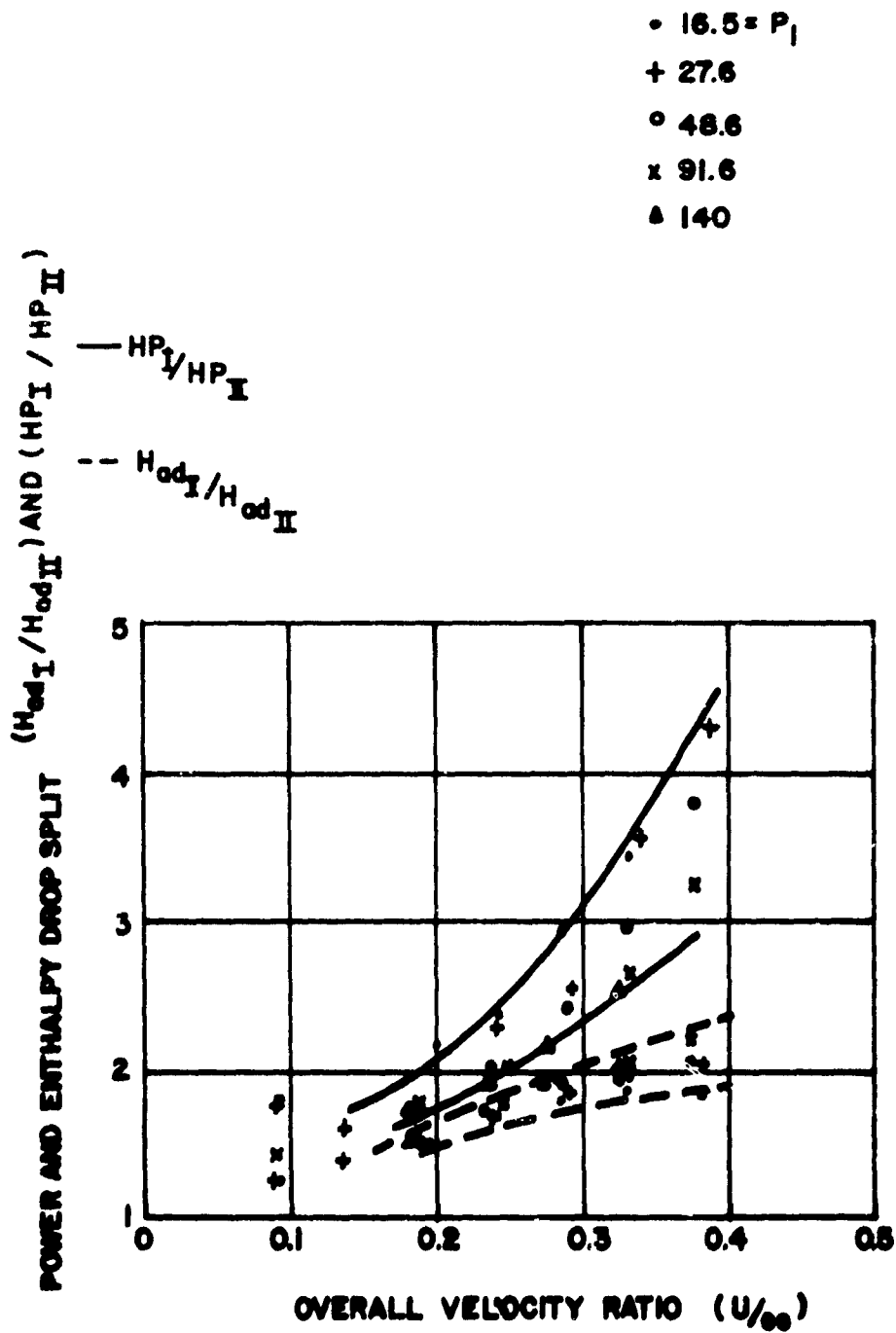
FIGURE 44. LOAD AND HEAT SPLIT IN RE-ENTRY TURBINE

TURBINE MAXIMUM EFFICIENCY ( $\eta$ MAX.)

MACHINE REYNOLDS NUMBER Re*

$N_s = 2.4$
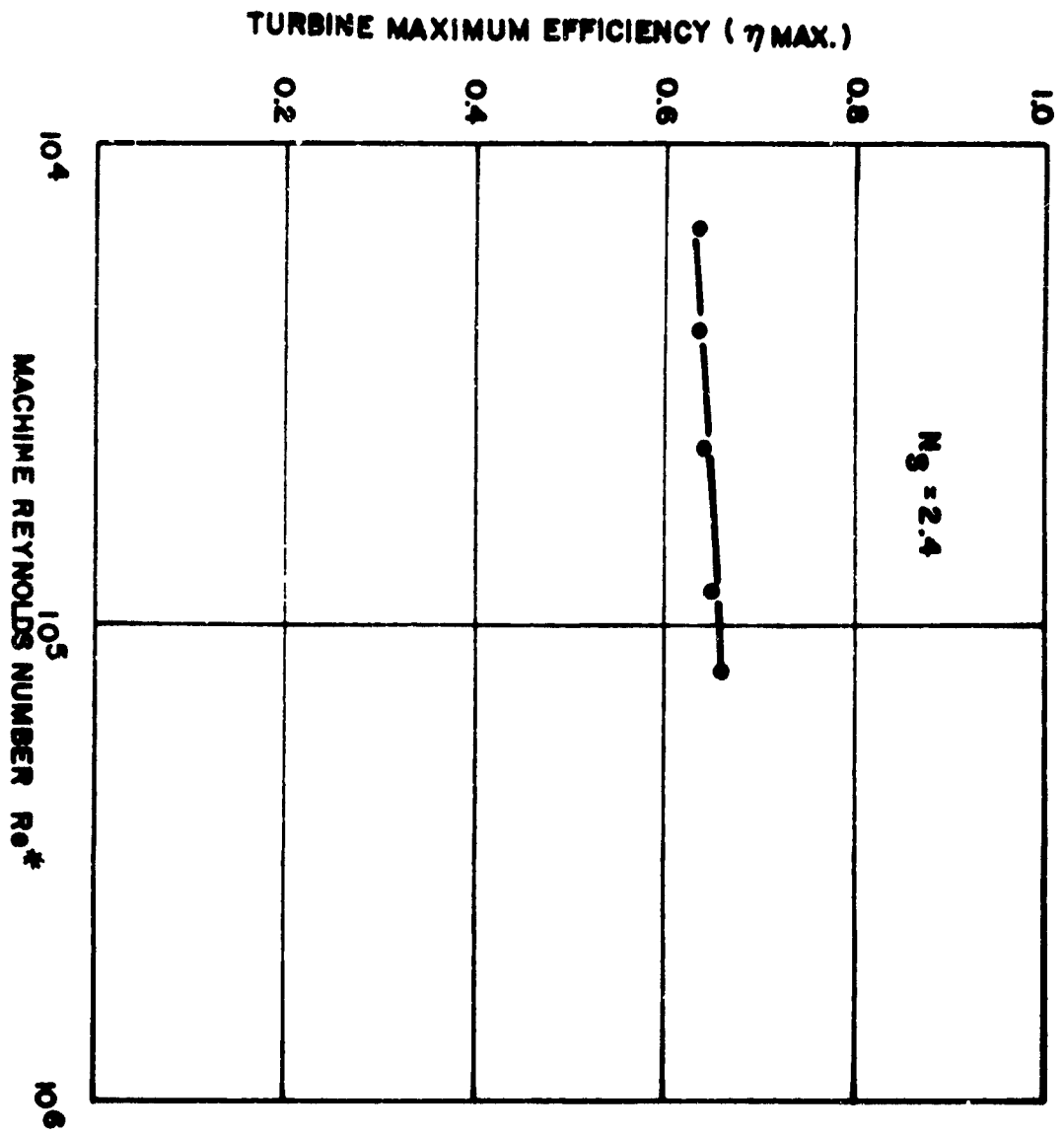
FIGURE 45 REYNOLDS NUMBER DATA FOR RE-ENTRY TURBINE
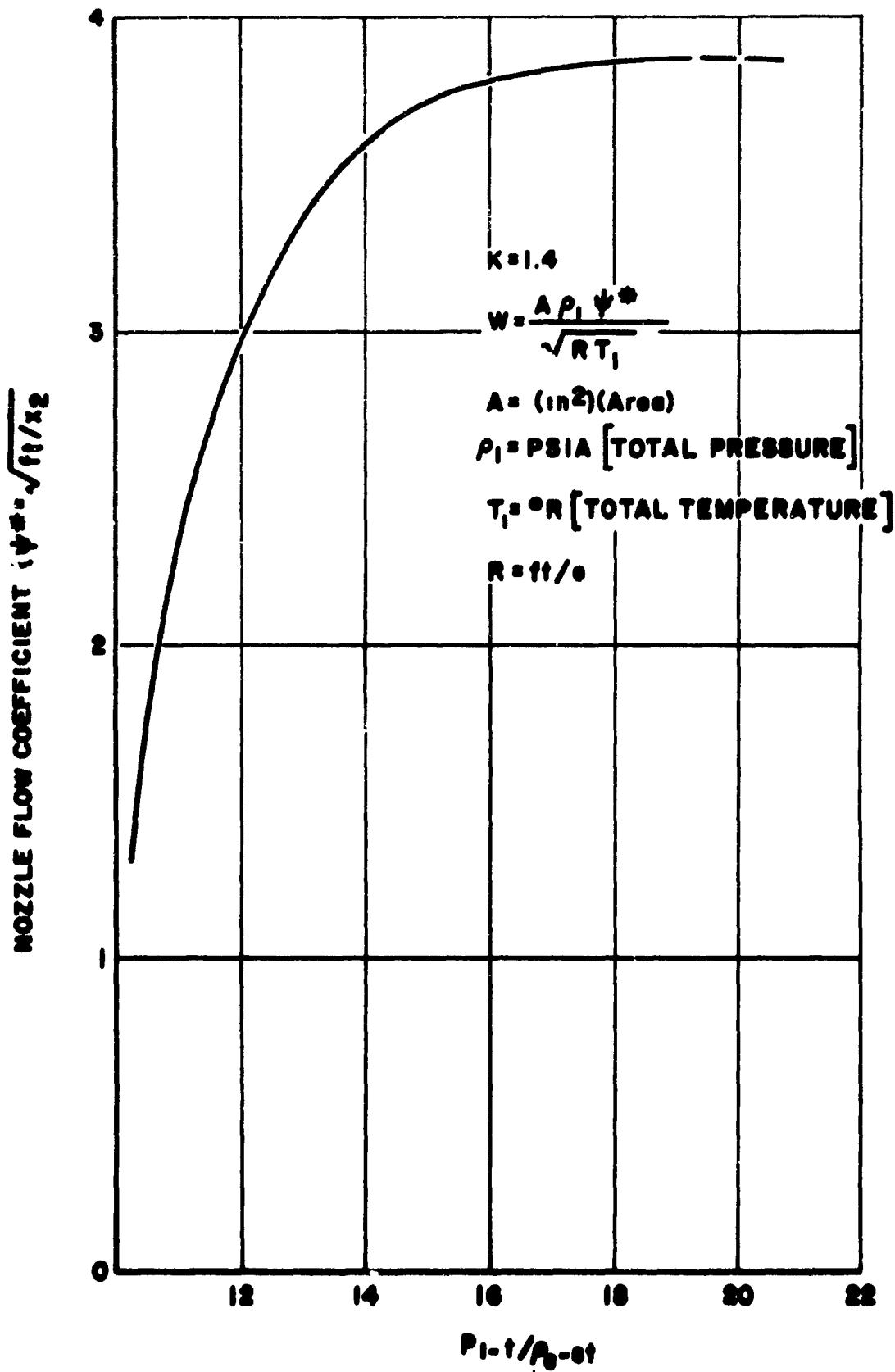
FIGURE 46. NOZZLE COEFFICIENT AS FUNCTION OF NOZZLE PRESSURE RA
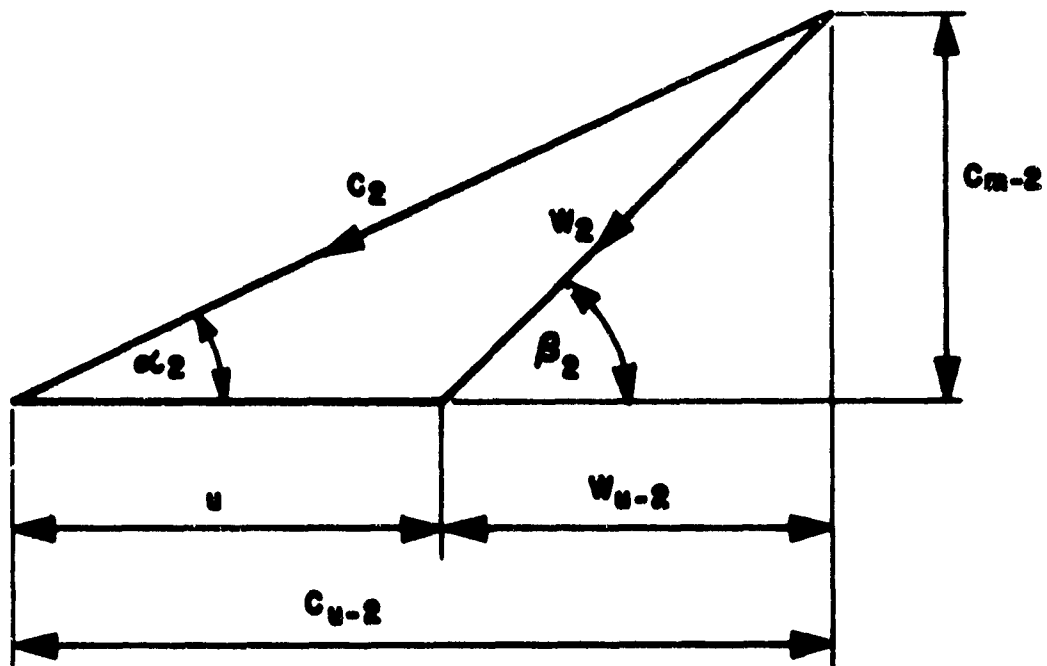
FIGURE 47. INLET VELOCITY TRIANGLE
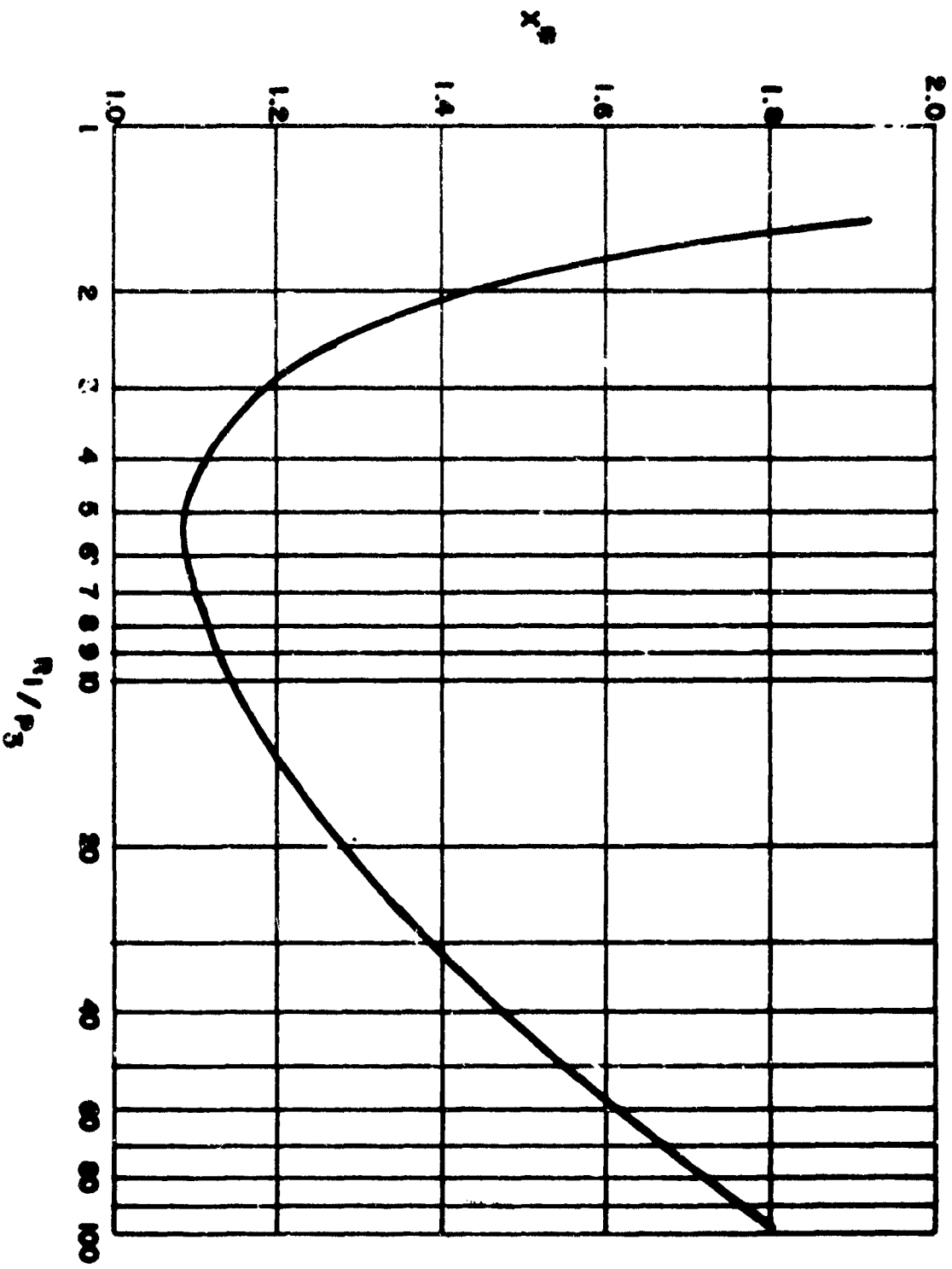
FIGURE 49. TYPICAL $X^*$ VALUE FOR IMPULSE TURBINES

FIGURE 48 NOZZLE AREA RATIO

$A_e/A_{thr}$

PRESSURE RATIO $(P/p_a)$

NOZZLE AREA RATIO $(A_e/A_{throat})$
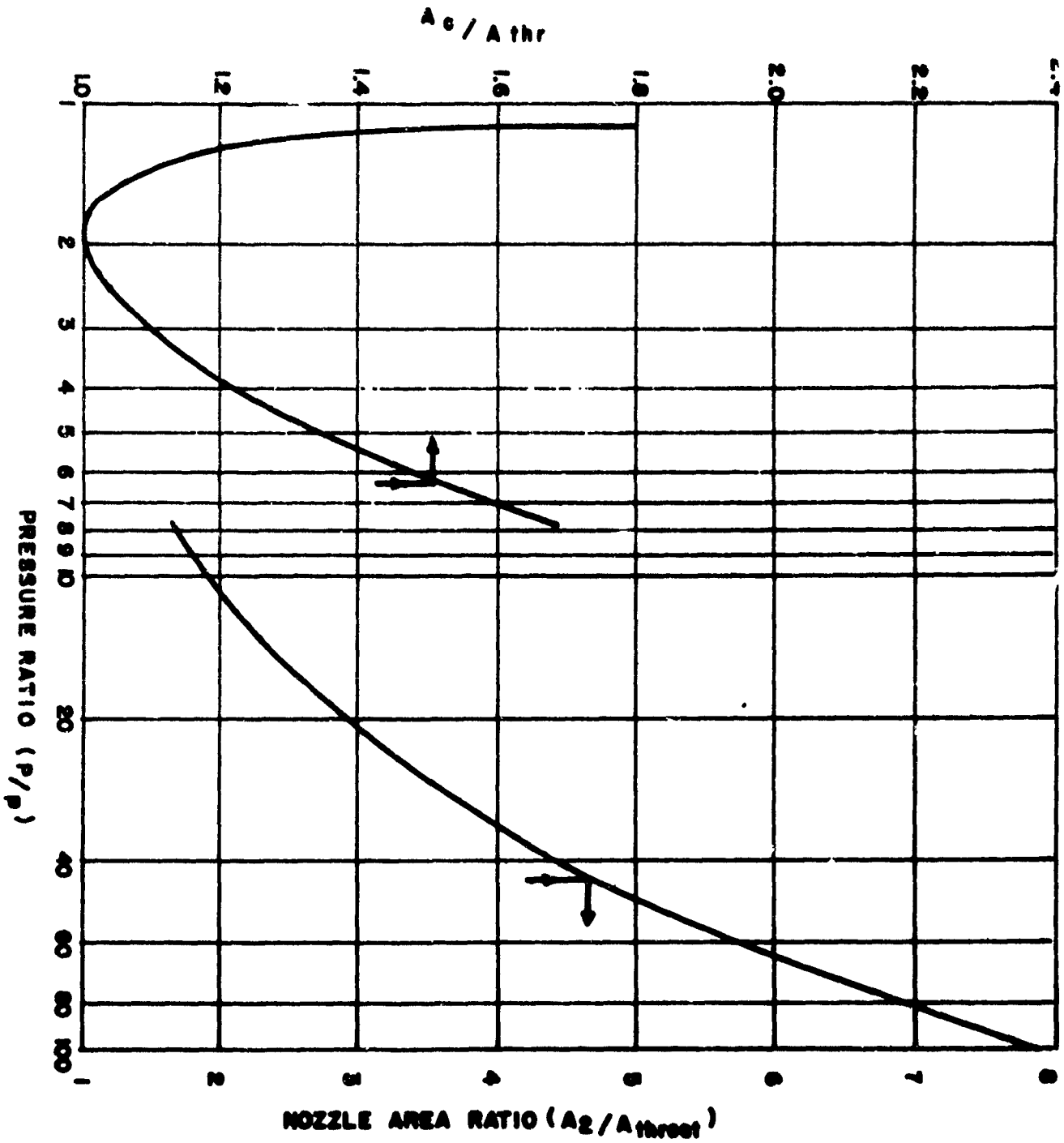
# 9.0 APPENDICES

## 9.1 DERIVATION OF RELATION FOR MINIMUM DEGREE OF REACTION

In order to satisfy the continuity condition for nozzle and rotor the relation

$$\frac{A_N P_N \Psi_N^*}{\sqrt{RT_N}} = \frac{A_R P_R \Psi_R^*}{\sqrt{RT_R}} \tag{18}$$

must be satisfied. In this relation $A_N$ denotes the nozzle throat area, $P_N$ the total pressure in the nozzle throat, $R$ the gas constant, $T_N$ the total temperature in the nozzle throat $A_R$, the throat area of the rotor $P_R$ the total pressure in the rotor throat $T_R$, the total temperature in the rotor throat and $\Psi_N^*$ and $\Psi_R^*$ the flow factors which follow Equation 7. Thus $\Psi^*$ becomes a constant value in cases where the pressure ratio across the orifice is above the critical value(Figure 46). Solving Equation (18) for the ratio of the total pressures at nozzle throat and rotor throats, it results

$$\frac{P_N}{P_R} = \frac{A_R}{A_N} \frac{\Psi_R^*}{\Psi_N^*} \sqrt{\frac{T_N}{T_R}} \tag{19}$$

indicating that this ratio depends only on the area ratio, the flow factor ratio and the temperature ratio. The total temperature at the rotor throat can be written as function of the total temperature in the nozzle throat and the velocity components at nozzle exit and rotor inlet in the form

$$T_R = T_N - \frac{c_2^2}{2Jgc_p} + \frac{W_2^2}{2Jgc_p} = T_N - \frac{c_2^2 - W_2^2}{2Rg \frac{k}{k-1}} \tag{20}$$

when $c_2$ denotes the leaving velocity from the nozzle and $W_2$ the relative approach velocity to the rotor (Figure 47). These velocities can be expressed in terms of the meridional velocity $c_{m-2}$, the rotor speed $u$ and the peripheral component $W_{-2}$ of the relative velocity (see Figure 47) in the form

$$c_2^2 - W_2^2 = c_m^2 + (u + W_{u-2})^2 - W_2^2 = c_m^2 + u^2 + 2uW_{u-2} + W_{u-2}^2 - W_2^2 \tag{21}$$

considering now that

$$c_m^2 + W_{u-2}^2 = W_2^2 \qquad (22)$$

the difference in relative velocity approaching the rotor and nozzle leaving velocity can be quoted in the form

$$c_2^2 - W_2^2 = u^2 + 2u\,W_{u-2} \qquad (23)$$

The peripheral component of the relative approach velocity to the rotor can be quoted in the form (see Figure 47)

$$W_{u-2} = c_2 \cos \alpha_2 - u = c_o \sqrt{1 - \rho}\ \cos \alpha_2 - u \qquad (24)$$

when $\rho$ denotes the degree of reaction, $c_o$ the spouting velocity and $\alpha_2$ the nozzle angle. Introducing Equation (24) into Equation (23) yields the relation

$$c_2^2 - W_2^2 = 2u\,c_o \cos \alpha_2 \sqrt{1 - \rho} - u^2 \qquad (25)$$

Introducing now Equation (23) into Equation (17) the relation

$$\frac{P_R}{P_N} = \frac{A_N\,Y_N^{*}}{A_R\,Y_R^{*}}\ \sqrt{1 - Y_o \left[2 \cos \alpha_2 \sqrt{1 - \rho}\ \frac{u}{c_o} - \left(\frac{u}{c_o}\right)^2\right]} \qquad (26)$$

results when $Y_o$ refers to the overall pressure ratio $P_1/P_3$ of the turbine and is defined by

$$Y_o = 1 - \left(\frac{P_3}{P_1}\right)^{\frac{k-1}{k}} \qquad (27)$$

Equation 26 indicates the ratio of the total pressure at the rotor throat to the total pressure at the nozzle throat as function of the area ratio, the overall pressure ratio, the degree of reaction, the nozzle angle and the turbine velocity ratio $u/c_o$. It indicates that this ratio decreases with increasing overall pressure ratios and decreasing degree of reaction.

Actually the pressure ratio $P_R/P_N$ in Equation (26) is not an independent parameter but depends also on the ratio of the nozzle velocity to relative rotor approach velocity since

$$\left[ 1 - \left( \frac{P_R}{P_N} \right)^{\frac{k-1}{k}} \right] \frac{k}{k-1} R T_N = \frac{c_2^2 - w_2^2}{2g} \tag{28}$$

Introduci.... w Equation (25) into Equation (28) yields

$$\frac{P_R}{P_N} = \left\{ 1 - Y_o \left[ 2 \cos \alpha_2 \frac{u}{c_o} \sqrt{1-\rho} - \left( \frac{u}{c_o} \right)^2 \right] \right\}^{\frac{k}{k-1}} \tag{29}$$

which ⁚ ·· as that the available pressure ratio betweer total pressure at the roto. ...roat and total pressure at the nozzle throat is determined by the overall turbine pressure ratio, the nozzle angle, the degree of reaction and the turbine velocity ratio. Equating now Equation (26) with Equation (29) a relation of the form

$$\frac{A_N \Psi_N^*}{A_R \Psi_R^*} = \left\{ 1 - Y_o \left[ 2 \cos \alpha_2 \frac{u}{c_o} \sqrt{1-\rho} - \left( \frac{u}{c_o} \right)^2 \right] \right\}^{\frac{1+k}{2(k-1)}} \tag{30}$$

results which indicates that a certain ratio of nozzle throat area to rotor throat area is required and that this ratio is a function of overall pressure ratio degree of reaction, turbine velocity ratio and nozzle angle. It is also evident that a certain minimum degree of reaction for given turbine velocity ratios, area ratios and nozzle angles are required in order to satisfy the continuity relation. This can be expressed by solving Equation (30) for the degree of reaction yielding a relation of the form

$$\sqrt{1-\rho} = \frac{B + \left( \frac{u}{c_o} \right)^2}{2 \cos \alpha_2 \left( \frac{u}{c_o} \right)} \tag{31}$$

with

$$B = \frac{1 - \left( \frac{A_N \Psi_N^*}{A_R \Psi_R^*} \right)^{\frac{2(k-1)}{1+k}}}{Y_o} \tag{32}$$

It is now of interest to generalize the information presented in Equation (31) and (32) by expressing the nozzle throat area and rotor throat area in terms of the turbine geometry. Assuming typical design features, the area ratio can be expressed by the relation

$$\frac{A_N}{A_R} = \frac{h_N \, \sin \alpha_2 \, \left(\frac{t - t_e}{t}\right)_N \, \frac{A_{throat}}{A_2}}{h_R \, \sin \beta_3 \, \left(\frac{t - t_e}{t}\right)_R} \tag{33}$$

when $h_n$ denotes the nozzle heights $h_r$ the rotor blade heights, $\alpha_2$ the nozzle angle, $\beta_3$ the rotor exit angle, t the blade spacing, $t_e$ the trailing edge thickness and when the ratio

$$\frac{A_2}{A_{throat}} = \frac{1}{M}\left[\frac{2}{k+1} \left(1 + \frac{k-1}{2} M^2\right)\right]^{\frac{k+1}{2(k-1)}} \tag{34}$$

denotes the ratio of the throat area to the downstream area with M denoting the Mach number. This ratio is a function of the nozzle pressure ratio as indicated in Figure 48. Introducing Equation (33) into Equation (30) the desired ratio of nozzle heights to blade heights can be found as function of turbine pressure ratio, turbine velocity ratio, degree of reaction and turbine geometry. This then is the minimum required heights ratio in order to satisfy the continuity conditions.

$$x^* = \frac{h_N}{h_R} = \frac{(1 - Y_o B)^{\frac{1+k}{2(k-1)}}}{\sin \alpha_2 / \sin \beta_3} \quad \frac{A_2}{A_{throat}} \quad \frac{\left(\frac{t - t_e}{t}\right)_R}{\left(\frac{t - t_e}{t}\right)_N} \tag{35}$$

Introducing now typical geometry values for impulse turbines into Equation 25, $x^*$ values as indicated in Figure 49 result indicating that $x^*$ becomes a minimum at turbine pressure ratios of 5:1. The fact that $x^* > 1$ indicates that the rotor heights may be made smaller than the nozzle heights without incurring rotor choking in the ideal case, i. e. , when no flow losses have to be considered.

Actually it is customary to make the nozzle heights and blade heights equal in impulse turbines. In this case the ratio $x^*$ can be interpreted as the allowable acceleration of the meridional component through the rotor or as the ratio of effective flow area (geometrical flow area minus boundary layer displacement thickness) to geometrical through flow area. With this interpretation the significance of this ratio is that comparatively large boundary layer displacement thickness can be tolerated for low pressure ratio impulse turbines and high pressure ratio impulse turbines that only a comparatively small boundary layer displacement thickness can be tolerated at pressure ratios of about 5. More specifically it means that for conventional geometries, i. e. nozzle blade heights equal to rotor blade heights, only a displacement thickness of 7. 5% can be tolerated at pressure ratios of 5 and still retain impulse action. If this ratio is exceeded the turbine cannot operate as impulse turbines but has to operate at a higher degree of reaction in order to satisfy the continuity condition. This then means that impulse turbines designed for pressure ratios of 5 are particularly sensitive to rotor choking.